

Nonlinear, Adaptive and Fault-tolerant Control for Electro-hydraulic Servo Systems

Choux, Martin; Blanke, Mogens; Hovland, Geir

Publication date:
2011

Document Version
Publisher's PDF, also known as Version of record

[Link back to DTU Orbit](#)

Citation (APA):
Choux, M., Blanke, M., & Hovland, G. (2011). Nonlinear, Adaptive and Fault-tolerant Control for Electro-hydraulic Servo Systems. Technical University of Denmark (DTU).

DTU Library

Technical Information Center of Denmark

General rights

Copyright and moral rights for the publications made accessible in the public portal are retained by the authors and/or other copyright owners and it is a condition of accessing publications that users recognise and abide by the legal requirements associated with these rights.

- Users may download and print one copy of any publication from the public portal for the purpose of private study or research.
- You may not further distribute the material or use it for any profit-making activity or commercial gain
- You may freely distribute the URL identifying the publication in the public portal

If you believe that this document breaches copyright please contact us providing details, and we will remove access to the work immediately and investigate your claim.

Martin Choux

Nonlinear, Adaptive and Fault-Tolerant Control for Electro Hydraulic Servo Systems

PhD thesis, December 2011

Nonlinear, Adaptive and Fault-Tolerant Control for Electro Hydraulic Servo Systems

Martin Choux

Kongens Lyngby 2011
DTU Elektro - PHD-2011

Technical University of Denmark
Department of Electrical Engineering
Building 348, DK-2800 Kongens Lyngby, Denmark
Phone +45 45253800, Fax +45 45931634
info@elektro.dtu.dk
www.elektro.dtu.dk

DTU Elektro-PHD: ISBN 978-87-92465-92-4

Summary

Fluid power systems have been in use since 1795 with the first hydraulic press patented by Joseph Bramah and today form the basis of many industries. Electro hydraulic servo systems are fluid power systems controlled in closed-loop. They transform reference input signals into a set of movements in hydraulic actuators (cylinders or motors) by the means of hydraulic fluid under pressure. With the development of computing power and control techniques during the last few decades, they are used increasingly in many industrial fields which require high actuation forces within limited space.

However, despite numerous attractive properties, hydraulic systems are always subject to potential leakages in their components, friction variation in their hydraulic actuators and deficiency in their sensors. These violations of normal behaviour reduce the system performances and can lead to system failure if they are not detected early and handled. Moreover, the task of controlling electro hydraulic systems for high performance operations is challenging due to the highly nonlinear behaviour of such systems and the large amount of uncertainties present in their models.

This thesis focuses on nonlinear adaptive fault-tolerant control for a representative electro hydraulic servo controlled motion system. The thesis extends existing models of hydraulic systems by considering more detailed dynamics in the servo valve and in the friction inside the hydraulic cylinder. It identifies the model parameters using experimental data from a test bed by analysing both the time response to standard input signals and the variation of the outputs with different excitation frequencies. The thesis also presents a model that accurately describes the static and dynamic normal behaviour of the system. Further, in

this thesis, a fault detector is designed and implemented on the test bed that successfully diagnoses internal or external leakages, friction variations in the actuator or fault related to pressure sensors. The presented algorithm uses the position and pressure measurements to detect and isolate faults, avoiding missed detection and false alarm.

The thesis also develops a high performance adaptive nonlinear controller for the hydraulic system which outperforms comparable linear controllers widely used in the industry. Because of the controller adaptivity, uncertainties in the model parameters can be handled. Moreover, a special attention is given to reduce the complexity of the controller in order to demonstrate its real-time implementation. Finally the thesis combines the techniques developed in fault detection and nonlinear control in order to develop an active fault-tolerant controller for electro hydraulic servo systems. In order to maintain overall service and performances as high as possible when a potential fault occurs, the fault-tolerant controlled system prognoses the fault and changes its controller parameters or structure. The consequences of an unexpected fault are avoided, high availability is ensured and the overall safety in electro hydraulic servo systems is increased.

Resumé

Hydraulisk kraftoverførsel udgør fundamentet i mange industrielle processer til håndtering og bearbejdning og har været anvendt siden Joseph Bramah patenterede en hydraulisk presse. I et elektro-hydrauliske servosystem omsættes referencesignaler til bevægelse ved hjælp af lukket sløjfe styring, for eksempel i form af en computer som sender signaler til en magnetventil som regulerer tilstrømningen af olie til en hydraulisk cylinder. Den hydrauliske cylinders position og andre målesignalet føres tilbage til computeren. Hydrauliske aktuatorer udmærker sig ved at kunne yde meget store kræfter og momenter.

De store kræfter dannes af olie eller vand under højt tryk og hydrauliske komponenter udsættes let for lækage. Friktion og andre defekter kan udvikle sig og sådanne afvigelser fra normal opførsel skal detekteres for at sikre fuld funktionalitet af det maskineri, som hydraulikken er en del af. Hvis fejl ikke detekteres og håndteres i tide, fører de let til funktionssvigt eller nedbrud. Selve styringen af hydrauliske aktuatorer er også vigtig, og udfordringer i forbindelse med lukket-sløjfe styring udgøres af ikke-lineære fænomener og usikkerhed omkring parametre i dynamiske modeller for de hydrauliske enheder.

Afhandlingen fokuserer på ikke-lineær, adaptiv og fejltolerant styring af en hydraulisk servostyring. Afhandlingen udvider eksisterende modeller af hydrauliske servosystemer ved at inkludere detaljeret modellering af servoventil og af hydraulisk cylinder friktion. En laboratorieopstilling benyttes til at identificere parametre i en dynamisk model og give en nøjagtig karakterisering af statisk og dynamisk opførsel. Afhandlingen bidrager med at designe og validere algoritmer til at detektere interne og eksterne lækager, variation i friktion i en hydraulisk cylinder og fejl i tryksensorer. Algoritmen benytter målinger af stempel vandring og olie tryk til at isolere de nævnte fejl og statistiske metoder benyttes til

at undgå falske alarmer samtidigt med at pålidelig detektion opnås.

I afhandlingen udvikles der også en adaptiv ikke-lineær regulator for at opnå en kombination af meget høj nøjagtighed og hurtig respons. Det vises at den nye regulator er klart bedre end konventionelle styringer, som anvendes i industrien. Regulatorens adaptive egenskab gør at den effektivt kan håndtere model usikkerheder. Der er desuden arbejdet med at reducere kompleksiteten af regulatoren for at muliggøre en implementering i real tid. Endeligt kombineres fejldetektion og ikke-lineær regulering til en fejltolerant styring for elektro-hydrauliske servosystemer. Den fejltolerante regulator prognosticerer forekomsten af fejl og skifter regulatorparametre eller tilpasser topologi af signalveje for at kunne vedblive at fungere på trods af fejl. Hvad der ellers ville være konsekvenser af uventede fejl, ikke planlagte nedlukning eller pludselig driftsstop, kan undgås og dermed øges pålideligheden for de elektro-hydrauliske system og for den proces, det er en del af.

Preface

This thesis was prepared in collaboration with the Department of Electrical Engineering, the Technical University of Denmark and the Faculty of Engineering and Science, University of Agder, in partial fulfillment of the requirements for acquiring the Ph.D. degree in engineering.

The thesis deals with different aspects of modeling and control of electro hydraulic servo systems using simulation and experimental data. The main focus is on extensions of fault diagnosis and nonlinear control methods, but also real-time implementation of a fault-tolerant controller for a representative electro hydraulic servo system is considered.

The work contained in this thesis, unless explicitly stated, is original research whose major portion was done by the author. The work has not been submitted for a degree at any other university or institution. The research has been carried out in collaboration with Prof. Mogens Blanke and Prof. Geir Hovland during the period 2007-2011.

Grimstad, December 2011

A handwritten signature in black ink, appearing to read 'Martin Choux', with a long horizontal stroke extending to the right.

Martin Choux

Publications based on the thesis work

1. Choux, M., Karimi, H. R., Hovland, G., Hansen, M. R., Ottestad, M., & Blanke, M. (2009). Robust adaptive backstepping control design for a Nonlinear Hydraulic-Mechanical System. Proceedings of the 48h IEEE Conference on Decision and Control (CDC) held jointly with 2009 28th Chinese Control Conference, 2460-2467. IEEE. doi: 10.1109/CDC.2009.5400438.
2. Choux, M., & Hovland, G. (2010). Adaptive Backstepping Control of Non-linear Hydraulic-Mechanical System Including Valve Dynamics. Modeling, Identification and Control: 31(1), 35-44. doi: 10.4173/mic.2010.1.3.
3. M. Choux and G. Hovland (2008), "Design of A Hydraulic Servo System for Robotic Manipulation", Proc. of the 5th FPNI Ph.D Symposium, Krakow 2008, 1-5 July.
4. Choux, M., Hovland, G., & Blanke, M. (2011,submitted). Cascade Controller Including Backstepping for Hydraulic-Mechanical Systems. IFAC Workshop on Automatic Control in Offshore Oil and Gas Production. Trondheim, Norway. May 2012.
5. Choux, M., & Blanke, M. Fault Diagnosis for Nonlinear Hydraulic-Mechanical Drilling Pipe Handling System. IEEE CDC-ECC 2011 Orlando December 12th - 15th.
6. Choux, M., Tyapin, I., & Hovland, G. Extended Friction Model of a Hydraulic Actuated System. To be published in proceedings of Annual Reliability and Maintainability Symposium (RAMS2012) Reno, January 23th - 26th 2012.

7. Choux, M., Tyapin, I., & Hovland, G. Leakage-Detection in Blade Pitch Control Systems for Wind Turbines. To be published in proceedings of Annual Reliability and Maintainability Symposium (RAMS2012) Reno, January 23th - 26th 2012, .

Acknowledgements

It started with a spark, at the end of my master studies and quickly became a big flame which kept burning during the last four years. This is how I would describe my motivation to complete this PhD thesis and PhD program along a path full of obstacles but also full of learnings, discoveries and wonder. This fire would have died very shortly if it hasn't been continuously fed by the help of several extraordinary people.

First I thank my supervisors Professor Geir Hovland and Professor Mogens Blanke for their much appreciated guidance and support. They showed me directions each time I was disoriented, provided me with valuable knowledge in order to speed up my progression and encouraged me at the right times in order for me to always achieve higher results. Their contribution to my PhD project will also impact my future and I will attempt to perpetuate the positive values learnt from them.

Much of the work in my thesis has been carried out in collaboration with other researchers. I would like to give my gratitudes to all my co-authors, and a special thanks to Eivind Johansen for his practical help with building the test bench. A very special thanks to Ilya Tyapin for his fruitful collaboration.

Being a PhD student In Denmark and Norway, far away from my home town in France, was a very enjoyable experience thanks to my Phd student colleagues who became my friends. The daily Norwegian waffle times or the Danish PhD hotel evenings have been for me an unbounded source of support, inspiration and joy. Truthfully thanks to all of them, as robustness, and fault-tolerance in their friendship gave me inspiration to design a good controller.

Thanks to my family for their support, especially my brother for encouraging me to start this worthwhile journey. Thanks to my parents for giving me the desire to learn and the necessary skills for accomplishments.

Last but not least, I would like to hearty thank Kristel, for her patience, her encouragements and her affection. Never since I met her, I have been feeling alone.

Contents

Summary	i
Resumé	iii
Preface	v
Publications based on the thesis work	vii
Acknowledgements	ix
1 Introduction	1
2 Modelling of EHSS and Identification of their Parameters	7
2.1 EHSS components	8
2.2 Model	13
2.3 Parameter Estimation	26
2.4 State Space Model	60
2.5 Summary, Discussion and Conclusions	62
3 Fault Detection and Isolation	65
3.1 Residual Generator	67
3.2 Hypothesis Testing and Decision System	77
3.3 Experimental Model Validation	81
3.4 Detection and Prognosis of Faults	85
3.5 Summary and Discussion	101
4 Adaptive Nonlinear Control Design	103
4.1 Linear Control Design	103
4.2 Adaptive Backstepping	115

4.3	Experiments	143
4.4	Active Fault-Tolerant Control	149
4.5	Summary and Discussion	157
5	Conclusions and Further Research	159
5.1	Introduction	159
5.2	Major Conclusions, Discussions and Recommendations	160
5.3	Future Research Directions	162

CHAPTER 1

Introduction

With the development of fluid power during the last few decades, electro hydraulic servo systems (EHSS) are used increasingly in many industrial fields that require high actuation forces, where electric servos can not provide enough force within limited space. EHSS include among others active suspension control, braking systems, mobile hydraulic, offshore drilling equipment or pitch control system of wind turbines. For high pressure hydraulics the components can be small, light-weight and sophisticated which are necessary requirements for instance on offshore installations with limited space and load capacities.

EHSS have many and well known [3] attractive properties. Continuous improvements by using the advantages or compensating for the disadvantages of fluid power keep EHSS competitive in comparison with other forms of power. In comparison with electric motor systems, EHSS have several advantages. The size of a hydraulic motor with same power is at least 10 times smaller, it has longer service life, typically between 8000 to 10000 hours and maintenance is easier and does not require a highly skilled professional as compared to maintenance of sophisticated electronics. Regarding cooling, the hydraulic fluid evacuates the heat. EHSS offer greater protection in case of failure. In the case of exceeding load a typical system automatically goes into bypass (hydraulic fluid can flow freely between the actuator chambers), and out of bypass when the load is reduced, and in case of supply power failure, it can be designed such that it will hold the load. In comparison, for electric motor, if the load exceeds the power

capability, fuses or circuit breakers would interrupt the system. This situation can possibly damage the electrical devices and motors depending on how quick the system trips.

On the other and less glamorous side, hydraulic systems always leak. Three of the causes are pipe connector, dynamic seals and static seals. Leakage reduces efficiency and can be hazardous. Catastrophic hose failure needs obviously to be avoided but also small leakage in order to prevent contamination to water reclaim systems and pollution. Moreover leakage has a cost related to make-up fluid, clean-up and safety. When operating at high pressure, friction phenomena can not be ignored in EHSS. Because of the difficulty to model friction dynamics behaviour and to identify the varying inherent parameters, a certain amount of uncertainties are unavoidable which reduces performances of controller and fault detection. Finally noise caused by the pump and vibrations are other drawbacks of EHSS. These inherent drawbacks of EHSS, especially leakage and high friction justify the use of fault-tolerant control.

Fault-tolerant control is the adjustment of the available degrees of freedom of a system to achieve acceptable operation and prevent system failure when faults occur. Fault prognosis is the early detection of system changes and localisation of potential fault. The process of designing fault-tolerant control can be described in a step-by-step design procedure as illustrated in the following flow-chart 1.1: The motivation of this dissertation is to design a robust and fault tolerant controller for EHSS by developing and applying tools which facilitate this procedure.

EHSS are challenging to deal with for at least three reasons. First their behaviour is highly nonlinear. Linearisation of the model around an operating point gives good results only in a limited range of velocities. As a consequence a linear model based controller designed for a large set of operating points will have to be extremely robust if the plant nonlinearities are treated as uncertainties. Moreover, a too conservative controller will offer limited performances. Second, EHSS are difficult to model because of uncertain parameters, flow dynamics, temperature dependent behaviour, time varying leakage and friction, vibrations, and the inability to measure the whole system state. Finally when a high fidelity model is developed which renders the nonlinearities and uncertainties of the real plant, its complexity makes the design of controllers and fault detectors difficult to implement in practice. Even if better results are achieved in simulations, the high complexity of the controllers and detectors lead to computing time issues when implementation in real-time is not possible. Hence one has to make a trade-off between a high fidelity model which can not be used in real-time implementation and a too simple model, based on numerous assumptions which limit the control and fault detection performances. These difficulties render EHSS good candidates to exploit new possibilities and methods in the

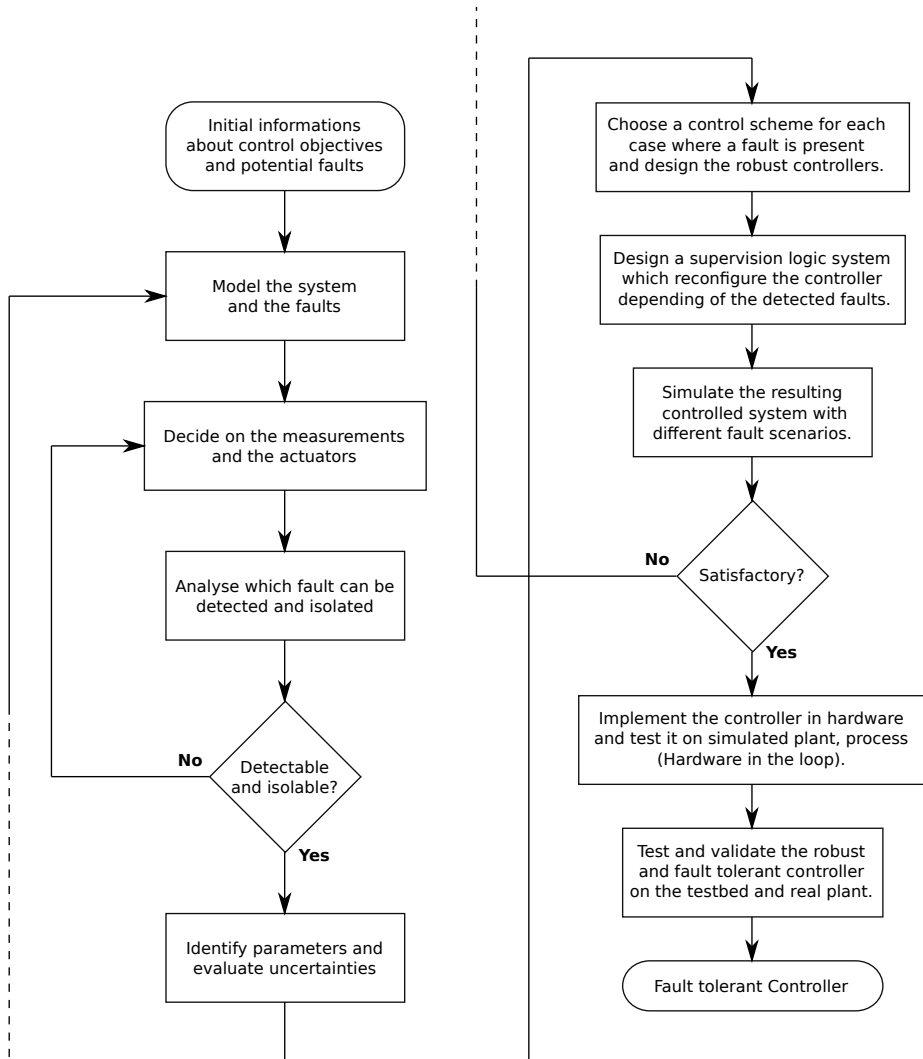


Figure 1.1: Flow chart describing the procedure used in this thesis for designing a fault-tolerant control system.

design of nonlinear and fault-tolerant controllers whose implementation lead to a renewed interest in electro hydraulic servo controlled motion systems.

The current preferred control method has historically been PID with feedforwards models or gain scheduled control for adaptive designs. However, these methods are to a large extent based on a linearisation of the system. Recent nonlinear control methods have been applied to EHSS, such as passivity based control and backstepping. Some phenomena have received less attention, for example saturation of the valve opening, dithering, and backstepping nonlinear control has been limited to some simplified models. Several improvements are taken in this dissertation, by considering model extension, higher performance controller taking into account more detailed dynamics, early fault detection and diagnosis including both simulated and experimental validation for each developed method. In this thesis, by combining control and fault detection, a fault-tolerant controller for a representative electro hydraulic servo system is achieved where the model is changed and assumptions refined depending of the fault diagnosis. Such controllers are a further development of so called “adaptive controllers” in the sense that not only parameters but the structure of the model is modified according to the system behaviour. Numerous applications would benefit from this work, from offshore drilling equipment to industrial robotic machines, through pitch controlled wind turbines.

Contributions

To solve the problem described in the previous section, this thesis develops tools for designing an active fault-tolerant controller for electro hydraulic servo systems.

A high fidelity model for a representative EHSS is developed and reproduces the static and dynamic normal behaviour of the physical system. The novelty in the model consists in taking into account the presence of friction in both the hydraulic cylinder and the servo valve together with the hydraulic film formation, the pressure dependency in the Coulomb friction and the presence of asymmetric leakage flows and openings deadbands in the servo valve. After estimation of the model parameters, the simulation results fit with the experimental ones.

Fault diagnosis techniques for EHSS are developed and implemented on a test bed. Experimental results demonstrate the ability to detect and isolate faults related to friction variation or leakages in the hydraulic cylinder or failure in the pressure sensors. Changes in residuals generated using structural analysis are detected by hypothesis testing when the system is in steady-state. Alternatively,

extended Kalman filters provide fault diagnosis for two types of leakages when the inputs, states and outputs of the system are varying.

Another contribution of the thesis is the development of a high performance adaptive nonlinear controller for EHSS and its implementation on the test bed. The inclusion of an accurate friction model in the controller design and the reduced complexity of the controller due to a cascade structure are the main improvements compared with existing backstepping controllers for such systems.

Finally the thesis describes a concrete implementation of an active fault-tolerant controller on an electro hydraulic servo controlled motion system. This architecture combines the techniques of fault diagnosis and nonlinear control developed in this thesis together with fault accommodation via active controller reconfiguration. The results demonstrate the effectiveness of the fault-tolerant control in improving the performances and safety in EHSS when faults occur.

Organisation of the Thesis

The remainder of this thesis is organised as follows. Chapter 2 presents the models and parameters estimations of an electro hydraulic servo system which are used in the next chapters of the thesis. Comparison between simulations and experiments in time and frequency domain as well as the model of the system in state space are presented. Chapter 3 continues with the design of fault detection and isolation. Residuals are generated from a structural analysis in a first section, hypothesis tests are designed and assumptions are experimentally validated in the next two sections. Finally, the designed fault detectors are implemented for different application example in a fourth section. Chapter 4 introduces the design of an adaptive nonlinear controller, using adaptive backstepping techniques, and compare the tracking performances with linear controllers. The last section of this chapter presents the overall architecture of an active adaptive fault-tolerant controller and its implementation on a test bed. Finally, chapter 5 presents the conclusion, and further research directions.

CHAPTER 2

Modelling of EHSS and Identification of their Parameters

Chapter Abstract: *This chapter presents the models and parameters which will be used later in the thesis to validate the solutions of the problems stated in chapter 1. Assumptions made in order to simplify the models are verified, a new friction model is developed and model parameters are estimated using test bed measurements for the simulation to best fit experimental data.*

Electro Hydraulic Servo Systems (EHSS) are characterised by the presence of hydraulic flow through its components and servo control valves. The dynamics of these elements exhibits nonlinear and complex behaviours which render the task of modelling particularly challenging. Depending on the performances required for the model based controller or for the fault detection and accommodation function on one hand and the real-time implementation feasibility on the other hand, the level of details for the model needs to be carefully considered to fulfil the specifications. Indeed, nonlinear controller and nonlinear observer based

fault detectors require a high fidelity model for increased performances whereas their implementation in real-time demands low complexity algorithms.

The EHSS considered in this section is a hydraulic cylinder which translates a mass attached to a spring-damper mechanical system. The system is depicted in fig. 2.1 by its hydraulic and mechanical symbols and in fig. 2.2 by a picture of the physical system on its test bed.

2.1 EHSS components

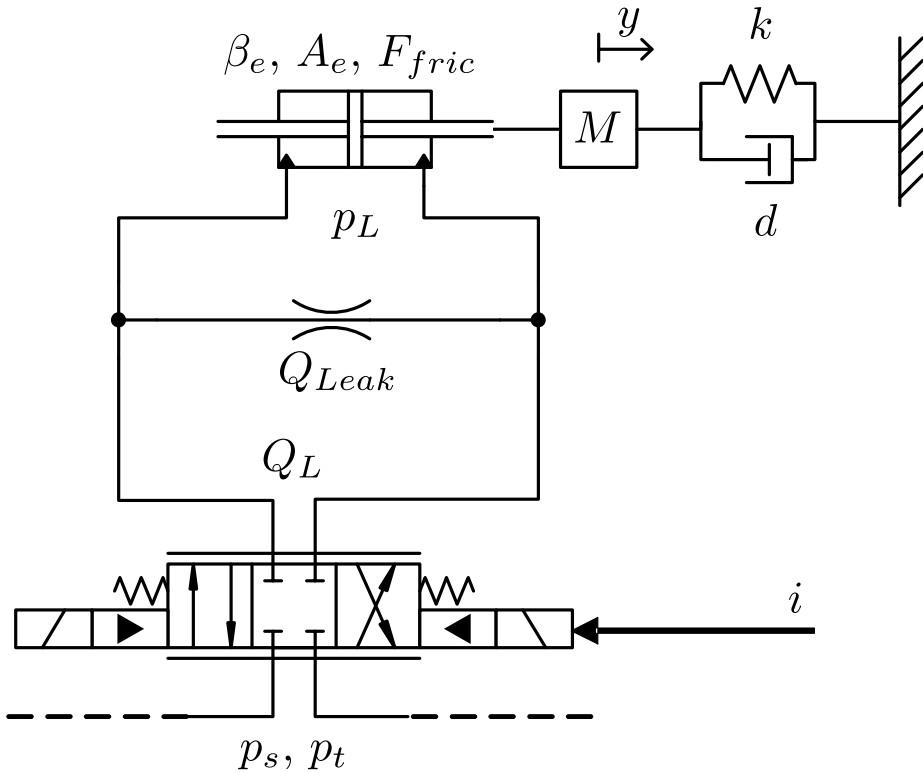


Figure 2.1: Electro Hydraulic Servo System with its parameters.

The principal components constituting the EHSS under scrutiny and numbered in fig. 2.2 are the mass (1) set into motion by linear hydraulic actuators (3) (equivalent to a single hydraulic cylinder for analysis) and attached to a spring-

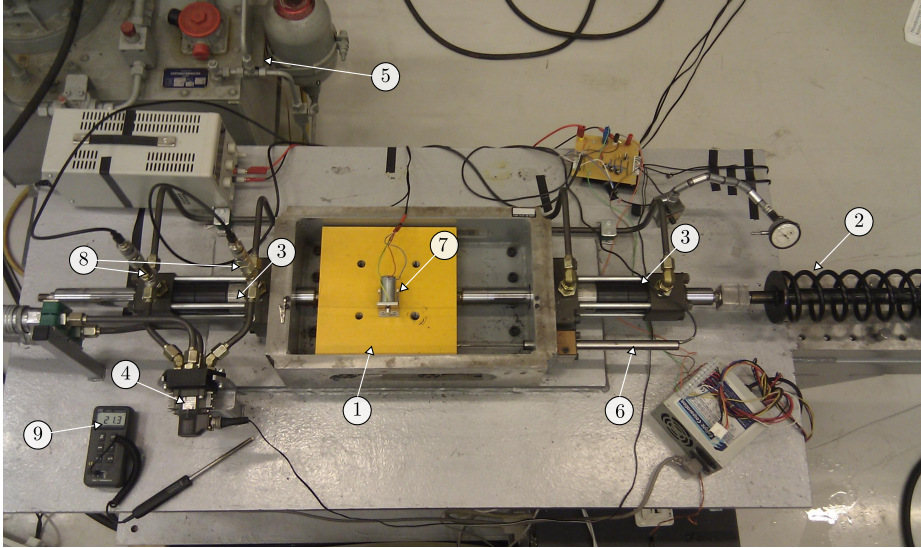


Figure 2.2: Test Bed for an Electro Hydraulic Servo System.

damper load (2). Flow through the actuator is controlled by a servo directional control valve (4) and the pressure is furnished by a hydraulic pressure unit (5) considered ideal (it delivers a constant supply pressure p_s without any flow shortcoming). A position sensor (LVDT) (6) and a linear velocity sensor (tachometer connected to a cable) (7) measure the position and velocity of the mass respectively. Finally pressure sensors (8) measure the pressures in both chambers of the cylinder and a thermometer (9) the temperature of the hydraulic fluid in the system. The parameters used in the model are summarised in table 2.1 and defined in the next paragraph.

2.1.1 Notations and Definitions

Dynamical systems will be described by differential equations of the form

$$\dot{x} = f(x, u, t)$$

for a scalar plant where $x \in \mathbb{R}$ is the system state, $u \in \mathbb{R}$ is the input signal, t denotes time, and the overdot “ \cdot ” denotes differentiation with respect to time. In the case of multiple states, bold letters will represent vectors and the differential equations can be written

$$\dot{\mathbf{x}} = f(\mathbf{x}, \mathbf{u}, t)$$

where $\mathbf{x} \in \mathbb{R}^n$ and $\mathbf{u} \in \mathbb{R}^m$.

The load pressure p_L is defined as the difference between the left chamber pressure p_a and the right chamber pressure p_b of the hydraulic cylinder:

$$p_L = p_a - p_b \quad (2.1)$$

The load pressure is normalised with respect to the supply pressure p_s :

$$p_{Ln} = \frac{p_L}{p_s} \quad (2.2)$$

The valve coefficient α is a function of the discharge coefficient C_d , the valve opening width w and the volumetric density of the hydraulic fluid ρ :

$$\alpha = C_d w \sqrt{\frac{1}{\rho}} \quad (2.3)$$

the compressibility κ of a fluid with mass density ρ and pressure p is defined as:

$$\kappa = \frac{1}{\rho} \frac{\partial \rho}{\partial p} \quad (2.4)$$

The stiffness or Bulk modulus β of the fluid is defined as:

$$\beta = \frac{1}{\kappa} \quad (2.5)$$

The compressibility coefficient β_e is defined as the ratio of four times the bulk modulus β and the total volume of fluid into consideration V_t :

$$\beta_e = \frac{4\beta}{V_t} \quad (2.6)$$

The effective area A_e for the hydraulic cylinder is the difference between the bore section area A and the rod section area a :

$$A_e = A - a = \frac{\pi}{4} (d_b^2 - d_r^2) \quad (2.7)$$

where d_b is the bore diameter of the cylinder and d_r is the rod diameter.

Table 2.1: Parameter definition

Parameter	Definition [SI Unit]	Values in Hydraulic Unit
Force balance around actuator		
M	Mass [kg]	41 kg
y_0	Initial spring deformation [m]	78.9 mm
a	Section of the rod [m ²]	2036 mm ²
A	Inside area of the cylinder [m ²]	3927 mm ²
d_b	Bore diameter of the cylinder [m]	100 mm
d_r	Rod diameter of the piston [m]	72 mm
A_e	Effective area for the cylinder [m ²]	1891 mm ²
F_h	Nominal hydraulic force [N]	15130 N
k	Spring coefficient for the load [N/m]	11220 N/m
d	Damping coefficient for the load [Ns/m]	250 Ns/m
Continuity of flow through actuator		
Q_{Leak}	Nominal leakage flow [m ³ /s]	0.5 l/min
Q_a, Q_b	Flow in, out of the cylinder [m ³ /s]	l/min
Q_L	Load flow [m ³ /s]	l/min
V_t	Total volume of fluid [m ³]	0.6 l
V_{a0}, V_{b0}	Dead volume in chamber a, b [m ³]	0.25 l, 0.35 l
s_{tr}	Cylinder stroke [m]	100 mm
β	Bulk modulus [Pa]	10665 bar
β_e	Compressibility coefficient [Pa/m ³]	71154 bar/l
p_s	Supply pressure [Pa]	80 bar
p_t	Tank pressure [Pa]	0 bar
Valve stage		
Q_n	Nominal flow [m ³ /s]	17.7 l/min
x_{vmax}	Maximal valve opening [m]	0.17 mm
x_{vn0}	Normalised valve opening offset [-]	-6.6×10^{-3}
w	Valve opening width [m]	31.4 mm
L	Valve opening parameter [m]	0.15 mm
C_d	Discharge coefficient [-]	0.6
ρ	Hydraulic fluid density [kg/m ³]	900 kg/m ³
w_v	Valve natural frequency [rad/s]	110 Hz
ζ_v	Valve damping ratio [-]	1
K_v	Valve gain [1/V]	0.16 V ⁻¹
m_v	Valve spool mass [kg]	0.1 kg
k_v	Torsion spring stiffness [N/m]	47800 N/m
d_v	Valve damping coefficient [Ns/m]	138 Ns/m
$\epsilon_{1s}, \epsilon_{1r}$	Normalised valve deadbands [-]	0, 0.003
$\epsilon_{2s}, \epsilon_{2r}$		0.005, 0.003

Continued on next page

Table 2.1 – continued from previous page

Parameter	Definition [SI Unit]	Values in Hydraulic Unit
c_{sa}, c_{at}	Leakage flows inside the valve [m ³ /s]	0.035, 0.03 l/min
c_{sb}, c_{bt}		0.035, 0.01 l/min
Friction in actuator		
σ_0	Micro stiffness friction coefficient [N/m]	6×10^7 N/m
σ_1	Micro damping friction coefficient [Ns/m]	0.1 Ns/m
σ_2	Macro damping friction coefficient [Ns/m]	80 Ns/m
v_b	Minimum friction velocity [m/s]	0.04 m/s
1) Positive velocities		
v_s	Stribeck velocity [m/s]	0.008 m/s
F_{fric}	Friction force [N]	N
F_c	Coulomb friction [N]	785 N
F_s	Stribeck friction [N]	1250 N
F_{pr}	Preload force [N]	8 N
f_{cfr}	Coulomb friction coefficient [m ²]	570 N/bar
2) Negative velocities		
σ_2	Macro damping friction coefficient [Ns/m]	0 Ns/m
v_s	Stribeck velocity [m/s]	0.005 m/s
F_c	Coulomb friction [N]	520 N
F_s	Stribeck friction [N]	1100 N
F_{pr}	Preload force [N]	365 N
f_{cfr}	Coulomb friction coefficient [m ²]	135 N/bar
1) Acceleration		
τ_h	Film thickness time constant [s]	0.2 s
2) Deceleration		
τ_h	Film thickness time constant [s]	2.5 s
Stiction in valve		
n_s	Stiction coefficient [-]	0.6
y_s	Stiction position [m]	0.003 mm
σ_{1v}	Stiction damping [Ns/m]	0.008 Ns/m
F_{st}	Stiction Stribeck force [N]	0.015 N
System states and input variables		
y	Position of the mass [m]	m
v	Velocity of the mass [m/s]	m/s
p_a, p_b	Pressure in chamber a, b of cylinder [Pa]	bar
p_L	Load pressure [Pa]	bar
p_{Ln}	Normalised pressure [-]	[-]
x_v	Valve opening [m]	mm
x_{vn}	Normalised valve opening [-]	[-]
\dot{x}_{vn}	Normalised valve opening velocity [s ⁻¹]	1/s

2.2 Model

Different levels of modelling must be chosen depending on which function a model must serve. A good model avoids unnecessary complexity and over-parametrisation but still describes the dynamical behaviour and gives a better understanding and insight of a system. In this section, each component constituting a typical EHSS is analysed by deriving its governing equations and by presenting the assumptions and simplifications made, leading to a global structure for EHSS models [16]. In the next section this structure is specialised or refined to enable simulations to generate data which fit with the ones obtained from experiments.

2.2.1 Mechanical Model

The following eq. (2.8) describes the motion of the mass M , where its acceleration \ddot{y} is related to the load pressure p_L indicated in fig. 2.1, the friction force F_{fric} created by the friction inside the cylinder and the force applied by the load F_{load} as follows:

$$\ddot{y} = \frac{1}{M} (A_e p_L - F_{fric} - F_{load}) \quad (2.8)$$

or equivalently

$$\ddot{y} = \frac{1}{M} (F_h p_{Ln} - F_{fric} - F_{load}) \quad (2.9)$$

where F_h is the nominal hydraulic force defined as $F_h = A_e p_s$. In the case of a spring-damper load,

$$F_{load} = k(y - y_0) + d\dot{y} \quad (2.10)$$

where k is the spring stiffness, y_0 is the deformation of the spring when the mass position is zero, and d is the damping coefficient whose value were identified using a calibrated tensile testing machine, see table 2.2.

2.2.2 Hydraulic Cylinder Model

The parameters describing a hydraulic single rod cylinder are shown in fig. 2.3. Q_a is the flow entering chamber a , Q_b the flow exiting chamber b and Q_{Leak} is

Table 2.2: Parameter Estimation

Parameter	Value	Confidence Interval (CI)
M [kg]	41	± 2
y_0 [mm]	78.9	± 1
A_e [mm ²]	1891	-0/+0.5
k [N/m]	11220	± 20
d [Ns/m]	250	± 250

the nominal leakage flow from chamber a to chamber b when the load pressure p_L is equal to the supply pressure p_s . When pressurised a hydraulic fluid is

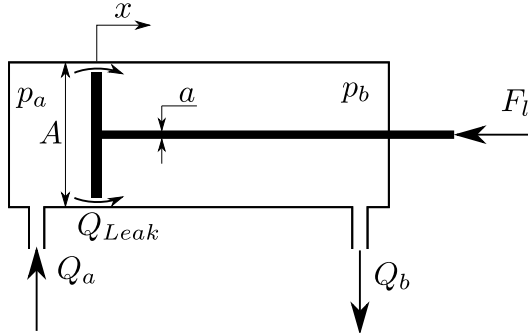


Figure 2.3: Hydraulic cylinder.

compressed causing an increase in density. This is described by means of the fluid compressibility κ and fluid stiffness or Bulk modulus β (see definitions (2.4) and (2.5)). By conservation of mass, the derivative of the pressure in each of the cylinder chambers multiplied by the fluid capacitance is given by the difference between the total flow through the chamber and the rate of increase in each chamber volume. For example if m_a and V_a are the mass of fluid and total volume respectively in chamber a :

$$m_a = \rho V_a \Rightarrow \dot{m}_a = \dot{\rho} V_a + \rho \dot{V}_a \Rightarrow \rho(Q_a - Q_{Leak}) = \frac{\rho}{\beta} \dot{p}_a V_a + \rho \dot{V}_a$$

which gives the following relations:

$$\frac{V_a}{\beta} \dot{p}_a - Q_a + Q_{Leak} p_{Ln} + Av = 0 \quad (2.11)$$

$$V_a - V_{a0} - Ay = 0 \quad (2.12)$$

$$\frac{V_b}{\beta} \dot{p}_b + Q_b - Q_{Leak} p_{Ln} - (A - a)v = 0 \quad (2.13)$$

$$V_b - V_{b0} + (A - a)y = 0 \quad (2.14)$$

where V_a , V_b are the total volumes on each side of the cylinder and V_{a0} , V_{b0} the constant dead volumes on each side including hose volumes.

Assumptions In the case of double rod cylinder, i.e. symmetrical actuator, making the assumption of equal flow entering the cylinder as flow leaving it, eqs. (2.11-2.14) become:

$$\frac{V_t}{4\beta} \dot{p}_L = Q_L - Q_{Leak} p_{Ln} - A_e v \quad (2.15)$$

where $V_t = V_{a0} + V_{b0} + s_{tr} A_e$ is the total volum of fluid. By normalising the load pressure and load pressure rate by the supply pressure, the flow continuity equation can be written:

$$\dot{p}_{Ln} = \frac{\beta_e}{p_s} (Q_L - Q_{Leak} p_{Ln} - A_e v) \quad (2.16)$$

2.2.3 Valve Model

A drawing of an electrically operated, 2-stage servo directional control valve as given in Bosch-Rexroth data-sheet (RE 29564-XN-100-B2/02.09) is shown in fig. 2.4. The valve consists of a torque motor (1), a flapper between a double-nozzle which plays the role of a hydraulic amplifier (2) and a control piston in a sleeve (3) which is connected to the torque motor via a cantilever spring (9).

2.2.3.1 Flow Equations

The control piston (3) in fig. 2.4 in a sleeve with position $x_v = 0$ can further be schematically represented as in fig. 2.5 where spool overlap and underlap can be considered varying the ε_i parameters, $\varepsilon_{1s} = \varepsilon_{1r} < 0$ for a symmetric overlap and $\varepsilon_{1s} = \varepsilon_{1r} > 0$ for a symmetric underlap. Since most flow occurs

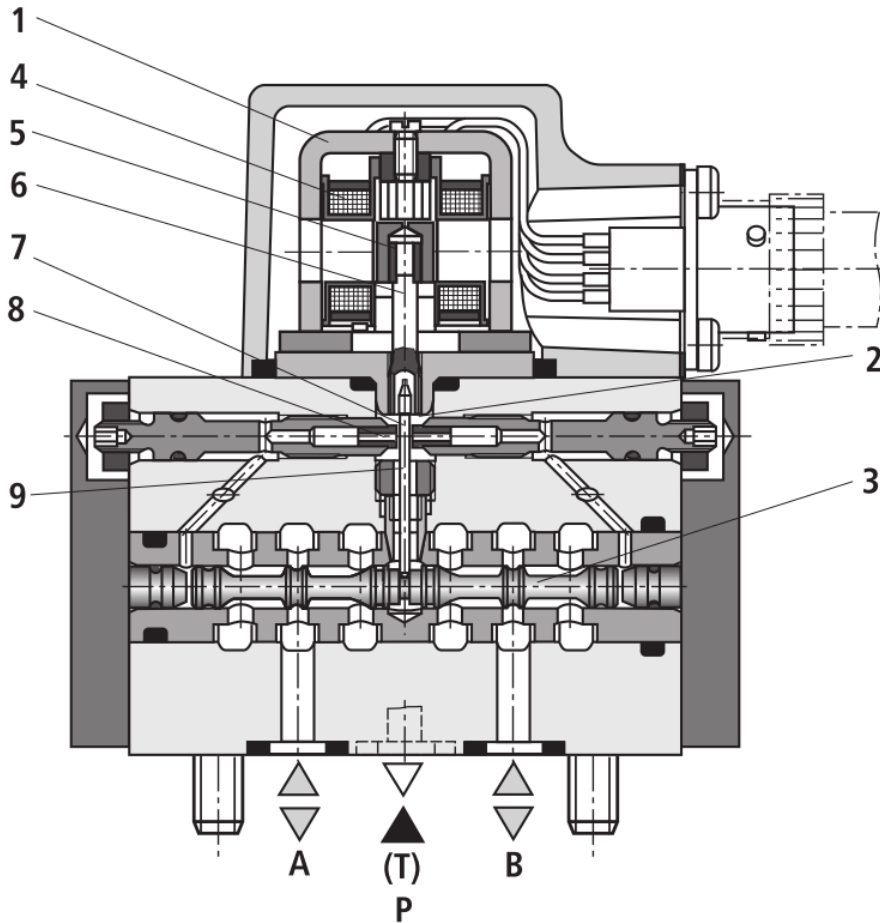
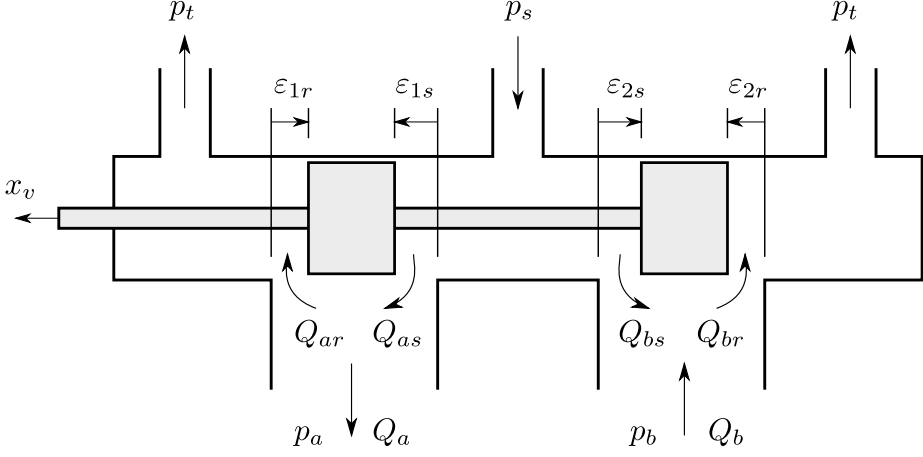


Figure 2.4: Bosch-Rexroth electrically operated 2-stage servo directional control valve with torque motor (1) and its coils (4) generating a force on the armature (5) and acting by means of a torque tube (6) on a hydraulic amplifier (2) composed of a flapper plate (7) between two control orifices (8). The pressure differential causes the position of the control piston in sleeve (3) to change, acting on a torsion spring (9).

Figure 2.5: Control piston with position $x_v = 0$ in a sleeve.

at high Reynolds numbers inside the valve, the following relations between the turbulent flow, the valve opening and the pressure drop hold:

$$\begin{aligned}
 Q_a &= Q_{as} - Q_{ar} \\
 &= \alpha \left(\text{sign}(p_s - p_a) \sqrt{|p_s - p_a|} u(x_v, \varepsilon_{1s}, L) \right. \\
 &\quad \left. - \text{sign}(p_a - p_t) \sqrt{|p_a - p_t|} u(-x_v, \varepsilon_{1r}, L) \right)
 \end{aligned} \tag{2.17}$$

$$\begin{aligned}
 Q_b &= Q_{br} - Q_{bs} \\
 &= \alpha \left(\text{sign}(p_b - p_t) \sqrt{|p_b - p_t|} u(x_v, \varepsilon_{2r}, L) \right. \\
 &\quad \left. - \text{sign}(p_s - p_b) \sqrt{|p_s - p_b|} u(-x_v, \varepsilon_{2s}, L) \right)
 \end{aligned} \tag{2.18}$$

where $\alpha = C_d w \sqrt{2/\rho}$ and where the saturation function u is defined as follows:

$$u(x_v, \varepsilon, L) = \begin{cases} 0 & \text{for } x_v \leq -\varepsilon \\ x_v + \varepsilon & \text{for } -\varepsilon < x_v < L \\ L & \text{for } L \leq x_v \end{cases} \tag{2.19}$$

In the case of critical centre valves ($\varepsilon_{1s} = \varepsilon_{1r} = 0$),

$$\begin{aligned} Q_a &= Q_{as} - Q_{ar} \\ &= \alpha \left(\text{sign}(p_s - p_a) \sqrt{|p_s - p_a|} u(x_v, L) \right. \\ &\quad \left. - \text{sign}(p_a - p_t) \sqrt{|p_a - p_t|} u(-x_v, L) \right) \end{aligned} \quad (2.20)$$

$$\begin{aligned} Q_b &= Q_{br} - Q_{bs} \\ &= \alpha \left(\text{sign}(p_b - p_t) \sqrt{|p_b - p_t|} u(x_v, L) \right. \\ &\quad \left. - \text{sign}(p_s - p_b) \sqrt{|p_s - p_b|} u(-x_v, L) \right) \end{aligned} \quad (2.21)$$

where u , the new saturation function is defined as follows:

$$u(x_v, L) = \begin{cases} 0 & \text{for } x_v \leq 0 \\ x_v & \text{for } 0 < x_v < L \\ L & \text{for } L \leq x_v \end{cases} \quad (2.22)$$

2.2.3.2 Symmetric Actuator

In the case of symmetric actuators, for instance a double rod hydraulic cylinder, the model for the valve can be simplified, i.e. the number of variables reduced, if the assumption of incompressible hydraulic fluid is taken when considering the flow equations. Indeed, the flow entering and leaving the actuator is the same and is called Q_L , the load flow. Depending on the sign of the valve opening, two cases need to be considered:

- For $x_v \geq 0$, $p_s \geq p_a$ and $p_b \geq p_t$, eqs. (2.20) and (2.21) give:

$$\begin{aligned} Q_a &= Q_b = Q_L \\ \Rightarrow p_s - p_a &= p_b - p_t \end{aligned}$$

Since $p_L = p_a - p_b$, an expression for p_b is:

$$\Rightarrow p_b = \frac{p_s + p_t - p_L}{2}$$

which implies:

$$\Rightarrow Q_L = \frac{\alpha}{\sqrt{2}} \sqrt{p_s - p_t - p_L} u(x_v, L) \quad (2.23)$$

- For $x_v \leq 0$, $p_s \geq p_b$ and $p_a \geq p_t$:

$$\begin{aligned}
 Q_a &= Q_b = Q_L \\
 \Rightarrow p_s - p_b &= p_a - p_t \\
 \Rightarrow p_a &= \frac{p_s + p_t + p_L}{2} \\
 \Rightarrow Q_L &= -\frac{\alpha}{\sqrt{2}} \sqrt{p_s - p_t + p_L} u(-x_v, L)
 \end{aligned} \tag{2.24}$$

Finally, considering the tank pressure equal to zero, $p_t = 0$, and $0 \leq p_i \leq p_s$, $i = a, b$, the load flow Q_L can be written:

$$Q_L = \frac{\alpha}{\sqrt{2}} \sqrt{p_s - \text{sign}(x_v) p_L} \text{sat}(x_v, L) \tag{2.25}$$

where the saturation function sat is defined as follows:

$$\text{sat}(x_v, L) = \begin{cases} x_v & \text{for } -L < x_v < L \\ L & \text{for } L \leq x_v \\ -L & \text{for } x_v \leq -L \end{cases} \tag{2.26}$$

Another expression for the load flow can be obtained when considering the nominal flow Q_n given in data-sheets, which is the flow when the valve piston is fully open and the load pressure is zero. For zero tank pressure:

$$\begin{aligned}
 Q_n &= Q_L(x_v = x_{v\max}, p_L = 0) = \alpha \sqrt{\frac{p_s}{2}} x_{v\max} \\
 \Rightarrow Q_L &= Q_n \sqrt{1 - \text{sign}(x_{vn}) p_{Ln}} \text{sat}\left(x_{vn}, \frac{L}{x_{v\max}}\right)
 \end{aligned} \tag{2.27}$$

Hydraulic losses in pipes Whether or not to neglect the losses in pipes when modelling an EHSS needs to be carefully considered. In this paragraph the pressure drop is calculated at different flow rates for the test bed shown in fig. 2.2. According to the manufacturer hydraulic fluid density is $\rho = 900 \text{ kg/m}^3$, and kinematic coefficient of viscosity is $\nu = 50 \text{ mm}^2/\text{s}$ at $T = 30^\circ\text{C}$. The volumetric flow q_v varies from 0 to $Q_n = 17 \text{ l/min}$ through $L = 2 \text{ m}$ of $d = 10 \text{ mm}$ diameter drawn tubing pipes between the servo valve and the cylinders. Seven 90° regular elbows and three tees are present in addition to the straight pipes. First the Reynolds number is computed:

$$Re = vd/\nu = 4q_v/(\pi d\nu) = 1130|_{q_v=Q_n} \tag{2.28}$$

The flow being laminar the friction factor f can be expressed as $f = 64/Re$. Then the head loss is:

$$h_f = f \frac{L}{d} \frac{v^2}{2g} + K_L \frac{v^2}{2g} \quad (2.29)$$

where g is gravity and $K_L = 5$ is the loss coefficient related to the elbows and tees. Therefore the pressure drop is:

$$\Delta_p = \rho g h_f = 8 \frac{\rho K_L q_V^2}{\pi^2 d^4} + 128 \frac{\rho q_V \nu L}{\pi d^4} \quad (2.30)$$

The pressure drop across the pipes from the valve to the cylinders is hence approximately equal to 0.2 bar for a 5l/min flow and 1 bar at nominal flow. It follows that the hydraulic losses in pipes have a limited effect on the system and hence can be neglected when considering a simple model of EHSS.

2.2.3.3 Dynamics

A complete model for a similar valve was derived in [25] and linearised around zero input current. It leads to a fifth order model for the valve dynamics where the five states are angular position and velocity of the flapper, difference of pressure between each side of the valve spool, spool position and velocity, see fig. 2.4. Modelling the dynamics of an electro hydraulic servo valve with a fifth order transfer function as in [25] revealed to be necessary in order to design a linear controller to achieve high bandwidth tracking performance, however in the case of nonlinear control, the model of the valve must be reduced in order to reduce the complexity of the controller when regarding real-time implementation issues, see chapter 4 for more details. Therefore servo valve dynamics has been considered in the design of nonlinear controller to various extent. Some authors neglect the spool valve resonance, the flow forces on the spool or the pressure feedback on the flapper and use a third order model as in [29], others ignore the dynamics of the first stage and use a second order model [44], [36], others consider first order model [14] or no dynamics [45], [1]. Nevertheless the importance of including an accurate model of dynamic characteristics of the servo valve was shown already in the early 1970s [34] and its influence on position control can easily be verified. Two models and their performances will be considered in chapter 4 when designing a nonlinear controller. The first one is given by a simple proportional gain, $x_{vn} = K_v u_n$ while the second one is the second order model:

$$\ddot{x}_{vn} = \frac{-k_v}{m_v} x_{vn} + \frac{-d_v}{m_v} \dot{x}_{vn} + K_v \frac{k_v}{m_v} i \quad (2.31)$$

or equivalently:

$$\ddot{x}_{vn} = -\omega_v^2 \left(\frac{2\zeta_v}{\omega_v} v_{vn} + x_{vn} - i_n \right) \quad (2.32)$$

where m_v is the mass of the spool, k_v the torsion spring stiffness, d_v a damping factor, $\omega_v = \sqrt{k_v/m_v}$ and $\zeta_v = d_v/(2m_v\omega_v)$ are respectively the natural frequency and damping ratio of the valve, and where u_n is the normalised voltage input to the voltage-to-current converter placed before the servo valve: $u_n = u/u_{max}$ where u_{max} is the limit voltage beyond which the valve saturates.

Remark The input signal to the servo valve coils is actually a current i considered as directly proportional to the input voltage before the voltage-to-current converter. Therefore when normalised, $u_n = i_n$.

2.2.4 Friction Model

Excessive friction in hydraulic cylinders is an unwanted force. It is caused by the presence of elastomeric seals between piston rod and cylinder bore interfaces required to prevent leaks and hence to ensure high difference of pressure between the two cylinder chambers. The contact materials in hydraulics differ from usual mechanical systems where friction is due to motion of transmission element as for example gear or roller bearings where contacts are metal on metal with lubricants.

2.2.4.1 Static Friction Model

Friction is often considered as the sum of a constant force (Coulomb friction), a force proportional to the relative motion velocity (viscous friction) and a force present at low velocity (Stribeck friction). Static models provide an expression of the friction force for a constant relative velocity. A usual expression for hydraulic friction is:

$$\begin{aligned} F_{fric} &= \left(F_c + (F_s - F_c)e^{-|v|/v_s} \right) \text{sign}(v) + \sigma_2 v \\ F_c &= F_{pr} + f_{cfr}(p_a + p_b) \end{aligned} \quad (2.33)$$

where $F_c \text{sign}(v)$ is Coulomb friction, $(F_s - F_c)e^{-|v|/v_s} \text{sign}(v)$ is Stribeck friction and $\sigma_2 v$ is viscous friction. Parameters F_{pr} and F_s can be considered constant or position dependent for more accurate models.

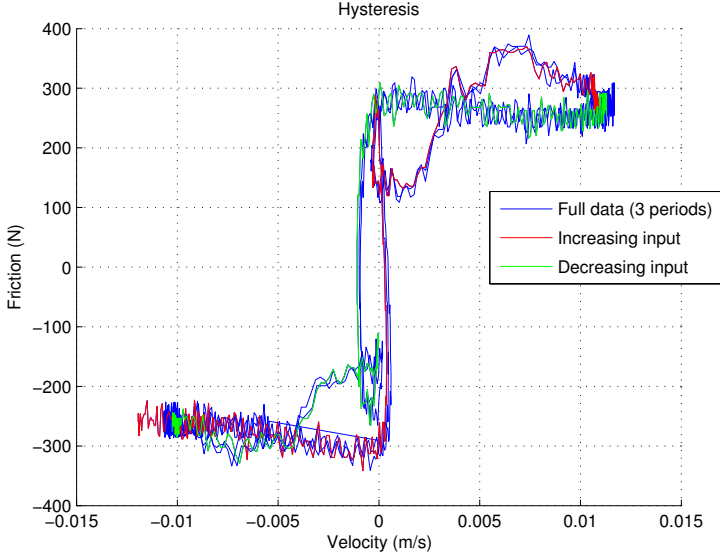


Figure 2.6: Hysteresis in friction force.

Remark Other models for static friction exist, for instance in [9] where hydraulic friction force is a function of the pressures in the hydraulic cylinder and is velocity independent.

2.2.4.2 LuGre Model

Static models are not sufficient to explain dynamic behaviour, such as varying break away force or hysteresis. As an example, fig. 2.6 illustrates the need of a dynamical friction model when the input is varying, a sine wave $u(t) = 0.5 \sin(10t)$ in this case, since a static model is not able to fit the experimental data.

The LuGre model [11] is described by the following equations:

$$F_{fric} = \sigma_0 z + \sigma_1 \dot{z} + \sigma_2 v \quad (2.34)$$

$$\dot{z} = v - \frac{|v|}{g(v)} z \quad (2.35)$$

$$g(v) = \frac{F_c}{\sigma_0} + \frac{F_s - F_c}{\sigma_0} e^{-|v|/v_s} \quad (2.36)$$

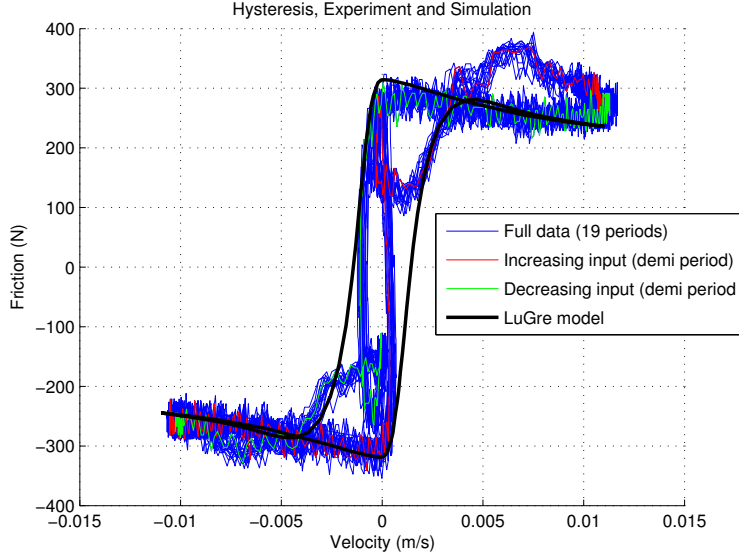


Figure 2.7: Comparison between experimental (blue, red, green) and simulated (black) data with LuGre friction model.

where z is an internal state variable representing the bristle micro displacement, σ_0 the bristle stiffness and σ_1 the microdamping. Using this dynamic friction model, it is possible to capture some of the dynamics of real friction behaviour as shown in fig. 2.7 where a simulated model of the EHSS using LuGre friction is compared to real data. However some phenomena are not explained by this model at low velocity or at velocities above 5mm/s where the friction is different if the mass accelerates or decelerates.

2.2.4.3 Modified LuGre Model

In order for the friction model to capture the differences of friction forces when the mass is accelerating or decelerating, the lubricant film thickness dynamics can be considered as in [42], where the authors consider not only the lag behaviour resulting from solid friction but also that resulting from the lubricant film formation, with variable thickness called h . The function g describing the

Stribeck effect is modified as follows:

$$\dot{h} = \frac{1}{\tau_h}(h_{ss} - h) \quad (2.37)$$

$$\dot{z} = v - \frac{\sigma_0|v|}{g(v, h)}z \quad (2.38)$$

$$g(v, h) = F_c + [(1 - h)F_s - F_c]e^{-|v|/v_s} \quad (2.39)$$

where τ_h is the lubricant film thickness time constant and h_{ss} is the dimensionless steady-state film thickness expressed as:

$$h_{ss} = K_f|v|^{2/3} \quad (v \leq v_b) \quad (2.40)$$

where K_f is a proportional constant and v_b is the velocity at which the magnitude of the steady-state force becomes minimum. Beyond the velocity v_b the film thickness is unchanged.

2.2.5 Model Linearisation

Using the first order term of a Taylor expansion, the nonlinear model can be linearised around a local operating point of the system. Tools for studying linear systems can be used thereafter to analyse the behaviour of the nonlinear system on a neighbourhood of an equilibrium. However, with increasing amplitudes the contribution from the nonlinearities is increasing leading to large discrepancies. Therefore, a linear model is developed in this section which will be used in the rest of the thesis when comparing nonlinear with linear techniques.

The flow equation in 2.27 can be linearised around zero normalised load pressure $p_{Ln} = 0$ and with a small opening $x_v = \epsilon$ as follows:

$$\begin{aligned} Q_L &= Q_n \sqrt{1 - \text{sign}(x_{vn})p_{Ln}x_{vn}} \\ \Rightarrow Q_{Llin} &= \left. \frac{\partial Q_L}{\partial x} \right|_{(x_{vn}, p_{Ln})=(\epsilon, 0)} x_{vn} + \left. \frac{\partial Q_L}{\partial p_{Ln}} \right|_{(x_{vn}, p_{Ln})=(\epsilon, 0)} p_{Ln} \\ \Rightarrow Q_{Llin} &= Q_n x_{vn} - Q_n \text{sign}(x_{vn}) \frac{\epsilon}{2} p_{Ln} \end{aligned}$$

The system (2.9, 2.15, 2.27, 2.32) without load, Coulomb nor Stribeck friction,

with a critical centre valve becomes:

$$\dot{y} = v \quad (2.41)$$

$$\dot{v} = \frac{-\sigma_{2l}}{M}v + \frac{F_h}{M}p_{Ln} \quad (2.42)$$

$$\dot{p}_{Ln} = \frac{-\beta_e A_e}{p_s}v - \beta_e \left(\frac{Q_{Leak}}{p_s} + \frac{Q_n}{p_s} \text{sign}(x_{vn}) \frac{\epsilon}{2} \right) p_{Ln} + \frac{\beta_e Q_n}{p_s} x_{vn} \quad (2.43)$$

$$\dot{x}_{vn} = v_{vn} \quad (2.44)$$

$$\dot{v}_{vn} = -\omega_v^2 \left(\frac{2\zeta_v}{\omega_v} v_{vn} + x_{vn} - i_n \right) \quad (2.45)$$

where σ_{2l} is the value of the viscous friction when the Coulomb friction is neglected. The transfer function from input i to position y is the following:

$$G(s) = G_1(s)G_2(s)G_3(s) \quad (2.46)$$

where G_1 , G_2 and G_3 are the transfer functions from velocity v to position y , from normalised valve opening x_{vn} to velocity v and from input i to normalised valve opening x_{vn} and are given by the following expressions in the Laplace domain:

$$G_1(s) = \frac{1}{s} \quad (2.47)$$

$$G_2(s) = \frac{K_2}{s^2/\omega_{hyd}^2 + (2\zeta_{hyd}/\omega_{hyd})s + 1} \quad (2.48)$$

$$G_3(s) = \frac{K_v}{s^2/\omega_v^2 + (2\zeta_v/\omega_v)s + 1} \quad (2.49)$$

where K_2 , ζ_{hyd} and ω_{hyd} are respectively the hydraulic gain, damping ratio and eigenfrequency:

$$K_2 = \frac{F_h \beta_e Q_n}{p_s M}, \quad \omega_{hyd} = \sqrt{\frac{\beta_e (2F_h A_e + Q_n \epsilon \sigma_{2l} + 2Q_{Leak} \sigma_{2l})}{2p_s M}}$$

$$\zeta_{hyd} = \frac{\sqrt{2}}{4} \frac{\beta_e Q_n \epsilon M + 2\beta_e Q_{Leak} M + 2p_s \sigma_{2l}}{\sqrt{p_s M \beta_e (2F_h A_e + Q_n \epsilon \sigma_{2l} + 2Q_{Leak} \sigma_{2l})}}$$

The linearised system contains an open-loop integrator and two second order poles.

Remark 1 When the leakage flow and the valve opening ϵ are small, the hydraulic damping ratio and eigenfrequency can be approximated by:

$$\omega_{hyd} = 2A_e \sqrt{\frac{\beta}{V_t M}}, \quad \zeta_{hyd} = \frac{1}{4} \frac{\sigma_{2l}}{A_e} \sqrt{\frac{V_t}{\beta M}}$$

Remark 2 In order to take into account the Coulomb friction in the hydraulic cylinder, a factor $\eta_{hmc} < 1$ which represents the hydro-mechanical efficiency of the cylinder can be added in eq. (2.42):

$$\dot{v} = \frac{-\sigma_{2l}}{M}v + \frac{\eta_{hmc}F_h}{M}p_{Ln} \quad (2.50)$$

2.3 Parameter Estimation

With the help of the measurements taken on the test bed shown in fig. 2.8, the parameters of the model developed in the previous section can be estimated using system identification. When the identification fails to give accurate enough results, the model structure is specialised to render the real dynamic behaviour of the system.

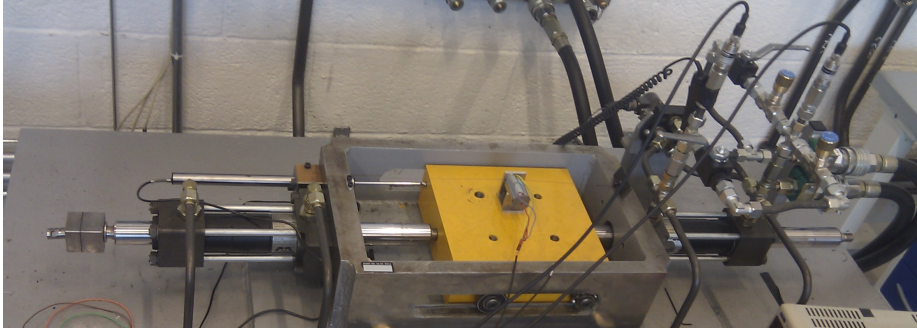


Figure 2.8: Experimental setup for EHSS identification.

The parameters in table 2.3 are directly accessible via measurement or from the manufacturer datasheet. The confidence intervals given in this section for each parameter estimation have not been strictly calculated based on a confidence level, but only estimated by repeating the experiments three times and by including the tolerance intervals issued from the datasheets. They should only be taken as a rough indication on the parameters reliability.

2.3.1 Static Parameters Estimation

Due to the complex nature of friction, orifice flows, leakages and servo valves, several assumptions have been made to derive eqs. (2.8), (2.16), (2.27) and (2.32). Using a system identification approach, experimental data are used to

Table 2.3: Parameter estimation

Parameter	Value	Confidence Interval (CI)
p_s [bar]	80	± 2
β [bar]	10665	± 2000
β_e [bar/l]	71154	± 10000
V_{a0} [l]	0.25	± 0.1
V_{b0} [l]	0.35	± 0.1
V_t [l]	0.6	± 0.1

validate the assumptions, to estimate the parameters and to refine the model structure, while taking into consideration the model complexity and real-time implementation. First the static parameters are estimated in order for the model to fit the steady-state behaviour. In steady-state, when the load pressure, mass velocity and valve opening are constant, eqs. (2.8), (2.16) (2.27) and (2.32) become:

$$0 = F_h p_{Ln} - F_{fric}^{ss} - F_{load} \quad (2.51)$$

$$0 = Q_L - Q_{Leak} p_{Ln} - A_e v \quad (2.52)$$

$$Q_L = Q_n \sqrt{1 - \text{sign}(x_{vn}) p_{Ln} \text{sat} \left(x_{vn}, \frac{L}{x_{v\max}} \right)} \quad (2.53)$$

$$0 = x_{vn} - u_n \quad (2.54)$$

The static parameters which can hence be estimated in steady-state are the nominal flow Q_n , the nominal internal leakage flow Q_{Leak} and the static parameters of the friction model. System identification is realised by the mean of the experimental setup shown in fig. 2.2 or in fig. 2.8, where the load has been removed in order to reduce uncertainty. Using a sequence of n stairs as input, the mass is moved from one end to the other at n different constant velocities and for each stair the measurements are recorded and averaged after an adequate transition time.

2.3.1.1 Estimation of static flow and valve parameters

The results from this experiment show that for zero valve opening the mass is moved in the negative direction, which demonstrates the presence of a valve offset x_{vn0} . Adding this offset in the model eqs. (2.16), (2.27) and (2.32) result

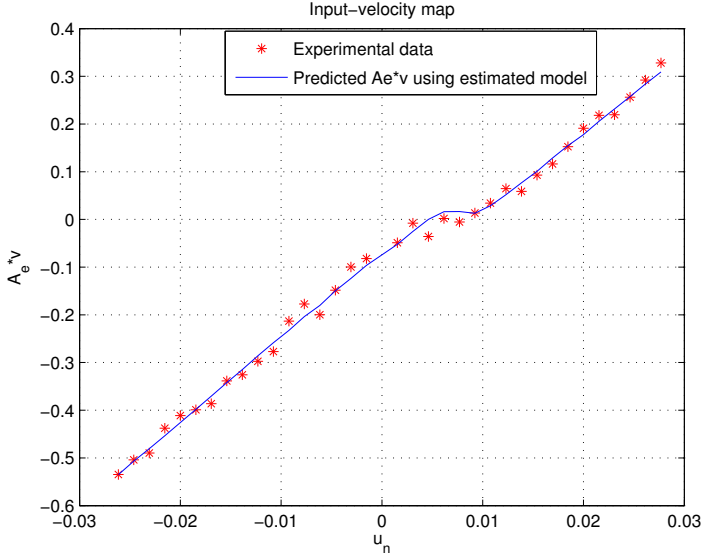


Figure 2.9: Nominal flow estimation.

in the following relation when the valve does not saturate:

$$\begin{aligned}
 A_e v &= Q_n \sqrt{1 - \text{sign}(u_n) p_{Ln}} (u_n + x_{vn0}) - Q_{Leak} p_{Ln} \\
 \Rightarrow A_e v &= \begin{bmatrix} \sqrt{1 - \text{sign}(u_n) p_{Ln}} u_n & \sqrt{1 - \text{sign}(u_n) p_{Ln}} & -p_{Ln} \end{bmatrix} \begin{bmatrix} Q_n \\ Q_n x_{vn0} \\ Q_{Leak} \end{bmatrix} \quad (2.55)
 \end{aligned}$$

With the experimental data registered for the n stairs, the values of Q_n , Q_{Leak} and x_{vn0} are estimated using linear least square method to best fit the data set. For temperature $T = 30^\circ\text{C}$ and supply pressure $p_s = 80$ bar, these values are given in table 2.1. Fig. 2.9 shows the input-velocity map for 35 different voltage inputs in steady-state from both the experimental data and from the model with estimated parameters. Repeating the same experiment at different temperatures, the dependence of these parameters with temperature is established and their variations are displayed in fig. 2.10. It is shown in fig. 2.10(a) that the nominal load flow Q_n increases by about 25% when the temperature is increased from 22°C , to 34°C , where this change of temperature corresponds to a 50% decrease in the fluid viscosity. This behaviour is resulting from the presence of a laminar flow, showing that the flow through the valve orifice is not completely turbulent. The Reynolds number needs hence to be calculated.

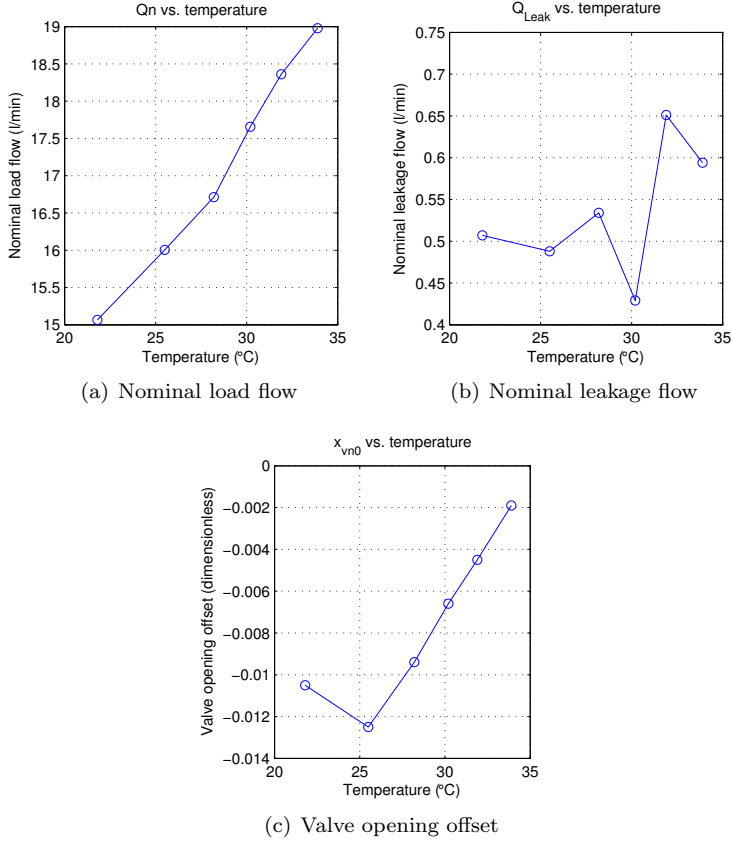


Figure 2.10: Variation of estimated static flow and valve parameters with temperature.

Low Reynolds number When the fluid velocity through the valve orifice is small, the flow becomes laminar, and eq. (2.27) is no longer valid. However it can still be a good representation for the flow if the discharge coefficient C_d , instead of being constant, is decreased as the Reynolds number Re decreases. See a typical plot of a discharge coefficient versus Reynolds number for an orifice in fig. 2.11 and [20]. For $\sqrt{Re} < 10$, experimental results [20] show that the discharge coefficient is directly proportional to the square root of Reynolds number:

$$C_d = \delta \sqrt{Re} \quad (2.56)$$

Table 2.4: Parameter estimation

Parameter	Value	Confidence Interval (CI)
Q_n [l/min]	17.7	± 1
Q_{Leak} [l/min]	0.5	± 0.1
x_{vn0} [-]	-0.0066	± 0.002

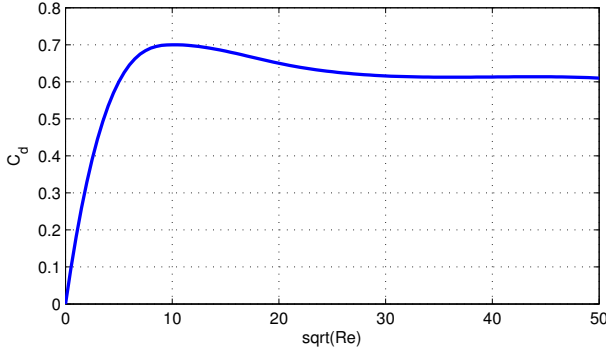


Figure 2.11: Plot of a discharge coefficient versus Reynolds number for an orifice.

The Reynolds number can be computed as:

$$Re = \frac{v_{or} d_H}{v} \quad (2.57)$$

where v is the kinematic viscosity [m^2/s], d_H is the hydraulic diameter and v_{or} , the fluid velocity in the orifice:

$$v_{or} = \frac{Q_L}{w x_v}, \quad d_H = \frac{4 x_v w}{2w} = 2x_v \quad (2.58)$$

Hence the Reynolds number is also:

$$Re = \frac{2Q_L}{wv} = \frac{2\delta\sqrt{Re}}{wvC_d} Q_n \sqrt{1 - \text{sign}(x_{vn})p_{Ln}x_{vn}} \quad (2.59)$$

which implies:

$$\sqrt{Re} = \frac{2\delta}{wvC_d} Q_n \sqrt{1 - \text{sign}(x_{vn})p_{Ln}x_{vn}} \quad (2.60)$$

The condition $\sqrt{Re} < 10$ is hence equivalent to:

$$Q_n \sqrt{1 - \text{sign}(x_{vn})p_{Ln}x_{vn}} < 10 \frac{wvC_d}{2\delta} \quad (2.61)$$

or:

$$Q_n \sqrt{1 - \text{sign}(x_{vn}) p_{Ln} x_{vn}} < 3.71/\text{min} \quad (2.62)$$

A more precise model can hence be obtained by considering the regime of the orifice flow as indicated in fig. 2.12. Up to 20% of the maximum valve opening, the flow inside the valve orifice is composed of a turbulent and a laminar flow, whereas for larger opening the flow can be considered as purely turbulent.

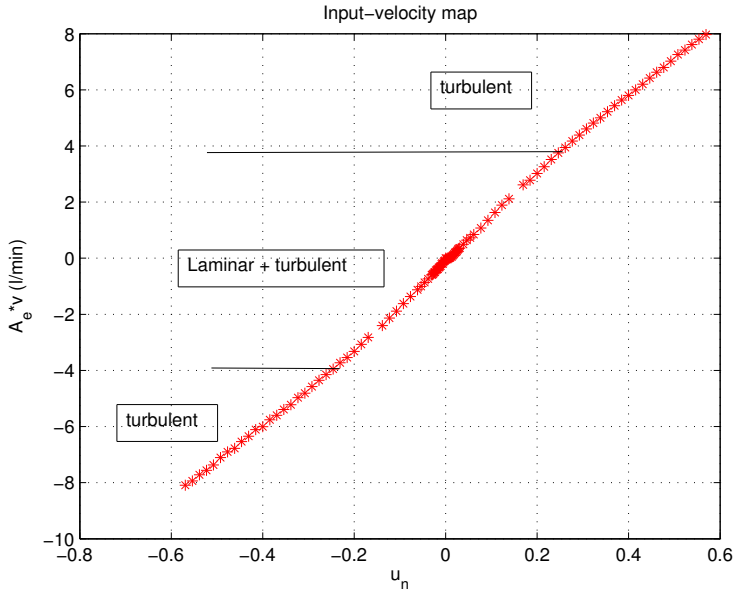
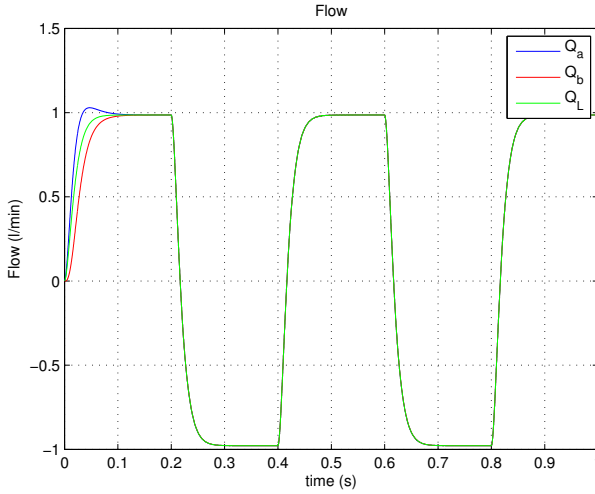
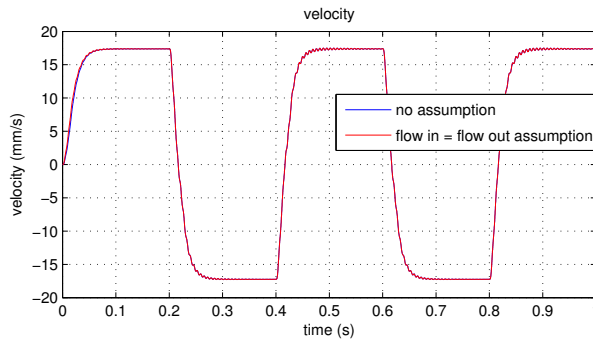


Figure 2.12: Input-velocity map from experimental data in steady-state with flow regime area.

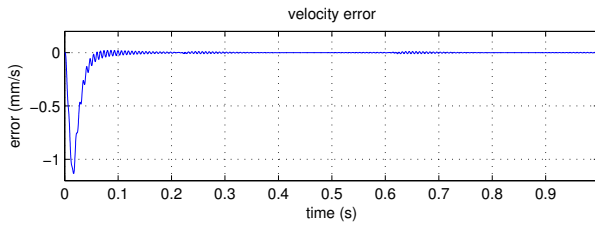
Flow in equals flow out In order to verify the validity of the assumption 'flow in equals flow out' in the cylinder, simulation of the system in fig. 2.1 is run with or without the assumption. The input signal for the simulation is a pulse with period 0.4s, amplitude 0.1V, centred on 0V and with 50% width. When it is not assumed that the flow in equals the flow out, $Q_a \neq Q_b$, during the first 100ms, the simulation shows an error in the velocity of 1 mm/s (7% relative error), see fig. 2.13. Once the pressure has built up in the cylinders chambers, the error can then be neglected (0.07% relative error) which validates the assumption of equality between the flow in and out of the cylinder.



(a) Flow



(b) Velocity



(c) Velocity error

Figure 2.13: Comparison between models with or without the assumption “flow in equals flow out” of the symmetrical cylinder. Input signal in the valve is a pulse with period $T = 0.4\text{s}$ and amplitude $A = 0.1\text{V}$. First model: flow in ($= Q_a$) and flow out ($= Q_b$). Second model $Q_L = Q_a = Q_b$.

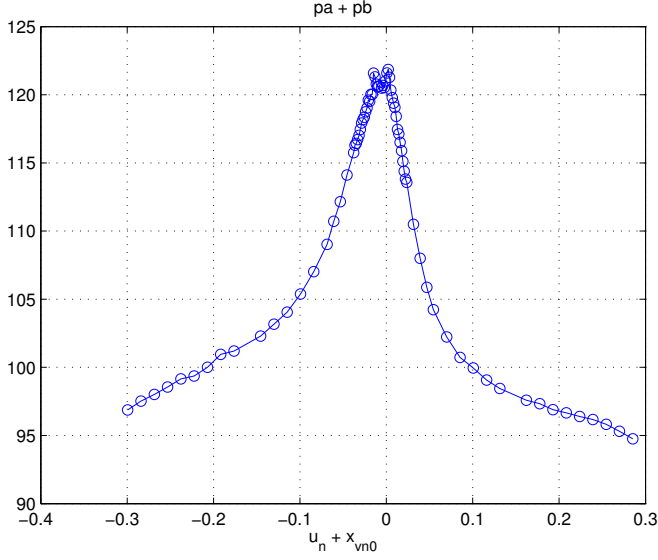


Figure 2.14: Sum of chamber pressures for different valve openings in steady-state.

Non-symmetric underlap valve For critically centred valve, the sum of the chamber pressures $p_a + p_b$ is constant and equal to the supply pressure $p_s = 80$ bar. However, the experimental measures of p_a and p_b are not in accordance with this assumption as shown in fig. 2.14 where the pressures sum up to 120 bar for small valve openings and down to 90 bar for larger openings. It can also be noticed that the sum of the pressures are not symmetrical for positive and negative valve openings. In order for the model to capture this behaviour, a non-symmetric underlap valve needs to be considered with additional leakage flow around the valve spool. The real flows inside the valve around zero opening are difficult to identify and numerous trials and errors are necessary to estimate parameters. Introducing laminar leakages between the valve openings which are independent of the valve spool, eqs. (2.17) and (2.18) are rewritten as follows:

$$Q_a = \sqrt{2}Q_n \left(\sqrt{1 - p_{an}}u(x_{vn}, \varepsilon_{1s}, L) + (1 - p_{an})c_{sa} - \sqrt{p_{an}}u(-x_{vn}, \varepsilon_{1r}, L) - p_{an}c_{at} \right) \quad (2.63)$$

$$Q_b = \sqrt{2}Q_n \left(\sqrt{p_{bn}}u(x_{vn}, \varepsilon_{2r}, L) + p_{bn}c_{sb} - \sqrt{1 - p_{bn}}u(-x_{vn}, \varepsilon_{2s}, L) - (1 - p_{bn})c_{bt} \right) \quad (2.64)$$

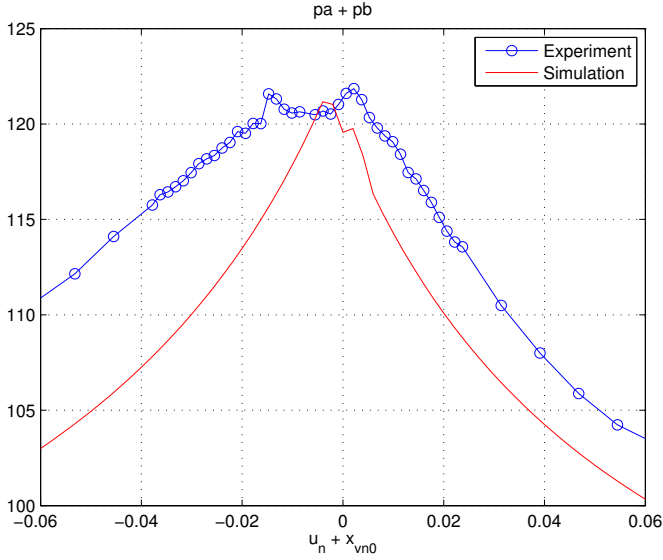


Figure 2.15: Sum of chamber pressures for different valve openings in steady-state when measured from experiment or simulated with modified model.

where c_{sa} , c_{at} , c_{sb} and c_{bt} are the laminar leakages coefficient from p_s to p_a from p_a to p_t , from p_s to p_b and from p_b to p_t respectively (see fig. 2.5). With the parameter values given in table 2.5 the sum of the pressures in the cylinder chambers is shown in fig. 2.15, when measured from experiment or simulated from the model, in steady-state for valve openings varying from -6% to 6% of the maximum opening. With these values used in the simulation the sum of the pressures is no longer constant equal to supply pressure but fits more closely to the experimental data. However, an error up to 7 bars remains due to the uncertainties inherent of leakage flow relations.

Table 2.5: Parameter estimation

Parameter	Value	Confidence Interval (CI)
ϵ_{1s} [-]	0	± 0.005
ϵ_{1r} [-]	0.003	± 0.005
ϵ_{2s} [-]	0.005	± 0.005
ϵ_{2r} [-]	0.003	± 0.005
c_{sa} [l/min]	0.035	± 0.05
c_{at} [l/min]	0.01	± 0.05
c_{sb} [l/min]	0.035	± 0.05
c_{bt} [l/min]	0.01	± 0.05

2.3.1.2 Estimation of static friction parameters

In order to estimate the static friction model parameters used in eq. (2.33), the friction force when zero load is applied to the system, can be calculated from measurements with the help of eq. (2.8). Combining the two equations, the following relation holds in steady-state:

$$F_h p_{Ln} = \left(F_c + (F_s - F_c) e^{-|v|/v_s} \right) \text{sign}(v) + \sigma_2 v$$

$$= \left[(1 - e^{-|v|/v_s}) \text{sign}(v), \quad e^{-|v|/v_s} \text{sign}(v), \quad v \right] \begin{bmatrix} F_c \\ F_s \\ \sigma_2 \end{bmatrix} \quad (2.65)$$

Or if $p_a + p_b$ is not constant:

$$F_h p_{Ln} = \begin{bmatrix} (1 - e^{-|v|/v_s}) \text{sign}(v), \\ (p_{an} + p_{bn}) (1 - e^{-|v|/v_s}) \text{sign}(v), \\ e^{-|v|/v_s} \text{sign}(v), \\ v \end{bmatrix}^T \begin{bmatrix} F_{pr} \\ f_{cfr} \\ F_s \\ \sigma_2 \end{bmatrix} \quad (2.66)$$

With the experimental data registered in steady-state for n different constant inputs, using linear least square method gives a good estimate for F_c , F_{pr} , f_{cfr} , F_s and σ_2 when v_s and n_s are known and when the data set is split in two, one set for positive velocities and one for negative velocities. For temperature $T = 30^\circ C$ and supply pressure $p_s = 80$ bar, these values are given in tables 2.1 and 2.6. Fig. 2.16 shows the friction forces for 115 different velocities in steady-state from both the experimental data and from the model with estimated parameters.

Repeating the same experiments at different temperatures, the dependence of parameters F_c , F_s and σ_2 with temperature is established and their variations are displayed in figs. 2.17. The results can be interpreted as follows: an increase of temperature causes the Coulomb and Stribeck frictions to increase and the viscous friction to decrease whereas the Stribeck velocity v_s tends to converge toward a constant value equal to 0.007 m/s.

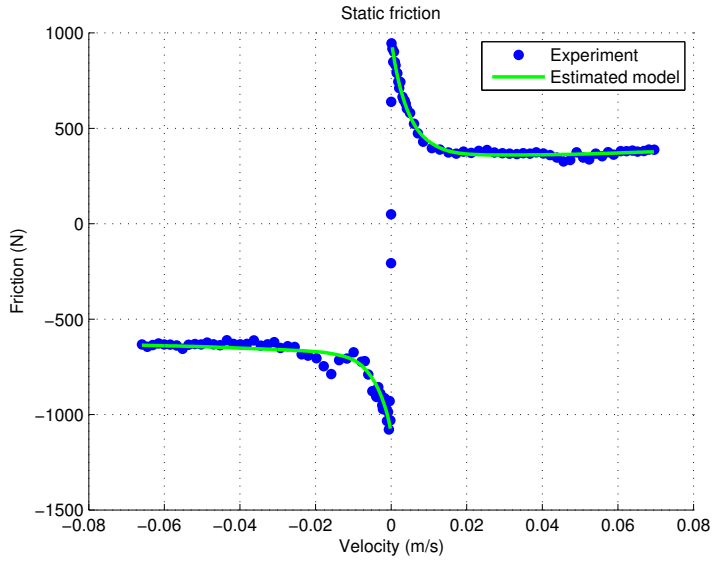


Figure 2.16: Friction estimation.

Table 2.6: Friction parameter estimation

Parameter	Value	Confidence Interval (CI)
Positive velocities		
σ_2 [Ns/m]	500	± 500
v_s [m/s]	0.008	± 0.001
F_c [N]	750	± 50
F_s [N]	1250	± 50
F_{pr} [N]	8	$+50 / - 8$
f_{cfr} [N]	570	± 50
Negative velocities		
σ_2 [Ns/m]	0	$+300 / - 0$
v_s [m/s]	0.006	± 0.001
F_c [N]	520	± 25
F_s [N]	1050	± 50
F_{pr} [N]	365	± 50
f_{cfr} [N]	135	± 50

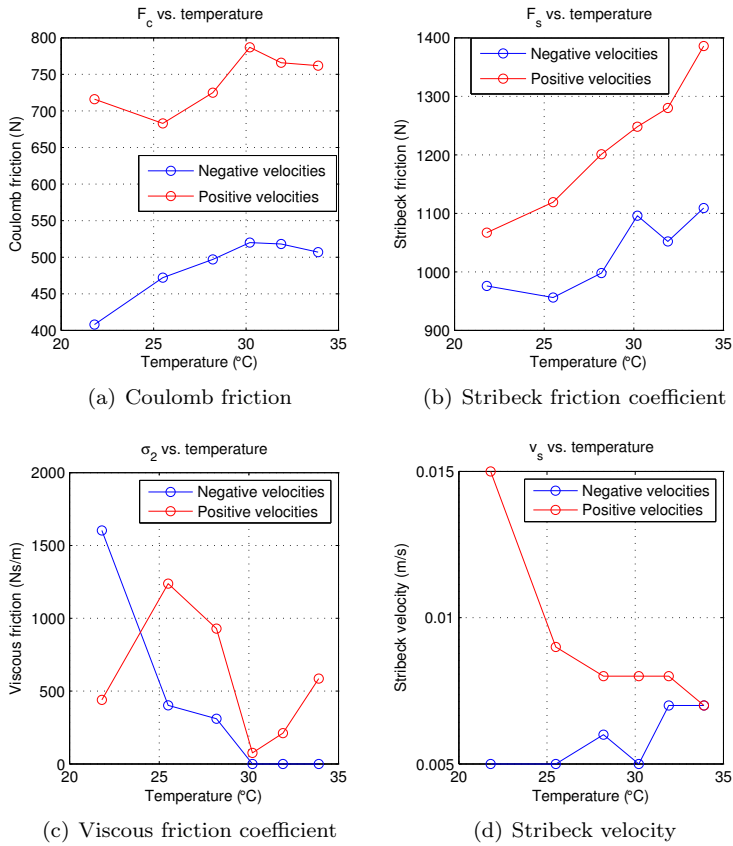


Figure 2.17: Variation of estimated static friction parameters with temperature.

2.3.1.3 Spool friction and dithering

The most severe nonlinearities in control valves are the stiction of the valve spool displacement in the sleeve and hysteresis (different flow rates even at the same valve opening depending on the moving direction of the valve spool). Ignoring their effect in the control loop can lead to stick-slip motion and oscillations which would degrade the performances of the controller. In order to compensate for stiction, a high-frequency zero-mean periodic signal (dither) can be added to the control signal. The amplitude of the dither should be so high that the stiction is overcome and the frequency should be higher than the operating frequency range of the system. In order to demonstrate the importance of dither, an experiment was made where the input signal to the valve takes different constant values, in one case with dither (frequency 400 Hz, amplitude 2% of nominal current) and in the other case without. Values for the flow versus variable $x = x_v \sqrt{p_s - \text{sign}(x_v)p_L}$ in steady-state (constant velocity and load pressure) is plotted in fig. 2.18. According to eq. (2.15) the relation is affine. From fig. 2.18 it can be seen that dithering compensates for stiction in the valve and removes hysteresis.

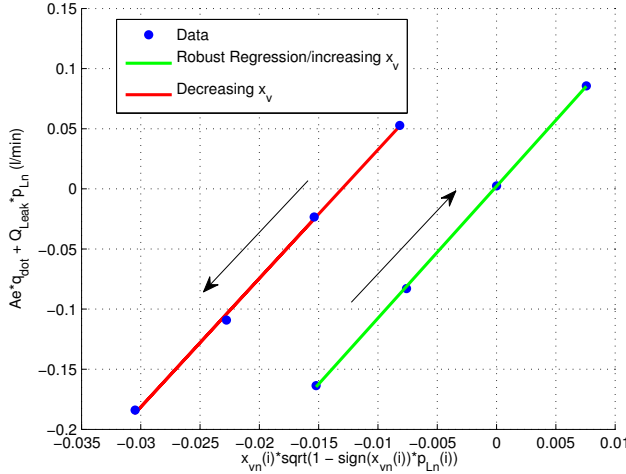
2.3.2 Dynamic Parameter Estimation

Once the static parameters are estimated, the next step in the system identification approach is to estimate the dynamic parameters comparing the experimental data generated with time varying input signal and the simulated data generated from the model developed in the previous section.

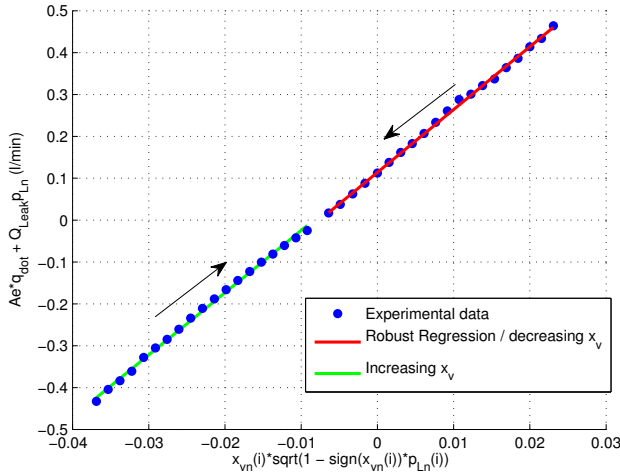
2.3.2.1 Valve dynamics

A first approach to estimate the parameters of the valve dynamics is to generate a step response of the EHSS shown in fig. 2.8 in closed loop with a PI controller and compare the results with two simulated models: a) with proportional valve characteristics and b) a second order valve dynamics model (eq. (2.32)). The results are shown in figs. 2.19 and 2.20. Fig. 2.19 shows the entire step response and the reverse step response, while fig. 2.20 is zoomed in at the transient response where the errors are the largest.

Besides estimating parameters to fit the experimental data closely, this experiment is used to assess the performance improvement using a second order model over a proportional model for the valve dynamics. Table 2.7 shows that the



(a) Without dither



(b) With dither

Figure 2.18: Importance of dither to remove hysteresis (stiction) in the valve

second order model represents a significant improvement compared to the proportional model. The step response (position) is improved by 52% and by 73%, respectively, for the RMS and MAX values. Table 2.7 also shows the RMS and MAX values for the measured load pressure p_L vs. the simulated load pres-

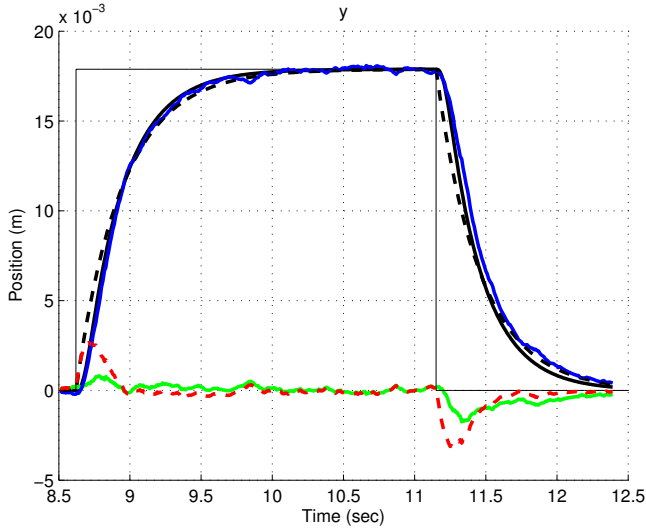


Figure 2.19: Experimental and simulated results with two different valve models. Blue: measurements, Black: second order model, Green: error second order model, Dashed: proportional model, Red: error proportional model.

sures. The pressure RMS values for the proportional and second order model are similar, while the MAX value shows a significant improvement for the second order model. Hence, the effects of the valve dynamics are important to consider in high-performance control of EHSS. Another approach consists in tuning the valve parameters for the model to fit the frequency response of the system and is done later in this section. The estimated values for the natural frequency ω_v , damping ratio ζ_v and valve gain K_v are given in table 2.8.

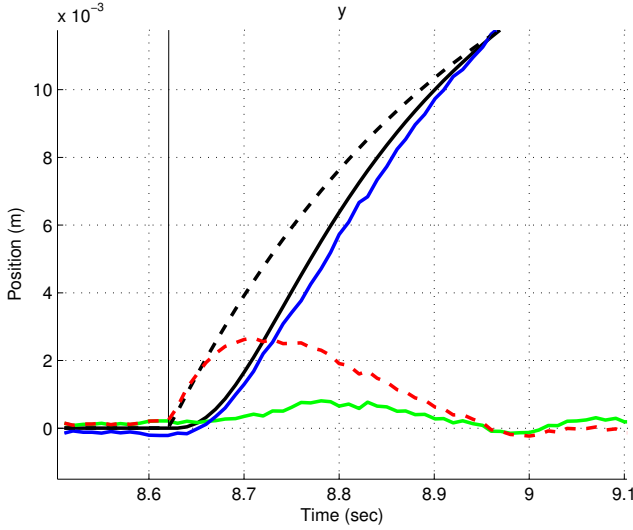


Figure 2.20: Transient response. Blue: measurements, Black: second order model, Green: error second order model, Dashed: proportional model, Red: error proportional model.

Position	Proportional	2 nd order	Improvement
RMS	$7.16 \cdot 10^{-4}$	$3.41 \cdot 10^{-4}$	52%
MAX	$9.19 \cdot 10^{-6}$	$2.46 \cdot 10^{-6}$	73%

Pressure	Proportional	2 nd order	Improvement
RMS	1.94	1.96	-1%
MAX	98.1	46.6	110%

Table 2.7: Comparison of RMS and MAX values against experiments for a step response using a proportional and a second order valve dynamics model. Top: Position, Bottom: Pressure.

Table 2.8: Valve dynamics parameter estimation

Parameter	Value	Confidence Interval (CI)
K_v [V ⁻¹]	0.16	± 0.01
ω_v [rad/s]	690	± 100
ζ_v	1	± 0.1
m_v	0.1	± 0.05
k_v	47800	+46000 / - 30000
d_v	138	+122 / - 85

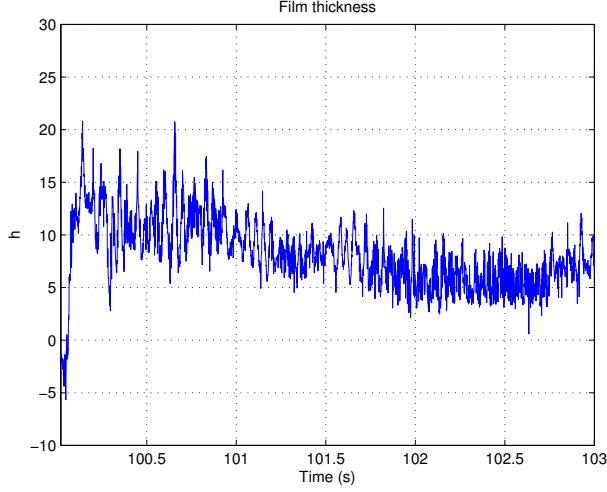


Figure 2.21: Film thickness variation under stepwise increase in velocity (from $v = 0\text{m/s}$ to $v = 0.02\text{m/s}$).

2.3.2.2 Friction dynamics

Parameters estimation Using the static friction parameters found previously, the same technique as in [43] is applied to estimate the time constant τ_h in case of acceleration or deceleration. From velocity and pressure measurements, the film thickness is calculated by making the assumption that z is constant immediately after a step change in velocity. For $\dot{z} = 0$, eqs. (2.34), (2.38) and (2.39) give the following relation:

$$F_{fric} = \text{sign}(v)g(v, h) + \sigma_2 v \quad (2.67)$$

$$\Rightarrow h = 1 - \frac{\text{sign}(v)(F_{fric} - \sigma_2 v) - F_c + F_c e^{-(|v|/v_s)^{n_s}}}{F_s e^{-(|v|/v_s)^{n_s}}} \quad (2.68)$$

Fig. 2.21 shows the variation of film thickness for a stepwise increase in velocity from $v = 0\text{m/s}$ to $v = 0.02\text{m/s}$. However the film thickness is greater than unity which is not in accordance with the model. The uncertainties in the model are too high for film thickness identification. Instead a default value of $\tau_h = 0.2\text{ s}$ is chosen. Fig. 2.22 shows the variation of film thickness for a stepwise decrease in velocity from $v = 0.02\text{m/s}$ to $v = 0.003\text{m/s}$. In this case by fitting the curve with eq. (2.37), τ_{hn} is found. See value in table 2.9.

Using the modified LuGre friction model, simulation is compared to experimental data in fig. 2.23 The film thickness becoming thinner during acceleration,

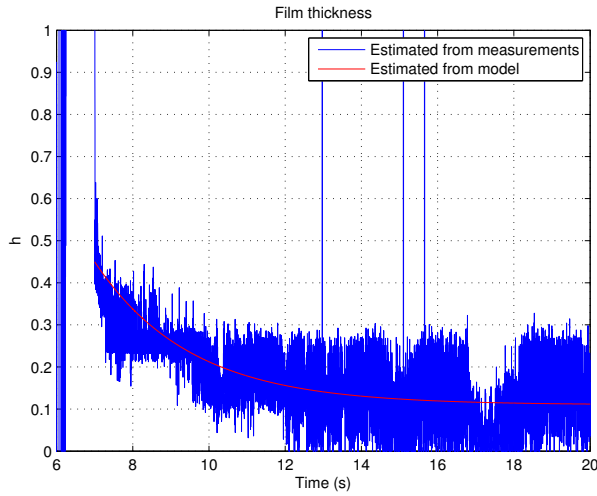


Figure 2.22: Film thickness variation under stepwise decrease in velocity (from $v = 0.02\text{m/s}$ to $v = 0.003\text{m/s}$).

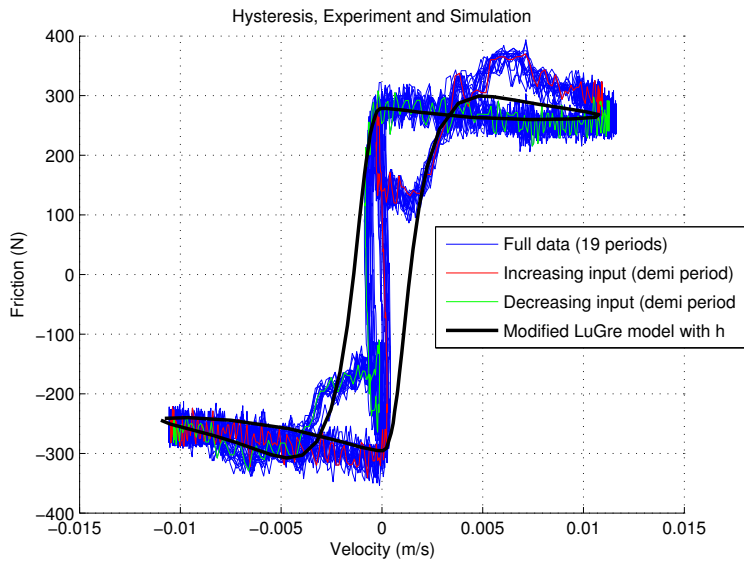


Figure 2.23: Comparison between experimental (blue, red, green) and simulated (black) data with modified LuGre friction model.

fig. 2.23 shows that friction is increased comparing to deceleration where the film thickness is larger.

Table 2.9: Parameter Estimation

Parameter	Value	Confidence Interval (CI)
σ_0 [N/m]	2.5×10^7	$+\infty / -0$
σ_1 [Ns/m]	108	$+\infty / -108$
v_b	0.04	± 0.02
Acceleration		
τ_h [s]	0.2	$+0.5 / -0.1$
Deceleration		
τ_h [s]	2.5	± 0.5

Valve spool stiction Despite of the presence of dithering in the valve, a more accurate model is obtained when considering a remaining stick-slip motion of the valve spool near zero valve opening. Flow forces and wear can be at the origin of this local position dependent force. Dynamics of the spool friction needs therefore to be added to the model replacing eq. (2.32) by:

$$m_v \ddot{x}_v = K_v k_v i - F_{stiction}(x_v, z_s) - k_v x_v - d_v \dot{x}_v \quad (2.69)$$

$$F_{stiction} = \sigma_{1v} \dot{z}_s \quad (2.70)$$

$$\dot{z}_s = x_v - \frac{|x_v|}{g_v(x_v)} z_s \quad (2.71)$$

$$g_v(x_v) = F_{st} e^{-(|x_v|/y_s)^{n_s}} \quad (2.72)$$

where i is the input current, m_v , k_v , d_v are the mass of the spool the stiffness of the torsion spring and the damping of the spool respectively. z_s is an internal state due to the stiction and can be viewed physically as the compression of the spool rubber seal. σ_{1v} is the damping when stiction and g_v , F_{st} , n_s and y_s are parameters relative to stiction. The new friction model including stiction in the valve at zero position is compared to experimental data in fig. 2.24. The behaviour at low mass velocity is now modeled. The cause of remaining error at low velocity between the experimental and simulated data could be the effect of the filter used to process the velocities measurements.

When looking at the velocity response in fig. 2.25, the simulations using LuGre and the modified LuGre including film thickness give similar results whereas a significant improvement is observed at low velocities when using in addition the model with stiction in the valve.

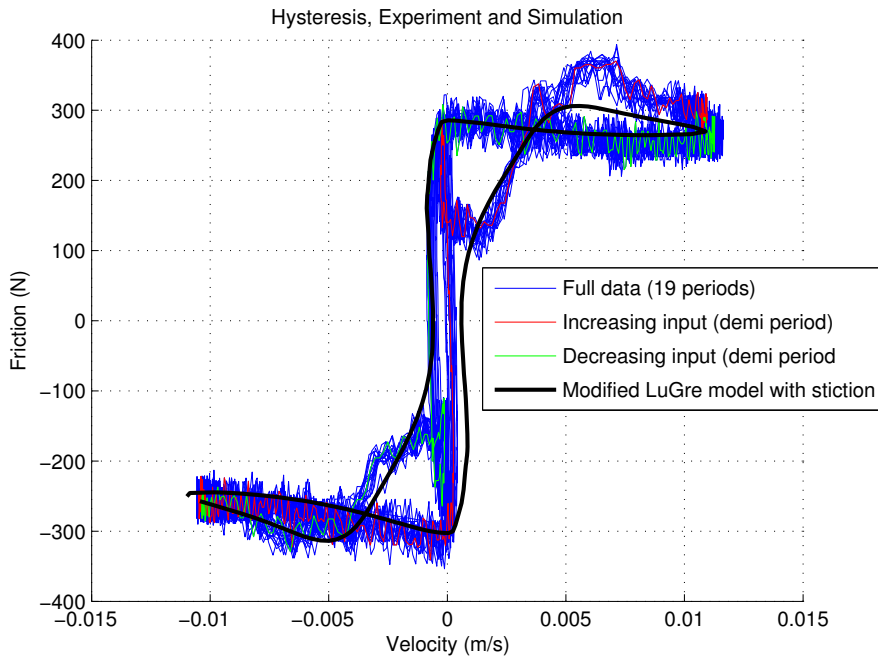


Figure 2.24: Comparison between experimental (blue, red, green) and simulated (black) data with modified LuGre friction model including stiction in the valve.

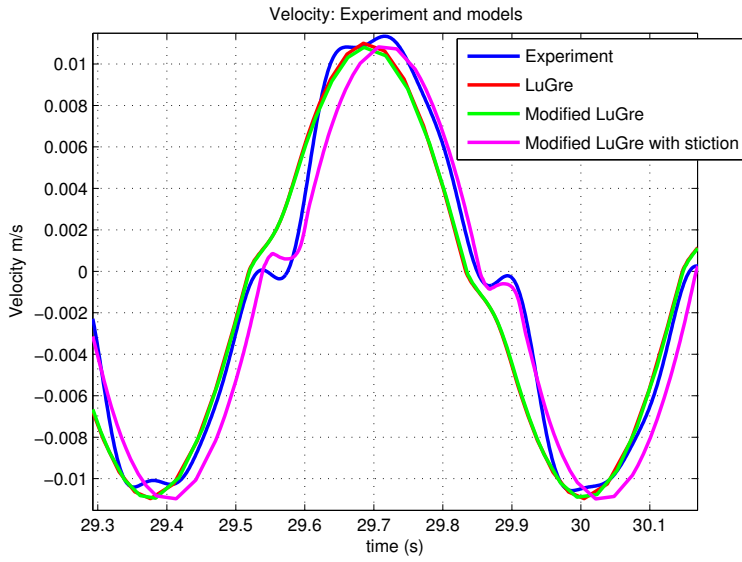


Figure 2.25: Comparison between experimental and simulated data with different friction models.

Table 2.10: Parameter Estimation

Parameter	Value	Confidence Interval (CI)
n_s	0.6	± 0.2
y_s [mm]	0.003	± 0.001
σ_{1v} [Ns/m]	8×10^3	$+\infty / -0$
F_{st} [N]	1.5×10^{-2}	$\pm 1 \times 10^{-2}$

2.3.3 Time Analysis

With the parameters estimated in the previous section the grey box model of the EHSS is simulated and its time response is compared with the experimental measurements. For both simulation and experiment the input signal to the valve is a sine wave of amplitude 1V and frequency 1 Hz. The results for position, velocity chamber pressures, load pressure and the sum of the chamber pressures are shown in figs. 2.26 to 2.31 during four seconds.

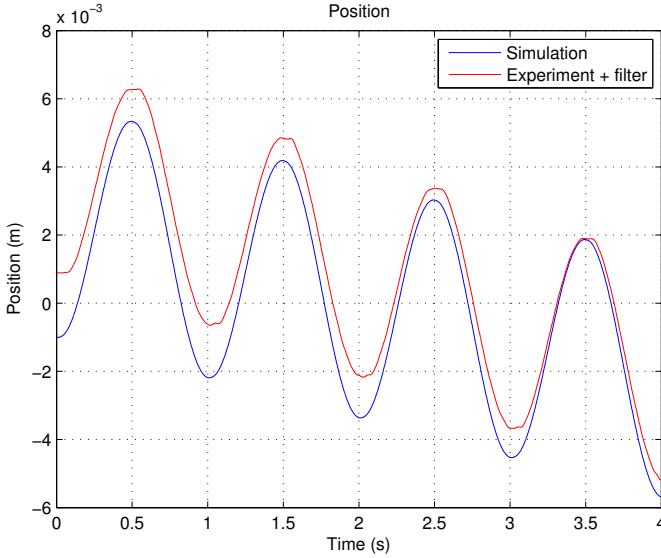


Figure 2.26: Position comparison between experimental measurement (blue) and simulation (red) for a sinusoidal input.

Comparing the amplitude and frequency of the output position in fig. 2.26, the model fits the test bed closely. However, the trend of the output position differs from simulation to experiment, which is caused by an uncertainty in the valve offset x_{vn0} estimated previously. A look at fig. 2.27 underlines two issues: first the velocity measurement needed to be filtered because it contains a high level of noise and second the simulated velocity differs slightly around zero velocity from experiment because the value for σ_0 needed to be decreased in order for the simulation to run. A too high σ_0 renders the system too stiff and makes the simulation extremely slow. The comparison of load pressure shows that the model is in accordance with the experiment, especially when looking at positive load pressure where the exponential decrease during the four periods is

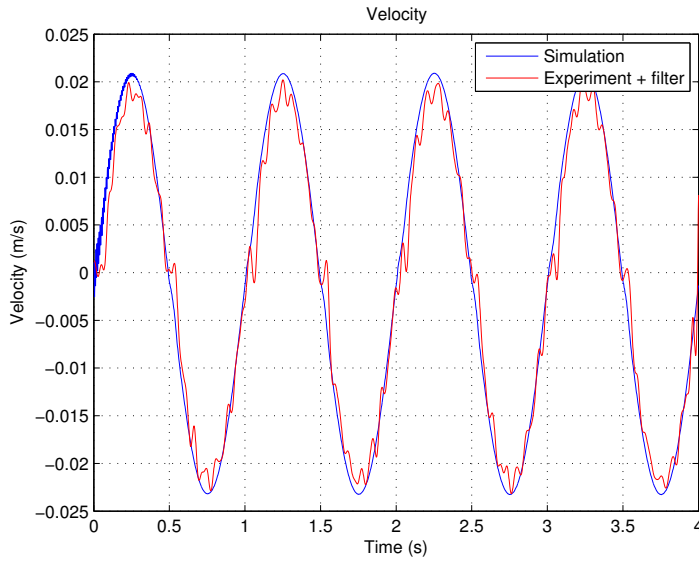


Figure 2.27: Velocity comparison between experimental measurement (blue) and simulation (red) for a sinusoidal input.

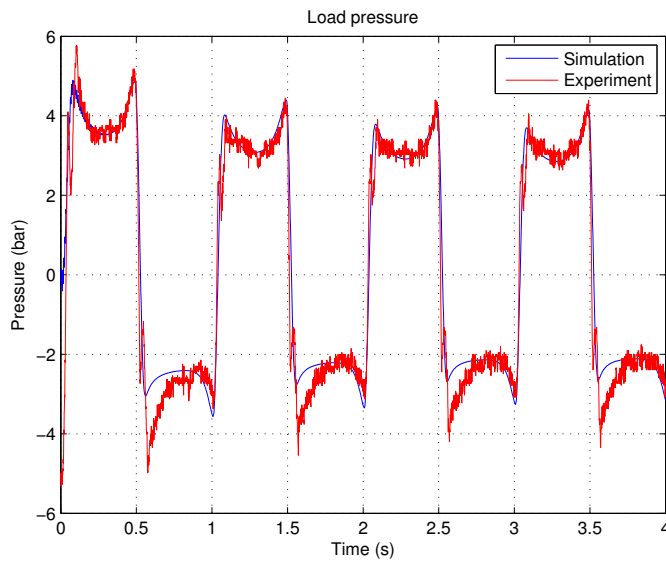


Figure 2.28: Comparison in load pressure between experimental measurement (blue) and simulation (red) for a sinusoidal input.

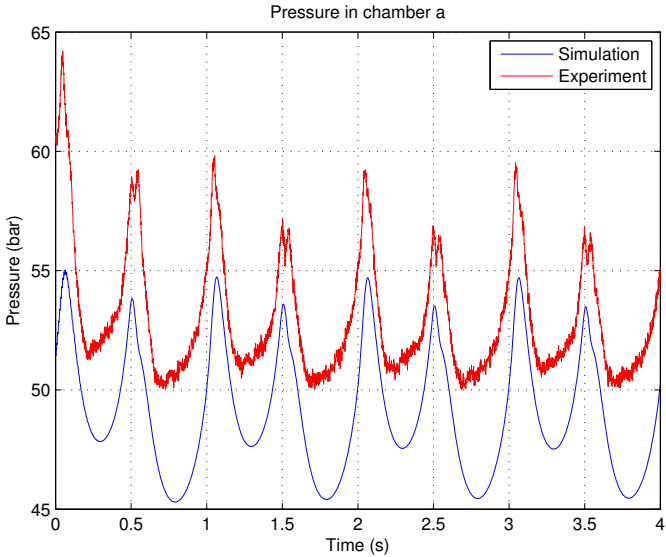


Figure 2.29: Comparison in chamber *a* pressure between experimental measurement (blue) and simulation (red) for a sinusoidal input.

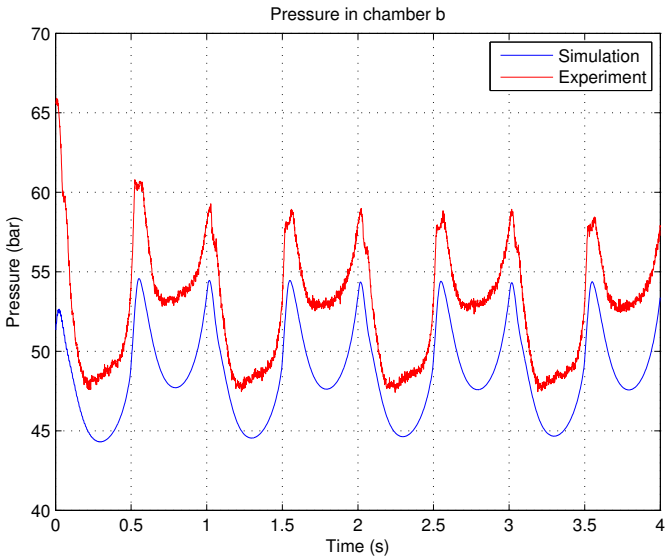


Figure 2.30: Comparison in chamber *b* pressure between experimental measurement (blue) and simulation (red) for a sinusoidal input.

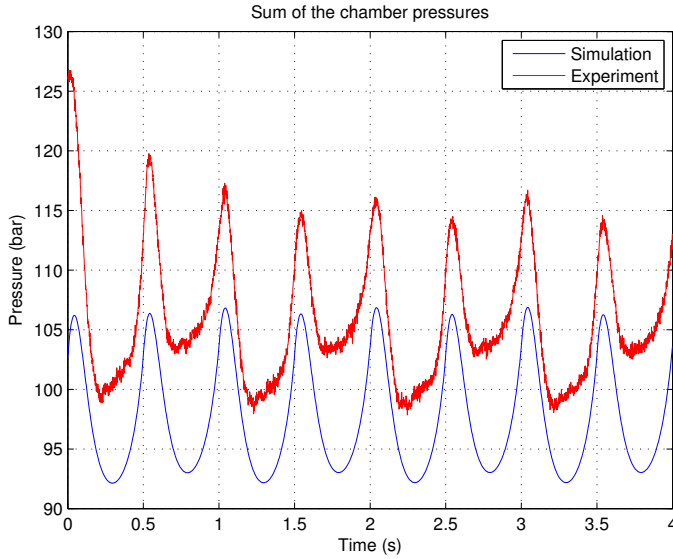


Figure 2.31: Comparison in the sum of chamber pressures between experimental measurement (blue) and simulation (red) for a sinusoidal input.

caused by the film formation inside the cylinder which reduces the friction force. Stribeck friction is also noticeable each time the velocity crosses zero. Finally, the last three figs. 2.29, 2.30 and 2.31 show that the chamber pressures, when considered independently, also are similar if generated from the simulation or from the experiment but with the exception of an offset of approximately 5 bars when looking at p_a or p_b and approximately 10 bars when looking at the sum of them. This offset is the result of uncertainties in the flows occurring inside the valve and the difficulty to estimate these parameters as shown previously in fig. 2.15.

2.3.4 Frequency Response

The knowledge of gain and phase shift of a linear system in open-loop at different frequencies is valuable in order to analyse the stability of this system with feedback control. However, when nonlinearities are present, the same tools as those used for linear systems are inappropriate since the response to a sine wave is not a pure sine wave and the frequency response is dependent of the amplitude of the excitation input. Nevertheless, in order to compare the simulation model with experiments and the linearised model with the high fidelity nonlinear one, in this section the frequency response of the EHSS behaviour is analysed, based on the parameters estimated in the previous section.

The frequency response from input u to position y of the linearised system in eqs. (2.41)-(2.45) is first investigated and its Bode plot is shown in fig. 4.1 together with the frequency response of the experimental test bed. The later frequency response from measurements is obtained by conducting the following experiment: first a stream of sine waves of amplitude 1V and with increasing frequency ranging from 1Hz to 100Hz is generated and used as the input signal to the servo valve while the measurements are recorded. Next the EHSS is approximated as quasi-linear: even if the response to each of the sine waves is not a pure sine wave, most of the energy in the output is indeed at the same frequency ω as the input. Calculating the fundamental of the output signal, the gain and phase shift can hence be observed for each sine wave constituting the stream. Finally the points are graphed on the Bode plot fig. 4.1.

Since the phase begins at -90° , the system contains an open-loop integrator. Two second order poles are placed at frequency $\omega_v = 110\text{Hz}$ for the valve dynamics and $\omega_{hyd} = 125\text{Hz}$ for the hydraulic natural frequency, with damping ratio equal to 0.8 and 0.13 respectively. Due to the sampling frequency and the sensor dynamics the frequency response for the experiment is limited to the range 1-100 Hz. It results from fig. 4.1 that with input amplitude of 1V the frequency response of the linear model is in accordance with the experiment.

2.3.4.1 Linear vs. nonlinear model

EHSS are highly nonlinear systems due mainly to turbulent orifice flow inside the servo valves, deadband and stiction inside the valve and friction inside the actuators. In order to distinguish and isolate the effects of these nonlinearities the linearised model is compared in frequency domain with the same model but with separately added nonlinearities for friction and orifice flow.

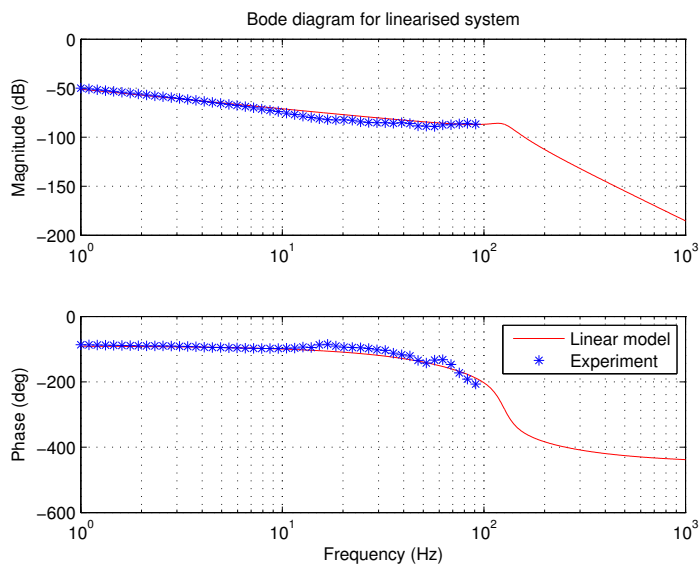


Figure 2.32: Frequency response from both experimental and simulated data issued from the linearised EHSS model. Input is the valve input signal, output is the mass position y .

Orifice flow nonlinearity Adding the nonlinearities due to the orifice flow in the valve and the deadbands, the new frequency response is shown in fig. 2.33 and 2.34 for different amplitudes of a sine stream, together with the linearised model (red line). The bode plot of the transfer functions from input to position is shown in fig. 2.33 whereas the transfer function from input to normalised load pressure is shown in fig. 2.34.

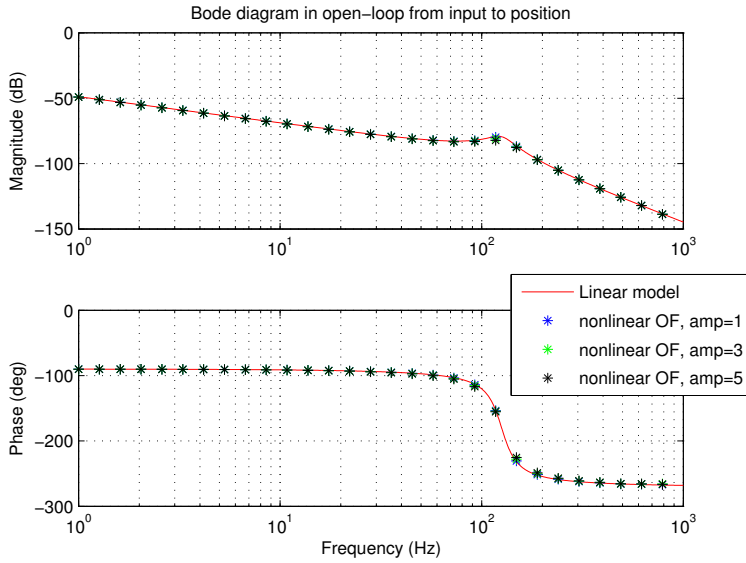


Figure 2.33: Input to position Bode diagram using a linearised model and the nonlinear model with different excitation amplitude: 5V, 3V and 1V.

The figures show that the nonlinearities due to the valve orifice flow have only a minor effect on the frequency response of the EHSS. The most important deviation is observed at resonance frequency for the transfer function from input to normalised load pressure at higher amplitudes (i.e. higher nonlinearities) where more damping is added to the system.

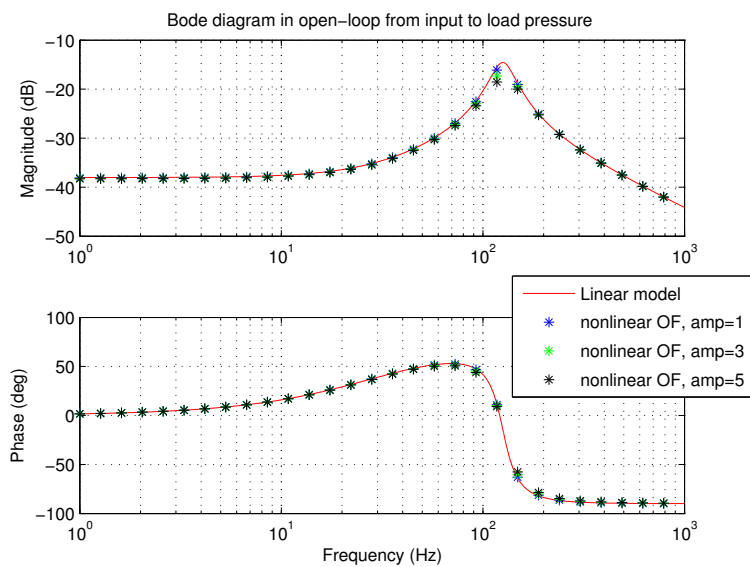


Figure 2.34: Input to pressure Bode diagram using a linearised model and the nonlinear model with different excitation amplitude: 5V, 3V and 1V.

Friction When adding the nonlinear friction model to the linear one, the frequency responses are shown in figs. 2.35 and 2.36 for transfer function from input to position and from input to nominal load pressure respectively, also with several amplitudes of the sine stream.

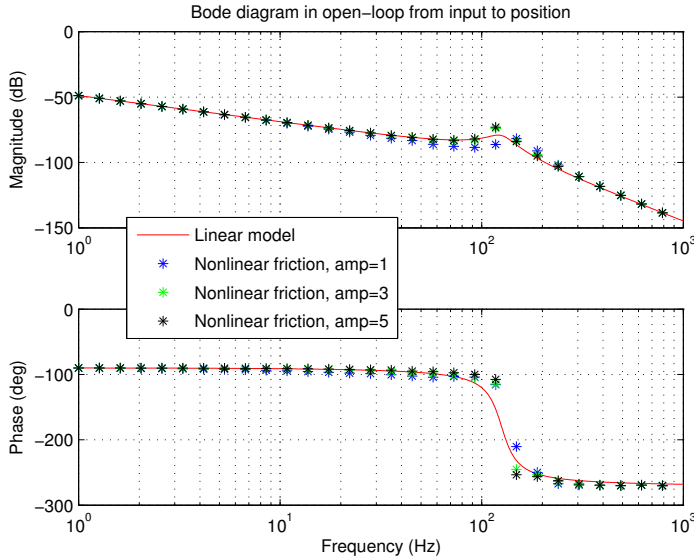


Figure 2.35: Input to position Bode diagram using a linearised model and the nonlinear model with different excitation amplitude: 5V, 3V and 1V.

These figures show that the nonlinearities inherent to the friction model have a more significant effect than those due to the orifice flow and deadband in the valve. This is true especially when the output is the load pressure, where for frequencies below the resonance frequency, the gain of the transfer function is lifted for small input amplitudes. It corresponds to the case when Stribeck friction has a dominant effect compared to viscous linear friction.

Complete EHSS The frequency response of the complete nonlinear model is now compared with the one obtained from the test bench and shown in figs. 2.37 and 2.38 when the output is the position and the normalised load pressure respectively.

A relative small difference at frequencies ranging from 10 to 50Hz can be observed when the output is position. This discrepancy can be caused by the too

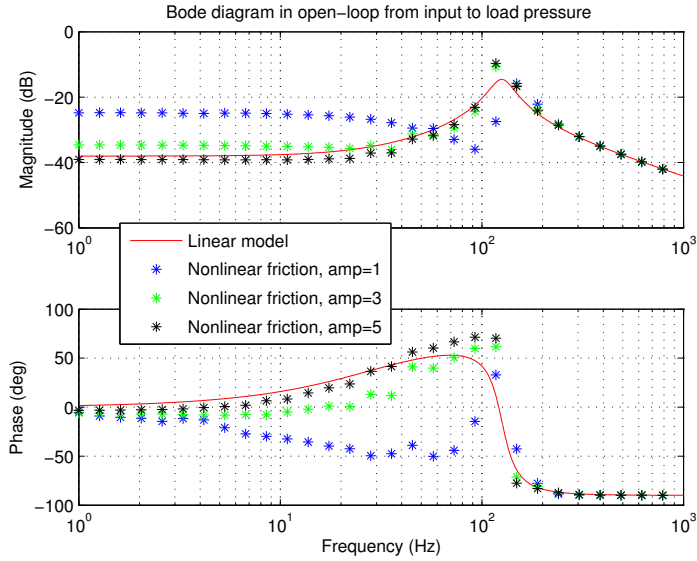


Figure 2.36: Input to pressure Bode diagram using a linearised model and the nonlinear model with different excitation amplitude: 5V, 3V and 1V.

low value of the stiffness σ_0 needed for the simulation to run. Looking at the Bode plot in fig. 2.38, it can be noticed that the nonlinear model is accurate enough to render the change of gains for different amplitudes of the excitations. However the model differs from the experiment at frequencies close to 100Hz, near the resonance frequency. Finally it can be concluded that the nonlinear friction model is better suited than the linearised model to describe the EHSS in the whole range of operating points and at a large range of frequencies.

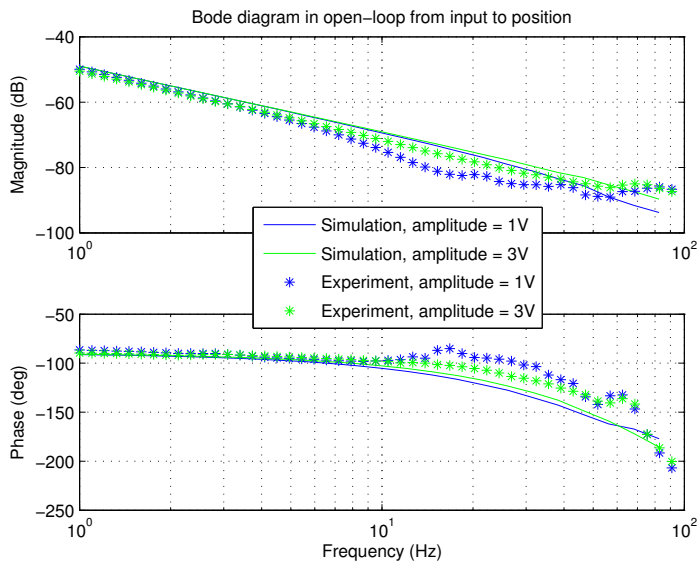


Figure 2.37: Bode diagram in open-loop from input to mass position y . Experimental data in blue and green stars for input amplitude 1V and 3V respectively and simulated data in corresponding coloured lines for input amplitude 1V and 3V.

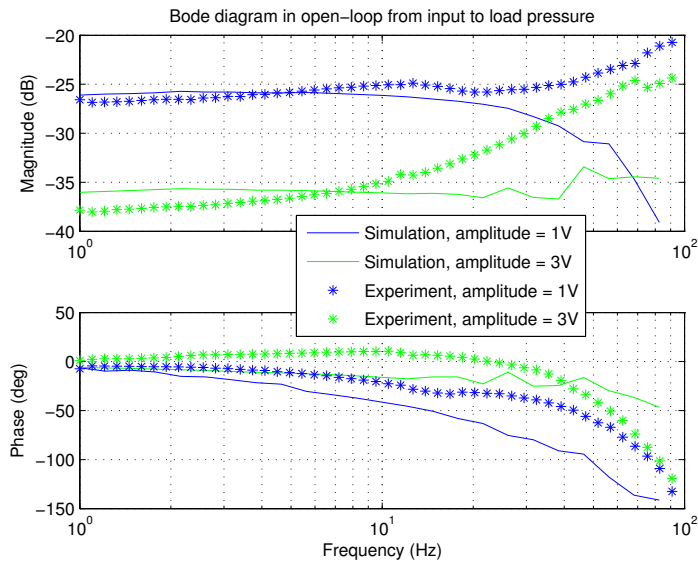


Figure 2.38: Bode diagram in open-loop from input to normalised load pressure pLn . Experimental data in blue and green stars for input amplitude 1V and 3V respectively and simulated data in corresponding coloured lines for input amplitude 1V and 3V.

2.4 State Space Model

In order to design a fault-tolerant controller for EHSS in later chapters, the model presented in this chapter will be used in the state space form which can be written as follows:

$$\begin{aligned}\dot{\mathbf{z}}(t) &= f(\mathbf{z}(t), u(t)) \\ \dot{\mathbf{y}}(t) &= h(\mathbf{z}(t), u(t))\end{aligned}$$

representing the state and output equations, where \mathbf{z} is the vector of states, u is the input and \mathbf{y} is the vector of outputs. The two multivariable functions f and h are not in the general case a linear combination of states and input.

Regrouping eqs. (2.9), (2.10), (2.16), (2.27), (2.34), (2.38), (2.36), (2.37), (2.39), (2.69), (2.70) and (2.71) the EHSS written in state space form is:

$$\dot{y} = v \quad (2.73)$$

$$\dot{v} = \frac{-k}{M}y + \frac{-(d + \sigma_1 + \sigma_2)}{M}v + \frac{F_h}{M}p_{Ln} + \frac{\sigma_0}{M} \left(\sigma_1 \frac{|v|}{g(v, h)} - 1 \right) z \quad (2.74)$$

$$\dot{z} = v - \sigma_0 \frac{|v|}{g(v, h)} z \quad (2.75)$$

$$\dot{h} = \frac{1}{\tau_h} (h_{ss}(v) - h) \quad (2.76)$$

$$\dot{p}_{Ln} = \frac{-\beta_e A_e}{p_s} v - \beta_e c_L p_{Ln} + \frac{\beta_e Q_n}{p_s} \sqrt{1 - \text{sign}(x_{vn}) p_{Ln}} \text{sat} \left(x_{vn}, \frac{L}{x_{v\max}} \right) \quad (2.77)$$

$$\dot{x}_{vn} = v_{vn} \quad (2.78)$$

$$\dot{v}_{vn} = \frac{-(\sigma_{1v} + k_v)}{m_v} x_{vn} + \frac{-\sigma_{2v}}{m_v} v_{vn} + \frac{\sigma_{1v}}{m_v} \frac{|x_{vn} x_{v\max}|}{g_v(x_{vn} x_{v\max})} z_s + K_v \frac{k_v}{m_v} i \quad (2.79)$$

$$\dot{z}_s = x_{vn} - \frac{|x_{vn} x_{v\max}|}{g_v(x_{vn} x_{v\max})} z_s \quad (2.80)$$

or in a more concise way:

$$\dot{z}_1 = a_{12}z_2 \quad (2.81)$$

$$\dot{z}_2 = a_{21}z_1 + a_{22}z_2 + a_{23} \left(\sigma_1 \frac{|v|}{g(v, z_4)} - 1 \right) z_3 + a_{25}z_5 \quad (2.82)$$

$$\dot{z}_3 = a_{32}z_2 + a_{33} \frac{|z_2|}{g(z_2, z_4)} z_3 \quad (2.83)$$

$$\dot{z}_4 = a_{42}h_{ss}(z_2) + a_{44}z_4 \quad (2.84)$$

$$\dot{z}_5 = a_{52}z_2 + a_{55}z_5 + a_{56} \sqrt{1 - \text{sign}(z_6)} z_5 \text{sat} \left(z_6, \frac{L}{x_{v\max}} \right) \quad (2.85)$$

$$\dot{z}_6 = a_{67}z_7 \quad (2.86)$$

$$\dot{z}_7 = a_{76}z_6 + a_{77}z_7 + a_{78} \frac{|x_{v\max} z_6|}{g_v(x_{v\max} z_6)} z_8 + b_7 u \quad (2.87)$$

$$\dot{z}_8 = a_{86}z_6 + a_{88} \frac{|x_{v\max} z_6|}{g_v(x_{v\max} z_6)} z_8 \quad (2.88)$$

where the coefficients a_{ij} are defined as follows:

$$a_{12} = 1$$

$$a_{21} = \frac{-k}{M}$$

$$a_{22} = \frac{-(d + \sigma_1 + \sigma_2)}{M}$$

$$a_{23} = \frac{\sigma_0}{M}$$

$$a_{25} = \frac{F_h}{M}$$

$$a_{32} = 1$$

$$a_{33} = -\sigma_0$$

$$a_{42} = \frac{1}{\tau_h}$$

$$a_{44} = -\frac{1}{\tau_h}$$

$$a_{52} = \frac{-\beta_e A_e}{p_s}$$

$$a_{55} = -\beta_e c_L$$

$$a_{56} = \frac{\beta_e Q_n}{p_s}$$

$$a_{67} = 1$$

$$a_{76} = \frac{-(\sigma_{1v} + k_v)}{m_v}$$

$$a_{77} = \frac{-\sigma_{2v}}{m_v}$$

$$a_{78} = \frac{\sigma_{1v}}{m_v}$$

$$b_7 = K_v \frac{k_v}{m_v}$$

$$a_{86} = 1$$

$$a_{88} = -1$$

and where the states and input in eqs. (2.81-2.88) are:

$$z_1 = y$$

$$z_2 = v$$

$$z_3 = z$$

$$z_4 = h$$

$$z_5 = p_{Ln}$$

$$z_6 = x_{vn}$$

$$z_7 = v_{vn}$$

$$z_8 = z_s$$

$$u = i$$

2.5 Summary, Discussion and Conclusions

In this chapter a high fidelity model of a typical electro hydraulic servo system has been developed and its behaviour was shown to be close to the physical behaviour of the corresponding test bed. By the mean of modelling, a better understanding and a good insight of the system was gained while describing the relationships between the variables and parameters. The governing equations were first established in section 2.2 for each component and second, in section 2.3, the system parameters were estimated using system identification with physical test bed measurements, leading to a so called grey box model of the EHSS. In order for the simulated results to best fit with the experimental data, the model structure has in a second step been specialised and the effects of nonlinearities in the valve and in the friction were analysed both in steady-state and in transient state. Finally, the model was linearised around zero load pressure and small valve opening. The effect of nonlinearities in the valve and the friction model were analysed separately resulting in the conclusion that the nonlinearities in friction is the main cause of divergence between the linear model and experiment for large range of frequencies and input amplitudes. The frequency response of the physical system approximated as quasi-linear underlines the role of nonlinear model to best describe the EHSS behaviour.

The main contributions in this chapter were first the development of a new friction model including the film formation inside the hydraulic actuator and its dynamics and the dependence of the friction model with the sum of the chamber pressures which is not assumed constant but varies up to +50% of the supply pressure, second the analysis and estimation of the flows around the spool of the servo valve whose effects are significant around zero spool position. In addition to the flows, the deadbands for a non-symmetric servo valve were estimated and the effects of valve stiction around zero spool position were also added to the model.

However, no matter how detailed the model is, simulations cannot reproduce the exact same data as experiment as for example in fig. 2.31 showing the sum of the chamber pressures for both the simulated and experimental data. The main reason could be the difficulties with tuning the model for all frequencies and all input sine wave amplitudes. The describing function of the model does not fit well with the one found with the help of experiment measurements for frequencies close to the resonance frequency (approximately 100Hz) as seen in fig. 2.38 for low amplitude. The dependency of certain parameters with temperature shown in figs. 2.10 and 2.17 also needs to be taken care of and supply pressure variation, complex behaviour of valve around zero spool position, the difficulty to estimate deadbands in the servo valve and complex behaviour of friction at low velocities contribute also for the inaccuracies of the model. Nevertheless,

the improvements in modelling highly nonlinear EHSS developed in this chapter together with the analysis of nonlinearities and their effects give a solid foundation for the design in the next chapters of adaptive fault-tolerant control for electro hydraulic servo systems.

CHAPTER 3

Fault Detection and Isolation

Hydraulic pistons are indispensable in industrial fields that require high actuation forces. The high difference of pressure needed inside the cylinder chambers in order to deliver the necessary force can be realised only if the leakage between the two chambers is kept small, involving considerable friction against the piston displacement. These two parameters, friction and leakage, play an important role in the reliability of hydraulic systems and their changes are a direct consequence of components' wear. According to the severity of leakage fault, the performances of the system are correspondingly degraded and a too high severity fault in leakage will eventually lead the system to failure. For instance in the offshore case where accessibility is an important factor to consider as it renders the cost for intervention especially high, fault detection for leakage should be considered in order to reduce the cost of maintenance and to prevent such systems from failures. However, due to significant non-linearities in hydraulic systems and the large uncertainties in their parameters, fault detection is difficult to implement in practice.

This chapter focuses on the investigation of leakage detection using model based methods in an experimental hydraulic test bed representing an actuator present in various EHSS. A crucial step in these methods is the ability to develop an accurate reference model of the system characterising its fault-free operation (see chapter 2).

The study of hydraulic leakage detection has received some attention in literature and numerous techniques have been developed in order to generate residuals, for example in [19] where the proposed methods are based on hardware redundancy, in [41], [30] where robust observer based methods are used for the nonlinear system models, in [31] using artificial neural network and in [2] where Extended Kalman Filter (EKF) is used to estimate the system states and detect both internal and external leakage. EKF is probably the most widely used nonlinear filter to determine the current mean and covariance of the states. However, EKF has certain well known drawbacks such as filter instability due to linearisation when sampling time is not small enough. In [38] the Unscented Kalman Filter (UKF) is used for fault monitoring of a hydraulic system. This approach employs recursive estimator meaning that only the current measurement and estimated state from the previous time step are required to compute the estimate for the current state. The significant characteristic of the UKF is that it is suitable for highly nonlinear systems as opposed to other approaches such as EKF. Once the residual signal is generated, the fault detector must analyse and process the signal to decide on the presence of a fault.

This chapter focusses on the design of residual generator for an Electric Hydraulic Servo System (EHSS) and on the analysis of the residuals using statistical change detection algorithms [4], [24], [18]. A crucial step in these methods is the ability to develop an accurate reference model of the system characterising its fault-free operation (see chapter 2). This system is representative for a typical nonlinear EHSS used in a commercial offshore drilling equipment. The system is used for drilling pipe handling and for operations such as making up a string of drilling pipe. Leakage or increased friction in an actuator could lead to pipe damage or to hazards in operation, so both are essential to diagnose. Residual generation is investigated for this highly nonlinear and parameter-uncertain system, and residuals are determined from which the too high severity faults could be diagnosed. Statistical change detection methods are employed for hypothesis testing about faults and the performance of different filters and the effectiveness of the proposed methods is examined in a Matlab/Simulink real-time environment. Results are validated against a test bed similar to the one described in chapter 2 but where two leakage bypasses are added to generate two different physical faults: internal and external leakage.

Four sections constitute the chapter, the first two focus on the theoretical design of a fault detector whereas the two others validate the design using experimental implementation. A fault detector consists of two main parts which are a residuals generator and a decision system as shown in fig. 3.1, where u is the plant input, y is the plant output, r are the residual signals, f are the faults and d are disturbances. The system considered in the rest of the chapter is the one described in chapter 2.

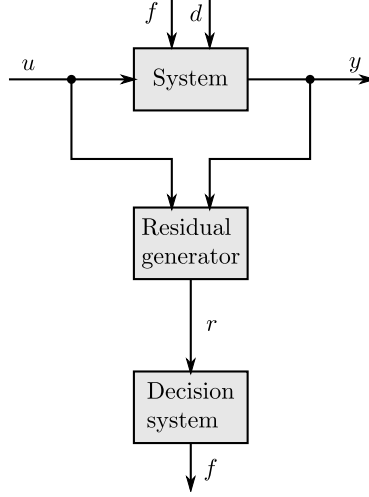


Figure 3.1: Diagnosis of systems

3.1 Residual Generator

The following constraints and measurements govern the EHSS:

$$c_1 : \quad Q_L = Q_n x_{vn} \sqrt{1 - \text{sign}(x_{vn}) p_{Ln}} \quad (3.1)$$

$$c_2 : \quad \dot{v} = \frac{1}{M} (A_e p_s p_{Ln} - ky - dv - F_{fric}(z, v)) \quad (3.2)$$

$$c_3 : \quad p_{Ln} \dot{=} \frac{4\beta}{V_t p_s} (Q_L - A_e v - Q_{Leak} p_{Ln}) \quad (3.3)$$

$$c_4 : \quad F_{fric} = \sigma_0 z + \sigma_1 \dot{z} + \sigma_2 v \quad (3.4)$$

$$c_5 : \quad \dot{z} = v - \frac{|v|}{g(v)} z \quad (3.5)$$

$$c_6 : \quad g(v) = \frac{F_c}{\sigma_0} + \frac{F_s - F_c}{\sigma_0} e^{-|v|/v_s} \quad (3.6)$$

$$m_1 : \quad y_1 = y + w_{1n} \quad (3.7)$$

$$m_2 : \quad y_2 = p_{Ln} p_s + w_{2n} \quad (3.8)$$

$$a_1 : \quad u_1 = x_{vn} x_{vmax} \quad (3.9)$$

$$d_1 : \quad v = \frac{dy}{dt} \quad (3.10)$$

$$d_2 : \quad \ddot{y} = \frac{dv}{dt} \quad (3.11)$$

$$d_3 : \quad p\dot{L}_n = \frac{dp_{Ln}}{dt} \quad (3.12)$$

$$d_4 : \quad \dot{z} = \frac{dz}{dt} \quad (3.13)$$

A formal analysis of analytic redundancy relations, which can be used for residual generation, is obtained from the constraints of the system, eqs.(3.1 - 3.13),

$$\mathcal{C} = \{c_1, c_2, c_3, c_4, c_5, c_6, m_1, m_2, a_1, d_1, d_2, d_3, d_4\} \quad (3.14)$$

The unknown variables in these constraints are

$$\mathcal{X} = \{Q_L, g, F_{fric}, z, \dot{z}, y, \dot{y}, \ddot{y}, p_{Ln}, \dot{p}_{Ln}, x_{vn}\} \quad (3.15)$$

and the known variables are

$$\mathcal{K} = \{y_1, y_2, u_1\} \quad (3.16)$$

A standard structural analysis [6] reveals that the maximum number of analytical redundancy relations are $|\mathcal{C}| - |\mathcal{X}| = 2$ where $|\cdot|$ denotes the number of elements in the set, also referred to as cardinality. A complete matching on \mathcal{C} is marked in the incidence matrix table 3.1 by *i using the simple ranking algorithm ([6]), where i is the rank number.

Table 3.1: Incidence matrix

Cstr.	Q_L	x_{vn}	F_{fric}	z	\dot{z}	y	v	\ddot{y}	p_{Ln}	\dot{p}_{Ln}	g	y_1	y_2	u_1
c_1	1^{*2}	1							1					
c_2			1^{*4}			1	1	1	1					
$c_3 = 0$	1						1		1	1				
c_4			1	1^{*5}	1		1							
$c_5 = 0$				1	1		1				1			
c_6							1				1^{*3}			
d_1						x	1^{*2}							
d_2							x	1^{*3}						
d_3									x	1^{*2}				
d_4			x	1^{*6}										
m_1						1^{*1}						1		
m_2									1^{*1}				1	
a_1		1^{*1}												1

Redundancy relations:

$$\begin{aligned}
 0 &= c_3(c_1(a_1, m_2), d_1(m_1), m_2, d_3(m_2)) \\
 0 &= c_5(c_4(c_2(m_1, d_1(m_1), d_2(d_1(m_1))), m_2), d_1(m_1)), d_4(c_4(\dots), d_1(m_1), c_6(d_1(m_1)))
 \end{aligned}$$

From the two redundancy relations found in table 3.1, the two residuals can be written in analytic form, only from using measurement and input:

$$r_1 = \frac{y_2^{(1)}}{p_s} - \frac{4\beta}{V_t p_s} \left(Q_n a_1 \sqrt{1 - \text{sign}(a_1) \frac{y_2}{p_s}} - A_e y_1^{(1)} - Q_{Leak} \frac{y_2}{p_s} \right) \quad (3.17)$$

$$r_2 = \frac{1}{\sigma_0} \left(-M y_1^{(3)} + A_e p_s \frac{y_2^{(1)}}{p_s} - k y_1^{(1)} - (d + \sigma_2) y_1^{(2)} \right) - y_1^{(1)} \\ + \frac{|y_1^{(1)}|}{F_c + (F_s - F_c) e^{-|y_1^{(1)}|/v_s}} \left(-M y_1^{(2)} + A_e p_s \frac{y_2}{p_s} - k y_1 - (d + \sigma_2) y_1^{(1)} \right) \quad (3.18)$$

The two resulting residual generators were found to be quite difficult to work with in practice due to large parameter variations and the complex nature of the LuGre model of friction. Instead, a simplified, steady-state model is considered.

3.1.1 Static

In steady-state, when the mass velocity \dot{y} is constant, eqs.(3.1-3.6) become s_1 to s_5 below,

$$s_1 : \quad F_{fric} = g(\dot{y}) \text{sign}(\dot{y}) + \sigma_2 \dot{y} \quad (3.19)$$

$$s_2 : \quad Q_L = Q_n x_{vn} \sqrt{1 - \text{sign}(x_{vn}) p_{Ln}} \quad (3.20)$$

$$s_3 : \quad 0 = A_e p_s p_{Ln} - k y - d v - F_{fric} \quad (3.21)$$

$$s_4 : \quad 0 = Q_L - A_e v - Q_{Leak} p_{Ln} \quad (3.22)$$

$$s_5 : \quad g(v) = \frac{F_c}{\sigma_0} + \frac{F_s - F_c}{\sigma_0} e^{-|v|/v_s} \quad (3.23)$$

$$m_1 : \quad y_1 = y + w_{1n} \quad (3.24)$$

$$m_2 : \quad y_2 = p_{Ln} p_s + w_{2n} \quad (3.25)$$

$$a_1 : \quad u_1 = x_{vn} x_{vmax} \quad (3.26)$$

$$d_1 : \quad v = \frac{dy}{dt} \quad (3.27)$$

In the set of steady-state equations, $\mathcal{C} = \{s_1, s_2, s_3, s_4, s_5, m_1, m_2, a_1, d_1\}$, $\mathcal{X} = \{Q_L, g, F_{fric}, y, \dot{y}, p_{Ln}, x_{vn}\}$ and $\mathcal{K} = \{y_1, y_2, u_1, \}$. Therefore there are a maximum of two residuals. This gives the possibility to detect and isolate the leakage and friction faults.

Two unmatched constraints, that can be used for residual generation, are eqs.(3.21) and (3.22).

Eq.(3.22) is sensitive to detect a leakage, but it is sensitive also to possible faults related to a_1 , a_2 , m_1 and m_2 . In a similar way eq.(3.21) can be used to detect a fault in friction, if the pressure and position measurements are available, but it is sensitive also to sensor faults in m_1 and m_2 . In the rest of the chapter only the leakage detection is considered but the fault detection in friction can be designed using the same methods. Fault isolation is not directly obtainable through passive diagnosis, i.e. by just observing the residuals. Instead active fault diagnosis can be employed where perturbation signals on u_1 cause response signatures in y_1 , y_2 and the two residuals, which depend on the type of fault that is present, see [7], [28] and [35] and references therein.

3.1.1.1 Residual for leakage detection

During operation, for example when the force is high and velocity is zero, valve opening x_v is positive and the load pressure is high. Eq.(3.22) gives in this case the following residual r :

$$0 = Q_L - Q_{Leak} p_{Ln} \quad (3.28)$$

$$r = Q_n x_{vn} \sqrt{1 - \frac{y_2}{p_s}} - Q_{Leak} \frac{y_2}{p_s}$$

$$r = Q_n x_{vn} \sqrt{1 - p_{Ln}} \sqrt{1 - \frac{w_{2n}}{p_s(1 - p_{Ln})}} - Q_{Leak} \left(p_{Ln} + \frac{w_{2n}}{p_s} \right) \quad (3.29)$$

Considering $\frac{w_{2n}}{p_s(1 - p_{Ln})} \ll 1$ an Euler approximation gives:

$$r = Q_n x_{vn} \sqrt{1 - p_{Ln}} - Q_{Leak} p_{Ln} + w' \quad (3.30)$$

where

$$w' = - \left(Q_n \frac{x_{vn}}{2\sqrt{1 - p_{Ln}}} + Q_{Leak} \right) \frac{w_{2n}}{p_s} \quad (3.31)$$

From eq.(3.31) it follows that the noise w' in the residual is also white with Gaussian distribution, so called white Gaussian noise (WGN). This assumption will hold in the following sections when designing the fault detectors.

The goal of the leakage detector is to decide between two hypotheses. The null hypothesis (\mathcal{H}_0), when only noise w' is present in the residual, characterises an acceptable leakage, whereas the alternative hypothesis (\mathcal{H}_1), when a constant signal and noise is present in the residual characterises a too high leakage. The probability of false alarm (P_{FA}) is chosen by the designer.

3.1.2 Dynamic

In this section the whole system is considered not only in steady-state but in the general case when the states are varying and is described by eqs.(3.1-3.13). In this case the design of residual generators is based on both the standard Extended Kalman Filter and the State-Augmented Extended Kalman Filter (SAEKF) whose algorithms are presented in [8]. The SAEKF estimates the system states including augmented states (such as leakage) and generates residuals. The EKF linearises a nonlinear model around the current estimates and computes posteriori estimates with updated system measurements. Two leakage related faults such as external chamber leakage at either side of the actuator and internal leakage between the two hydraulic cylinder chambers are investigated. If internal flow occurs, it could lead to actuator performance reduction, since only a part of the liquid is available for actuation. When external leakage, the fluid loss in the system also leads to drop in the load pressure and performance reduction, which in turn can lead to severe system failure and operation stop after a period of time. In order to detect external leakage, both chamber pressures of the cylinder must be measured and the assumption of incompressible fluid in the flow equations must be relaxed. The test bed shown in fig. 2.2 must be modified in order to add internal or external leakage flow into the EHSS. The new test bed is shown in fig. 3.2 where two flow control valves are added, one between chamber A and B of the hydraulic cylinder (number 10 on the figure) and one between chamber A and the tank (number 11). The new drawing of the EHSS is shown in fig. 3.3.

Eqs.(3.1-3.13 are hence modified to the following constraints:

$$c_1 : \quad Q_a = Q_n \sqrt{2} \left(\sqrt{1 - p_{an}} k_{vp}(x_{vn}) - \sqrt{p_{an}} k_{vn}(x_{vn}) \right) \quad (3.32)$$

$$c_2 : \quad Q_b = Q_n \sqrt{2} \left(\sqrt{p_{bn}} k_{vn}(x_{vn}) - \sqrt{1 - p_{bn}} k_{vp}(x_{vn}) \right) \quad (3.33)$$

$$c_3 : \quad \dot{v} = \frac{1}{M} (A_e p_s p_{Ln} - F_{fric}(z, v) - F_{load}(y, v)) \quad (3.34)$$

$$c_4 : \quad \dot{p}_{an} = \frac{\beta}{(V_t/2 + A_e y) p_s} (Q_a - A_e v - Q_{Li}(p_{an} - p_{bn}) - Q_{Le} p_{an}) \quad (3.35)$$

$$c_5 : \quad \dot{p}_{bn} = \frac{\beta}{(V_t/2 - A_e y) p_s} (-Q_b + A_e v + Q_{Li}(p_{an} - p_{bn})) \quad (3.36)$$

$$c_6 : \quad F_{fric} = \sigma_0 z + \sigma_1 \dot{z} + \sigma_2 v \quad (3.37)$$

$$c_7 : \quad \dot{z} = v - \frac{|v|}{g(v)} z \quad (3.38)$$

$$c_8 : \quad g(v) = \frac{F_c}{\sigma_0} + \frac{F_s - F_c}{\sigma_0} e^{-|v|/v_s} \quad (3.39)$$

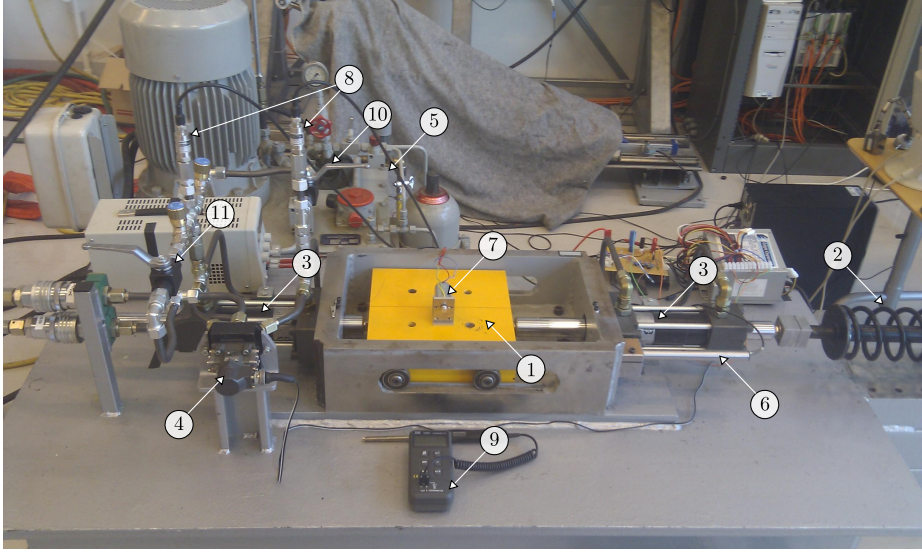


Figure 3.2: Test bench. 1: Mass, 2: Mechanical spring/damper, 3: Hydraulic cylinder, 4: Servo-valve, 5: Pressure source, 6: Position sensor (LVDT), 7: Velocity sensor (tachometer), 8: Pressure sensors, 9: Thermometer, 10: Internal leakage flow valve, 11: External leakage flow valve (only in chamber A)

$$c_9 : \quad \dot{v}_v = \frac{1}{m_v} \left(-k_v x_{v\max} x_{vn} - d_v v_v + \frac{k_v x_{v\max}}{u_{\max}} u \right) \quad (3.40)$$

$$m_1 : \quad y_1 = y + w_{1n} \quad (3.41)$$

$$m_2 : \quad y_2 = p_{an} p_s + w_{2n} \quad (3.42)$$

$$m_3 : \quad y_3 = p_{bn} p_s + w_{3n} \quad (3.43)$$

$$a_1 : \quad u_1 = x_{vn} x_{v\max} \quad (3.44)$$

$$d_1 : \quad v = \frac{dy}{dt} \quad (3.45)$$

$$d_2 : \quad \dot{v} = \frac{dv}{dt} \quad (3.46)$$

$$d_3 : \quad \dot{p}_{an} = \frac{dp_{an}}{dt} \quad (3.47)$$

$$d_4 : \quad \dot{p}_{bn} = \frac{dp_{bn}}{dt} \quad (3.48)$$

$$d_5 : \quad \dot{z} = \frac{dz}{dt} \quad (3.49)$$

$$d_6 : \quad v_v = x_{v\max} \frac{dx_{vn}}{dt} \quad (3.50)$$

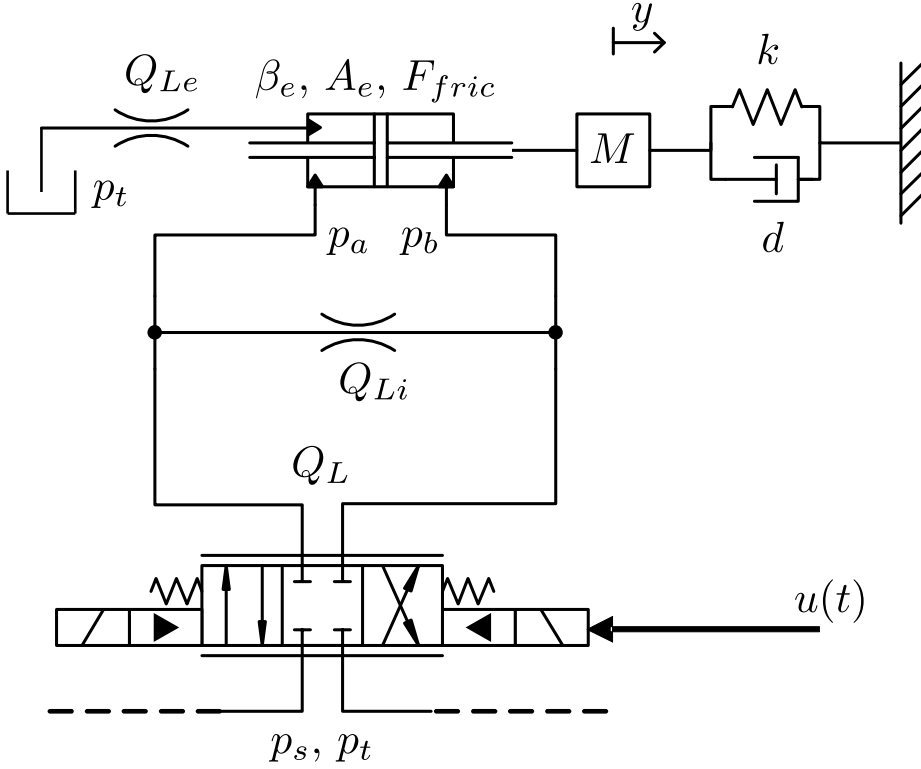


Figure 3.3: Electro Hydraulic Servo System with internal leakage in the cylinder and external leakage in cylinder chamber A .

$$d_7 : \quad \dot{v}_v = \frac{dv_v}{dt} \quad (3.51)$$

In this dissertation only an internal, external or both internal and external leakage fault is considered and no other fault occurs.

3.1.2.1 State-Augmented Extended Kalman Filter

The first method used to generate residuals is to estimate directly the internal and external leakage flows (Q_{Li} and Q_{Le} respectively) and to subtract from them the leakage flows when the system is in a fault-free working mode. The leakage flows are estimated by considering them as augmented states in the system and by running a State-Augmented Extended Kalman Filter whose algorithm is well described in [8]. This method is illustrated in fig. 3.4.

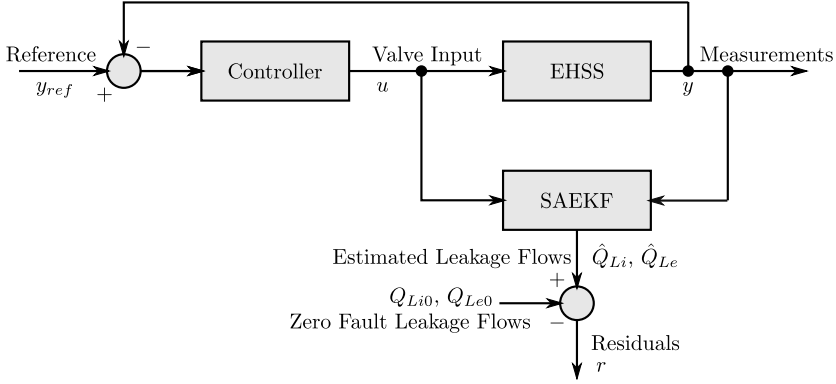


Figure 3.4: Leakage residual generator via SAEKF.

Defining $\mathbf{x} = (y, v, p_{an}, p_{bn}, z, x_{vn}, v_{vn})$ and $\mathbf{p} = (Q_{Li}, Q_{Le})$ a vector of unknown parameters and including \mathbf{p} into the states (so called augmented states), the EHSS can be written as:

$$\begin{aligned}
 \dot{\mathbf{x}} &= f(u, \mathbf{x}, \mathbf{p}) \\
 \dot{\mathbf{p}} &= 0 \\
 y &= h(u, \mathbf{x}, \mathbf{p})
 \end{aligned} \tag{3.52}$$

where f is the state update function and h is the measurement function. \mathbf{p} is constant during the propagation phase but its value is updated during the update phase (see the algorithm in [8] for details), which allows for the filter to estimate the flow parameters Q_{Li} and Q_{Le} as the system is running.

3.1.2.2 Extended Kalman Filter

While the SAEKF attempts to estimate the leakage flows directly, generating one residual for each leakage flow, another method based on different Extended Kalman Filters (without augmented states) can be used to generate residuals. The method consists in first partitioning the two-dimensional space formed by Q_{Li} and Q_{Le} and then generating a residual for each partition box using an EKF for which the Q_{Li} and Q_{Le} values are the ones in the centre of the box. Each EKF returns three residuals which are the errors between the estimated and measured states. For example, for the i^{th} EKF: $r_{i1} = |\hat{y} - y_1|$, $r_{i2} = |\hat{p}_a - y_2|$, $r_{i3} = |\hat{p}_b - y_3|$. The box for which the residuals take the lowest values furnishes the estimated values for Q_{Li} and Q_{Le} . The approach is illustrated in fig. 3.5. In order to validate the method and show that leakage fault can be detected, a rough partition of the leakage flow space is chosen but it can be further refined

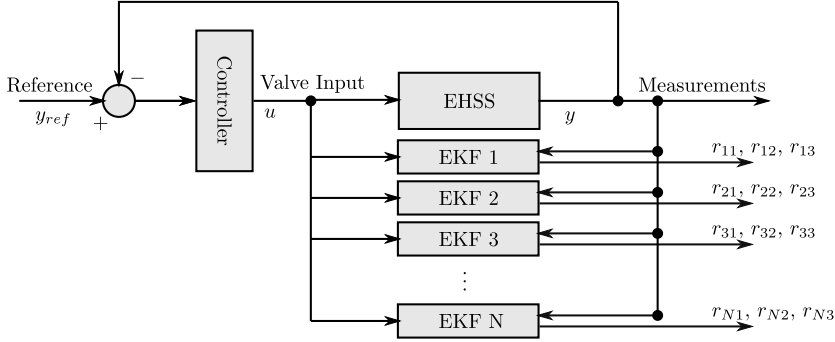


Figure 3.5: Leakage residual generator via different EKF. Each filter uses a different assumption about leakage flows.

if a more precise estimate is of interest. The first filter models a system with no leakage. The second filter models a system with only internal leakage equal to twenty percent of the nominal flow, while the third filter models a system with only external leakage equal to one percent of the nominal flow. Finally the fourth filter models a system with both the internal and external leakages. In practice, an internal leakage causes a change in chamber pressures which is about twenty times smaller than that caused by an external leakage of same flow.

The critical step in the design of the Kalman filters is the tuning of the elements of the covariance matrices \mathbf{Q} and \mathbf{R} , as they affect the performance, convergence and stability of the filters. The use of large values in \mathbf{Q} presumes high model noise and parameter uncertainties which increases the filter dynamics and decreases the steady-state performance. Matrix \mathbf{R} is related to the measurements noise and increasing the values of the elements of \mathbf{R} will assume that the current measurements are more affected by noise and thus less reliable. Consequently, the filter gain will decrease, yielding poorer transient response. From the test bed measurements, the standard deviations due to noise can be obtained and the resulting variances are added into the matrix \mathbf{R} . The matrix \mathbf{Q} was found through different simulations as described in [8]. The values of the elements of the diagonal matrices \mathbf{Q}_{pp} , \mathbf{Q}_{xx} (SAEKF) and \mathbf{Q} (EKF) are given below, where “diag” stands for diagonal matrix. The matrix \mathbf{R} consists of the variance of the measured noises.

$$\mathbf{Q}_{xx} = \text{diag}(10^{-4}, 10^{-3}, 10^{-4}, 10^{-4}, 10^{-2}, 10^{-2}, 10^{-2}) \quad (3.53)$$

$$\mathbf{Q}_{pp} = \text{diag}(10^{-4} \times (1.1, 2.3)) \quad (3.54)$$

$$\mathbf{Q} = \text{diag}(10^{-6} \times (1, 1, 10, 10, 100, 100, 100)) \quad (3.55)$$

$$\mathbf{R} = \text{diag}(10^{-8} \times (0.5521, 2.641, 11.98, 11.98)) \quad (3.56)$$

3.2 Hypothesis Testing and Decision System

3.2.1 Unknown DC levels and noise parameters

In a first step, the time n_0 (time when the fault occurs) is supposed to be known. This assumption will be relaxed in a second step. Since the leakage in the cylinder as well as the valve parameter Q_n is uncertain, the DC level of residual (3.30) before and after the jump time, respectively A_1 and A_2 are unknown. The variance of the WGN in the residual depends on the leakage in the cylinder as shown in eq.(3.31). It is hence considered as another unknown parameter. The hypothesis testing problem is

$$\begin{aligned} \mathcal{H}_0 : A_1 &= A_2 \\ \mathcal{H}_1 : A_1 &\neq A_2 \end{aligned}$$

Since this is a composite hypothesis test, the usual generalised likelihood ration test (GLRT) is applied, which for a signal with unknown parameter vector θ in WGN, is to decide \mathcal{H}_1 if the log-likelihood $L(x)$ exceeds a threshold γ ,

$$L(x) = \frac{p(x; \hat{\theta}, \mathcal{H}_1)}{p(x; \mathcal{H}_0)} > \gamma \quad (3.57)$$

where γ is determined by the desired false alarm probability P_{FA} and $\hat{\theta}$ is the maximum likelihood estimator (MLE) of θ (maximises $p(x; \theta, \mathcal{H}_1)$).

The probabilities for false-alarm P_{FA} and detection P_D are

$$P_{FA} = \int_{\{x: L(x) > \gamma\}} p(x; \mathcal{H}_0) dx \quad (3.58)$$

$$P_D = \int_{\{x: L(x) < \gamma\}} p(x; \mathcal{H}_1) dx. \quad (3.59)$$

The MLEs of the DC levels and the variances of the residual before and after the jump time under \mathcal{H}_0 (i.e. \hat{A} and $\hat{\sigma}_0^2$) and under \mathcal{H}_1 (i.e. \hat{A}_1 , \hat{A}_2 , $\hat{\sigma}_1^2$ and $\hat{\sigma}_2^2$)

respectively) are determined as follows [4], [24]:

$$\begin{aligned}
 \hat{A} &= \frac{1}{N} \sum_{n=0}^{N-1} x[n] = \bar{x} \\
 \hat{A}_1 &= \frac{1}{n_0} \sum_{n=0}^{n_0-1} x[n] \\
 \hat{A}_2 &= \frac{1}{N-n_0} \sum_{n=n_0}^{N-1} x[n] \\
 \hat{\sigma}_0^2 &= \frac{1}{N} \sum_{n=0}^{N-1} (x[n] - \hat{A})^2 \\
 \hat{\sigma}_1^2 &= \frac{1}{n_0} \sum_{n=0}^{n_0-1} (x[n] - \hat{A}_1)^2 \\
 \hat{\sigma}_2^2 &= \frac{1}{N-n_0} \sum_{n=n_0}^{N-1} (x[n] - \hat{A}_2)^2
 \end{aligned} \tag{3.60}$$

The GLRT decides \mathcal{H}_1 if

$$L_G(x) = \frac{p(x; \hat{A}_1, \hat{A}_2, \hat{\sigma}_1^2, \hat{\sigma}_2^2)}{p(x; \hat{A}, \hat{\sigma}_0^2)} > \gamma \tag{3.61}$$

Assuming Gaussian distributions, which will be verified experimentally in Section 3.3,

$$\begin{aligned}
 \frac{p(x; \hat{A}_1, \hat{A}_2, \hat{\sigma}_1^2, \hat{\sigma}_2^2)}{p(x; \hat{A}, \hat{\sigma}_0^2)} &= \\
 \prod_{n=0}^{n_0-1} \sqrt{\frac{\hat{\sigma}_0^2}{\hat{\sigma}_1^2}} \exp \left[\frac{1}{2} \left(\frac{(x[n] - \bar{x})^2}{\hat{\sigma}_0^2} - \frac{(x[n] - \hat{A}_1)^2}{\hat{\sigma}_1^2} \right) \right] &\times \\
 \prod_{n=n_0}^{N-1} \sqrt{\frac{\hat{\sigma}_0^2}{\hat{\sigma}_2^2}} \exp \left[\frac{1}{2} \left(\frac{(x[n] - \bar{x})^2}{\hat{\sigma}_0^2} - \frac{(x[n] - \hat{A}_2)^2}{\hat{\sigma}_2^2} \right) \right], &
 \end{aligned}$$

hence,

$$2 \ln L_G = \sum_{n=0}^{n_0-1} \left[\ln \left(\frac{\hat{\sigma}_0^2}{\hat{\sigma}_1^2} \right) + \frac{(x[n] - \bar{x})^2}{\hat{\sigma}_0^2} - \frac{(x[n] - \hat{A}_1)^2}{\hat{\sigma}_1^2} \right] + \sum_{n=n_0}^{N-1} \left[\ln \left(\frac{\hat{\sigma}_0^2}{\hat{\sigma}_2^2} \right) + \frac{(x[n] - \bar{x})^2}{\hat{\sigma}_0^2} - \frac{(x[n] - \hat{A}_2)^2}{\hat{\sigma}_2^2} \right]$$

and by using the estimates in eq. 3.60,

$$2 \ln L_G = N \ln(\hat{\sigma}_0^2) - n_0 \ln(\hat{\sigma}_1^2) - (N - n_0) \ln(\hat{\sigma}_2^2)$$

Since the logarithm is a monotonic function, the GLRT decides \mathcal{H}_1 if :

$$2 \ln L_G(x) = N \ln \left(\frac{\hat{\sigma}_0^2}{(\hat{\sigma}_1^2)^{\frac{n_0}{N}} (\hat{\sigma}_2^2)^{\frac{N-n_0}{N}}} \right) > \gamma' \quad (3.62)$$

where $\gamma' = 2 \ln \gamma$.

3.2.2 Unknown DC levels and noise parameters and jump time

To accommodate with unknown jump time, the transition, if it occurs, is assumed not too close to the endpoints of the observation interval. $n_{0_{min}} \leq n_0 \leq n_{0_{max}}$, where presumably $n_{0_{min}} \gg 1$ and $n_{0_{max}} \ll N - 1$

$$L_G(x) = \frac{p(x; \hat{n}_0, \hat{A}_1, \hat{A}_2, \hat{\sigma}_1^2, \hat{\sigma}_2^2)}{p(x; \hat{A}, \hat{\sigma}_0^2)} > \gamma \quad (3.63)$$

where \hat{n}_0 is the MLE under \mathcal{H}_1 . Or equivalently,

$$L_G(x) = \frac{\max_{n_0} p(x; n_0, \mathcal{H}_1)}{p(x; \mathcal{H}_0)} \quad (3.64)$$

Since the probability density function (PDF) under \mathcal{H}_0 does not depend on n_0 and is nonnegative, the test is also:

$$\max_{n_0} \left(2 \ln \frac{p(x; n_0, \mathcal{H}_1)}{p(x; \mathcal{H}_0)} \right) > 2 \ln \gamma \quad (3.65)$$

The GLRT decides \mathcal{H}_1 if

$$\max_{n_0} \left(N \ln \left(\frac{\hat{\sigma}_0^2}{(\hat{\sigma}_1^2)^{\frac{n_0}{N}} (\hat{\sigma}_2^2)^{\frac{N-n_0}{N}}} \right) \right) > \gamma' \quad (3.66)$$

where, again $\gamma' = 2 \ln \gamma$.

3.3 Experimental Model Validation

3.3.1 White and Uncorrelated Residuals

In order to apply the theory by [23], developed in the previous section for a EHSS, the residual used to detect a fault in leakage needs to be white or uncorrelated. In order to validate this assumption used in the detector design, an experiment is conducted on the EHSS shown in fig. 3.2 whose model and governing equations were presented in section 3.2. Position and velocity of the mass as well as pressure in each of the cylinder chambers are recorded every millisecond by the sensors when the EHSS is in steady-state with constant valve opening and during a total time of 100 s. Time record of the residual is given in fig. 3.6 together with its PDF. It results from the analysis of this signal that the distribution can be considered as Gaussian. Fig. 3.7 shows the power spectral

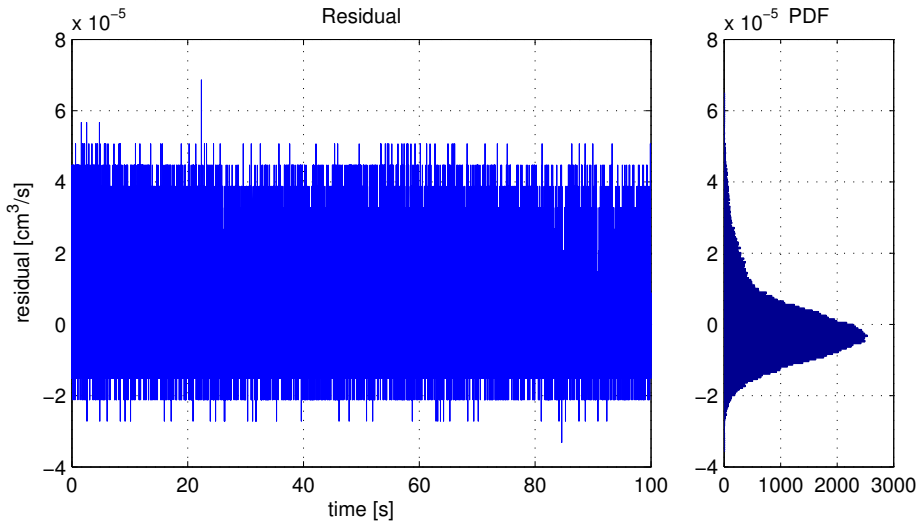


Figure 3.6: Residual signal from experiment

density (PSD) of the residual build from experiment data and hereby validates the assumption that the residual is white, i.e. its PSD is flat with frequency up to 900 Hz. Fig. 3.8, the autocorrelation function plot, also validates the white residual assumption by showing that each sample is uncorrelated with all the others.

From the experimental data, noise present in the load pressure measurement is found to be WGN with standard deviation $\sigma = 0.0963$. The same noise

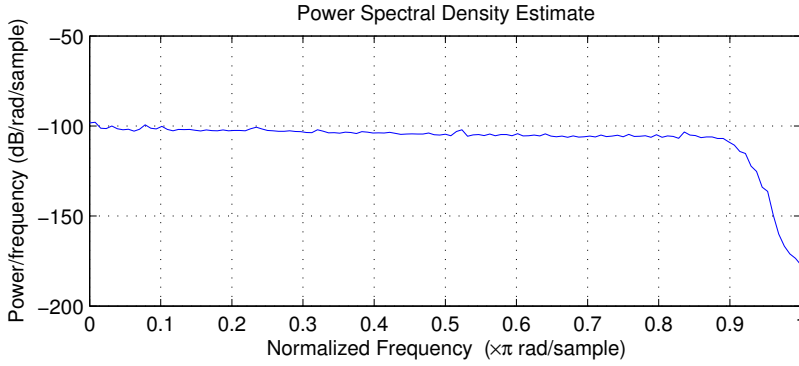


Figure 3.7: Power Spectral Density of residual from experiment.

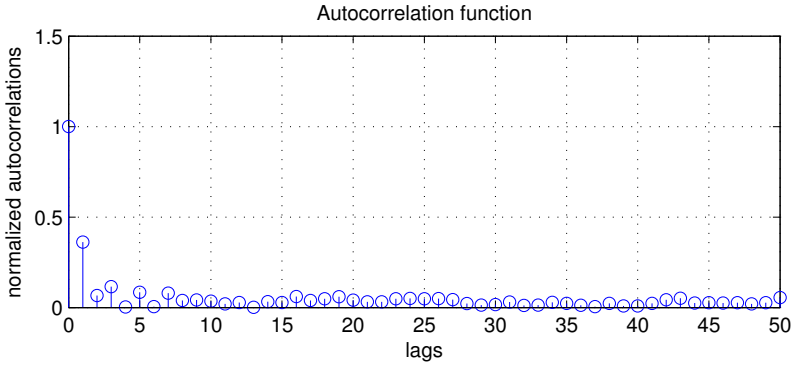


Figure 3.8: Normalized autocorrelation function of residual from experiment.

properties will be used in the next section to detect a simulated fault.

3.3.2 Comparison between experimental and simulated outputs

A comparison between simulated and experimental data is shown in figs. 3.3.2 and 3.3.2, where no leakage is included and results are not normalised.

The differences between the simulated and experimental data occurs mainly due to the use of LuGre friction model as an approximation of the real friction inside the cylinder, as the effect of lubricant film thickness inside the valve is not included.

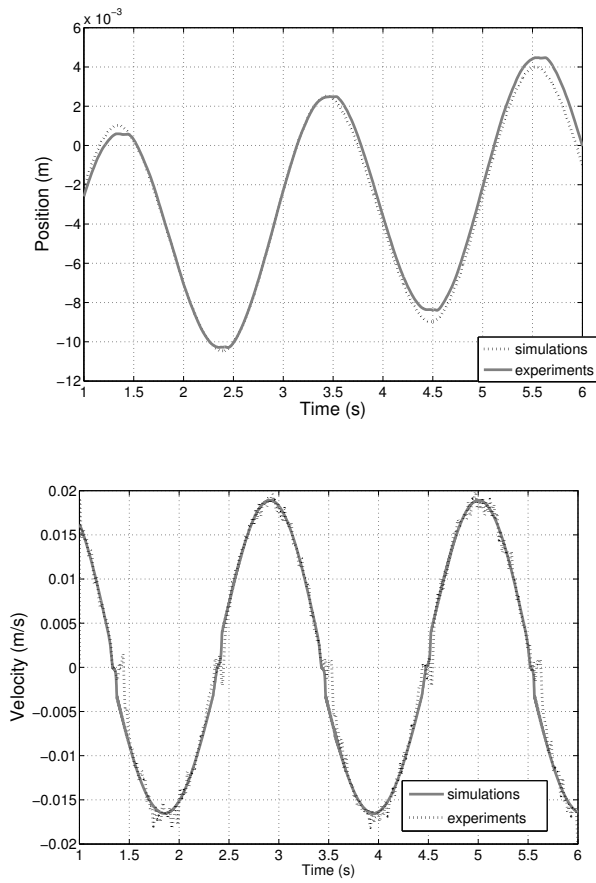


Figure 3.9: Simulated and measured position and velocity.

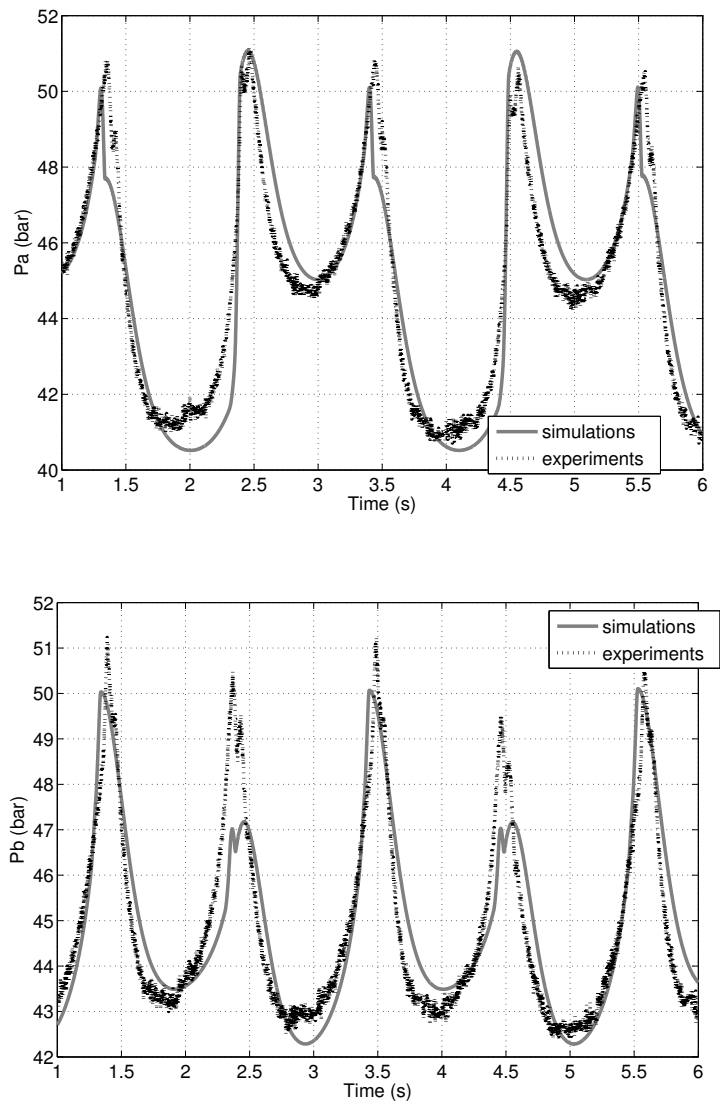


Figure 3.10: Simulated and measured pressure in chamber A and pressure in chamber B.

3.4 Detection and Prognosis of Faults

Two experiments are conducted where an internal leakage is introduced in the physical system (test bed) and the model based fault detector is to diagnose the leakage based fault.

3.4.1 Static Leakage Detection in a Position Controlled EHSS

In a first experiment, the hydraulic cylinder is loaded with a spring and damper and the position of the mass controlled by a proportional integral derivative (PID) controller. The mass position variation is neglected when a sufficient small leakage fault appears inside the cylinder. In this case, the normalised load pressure p_{Ln} is constant equal to 3% and the normalised valve opening x_{vn} is 0.24% before the fault occurs. This initial opening is the sign that an initial leakage in the fault-free case is present and approximately equal to $Q_{Leak0} = 0.9 \text{ l/min}$. Between time $t = 22.5 \text{ s}$ and $t = 25.6 \text{ s}$ when a fault caused by an increase of 1 l/min in the internal leakage, p_{Ln} stabilises to 3% again but x_{vn} takes a value of 0.5%. The residual calculated from eq. (3.29) is given in fig. 3.11 between time $t = 14 \text{ s}$ and $t = 35 \text{ s}$.

Fig. 3.12 shows the GLRT values for different jump times. The experiment is run for 23.5 s , the real jump time is at 22.5 s and the GLRT values are given for assumed jump times ranging from 21.5 s to 23.45 s . The highest value of the GLRT occurs at time close to $t = 22.6 \text{ s}$ and gives $GLRT = 511$, represented by a red dot on fig. 3.12.

Fig. 3.13 shows the GLRT with unknown jump time at different end times. For each of these end times a GLRT is run as in the previous figure and the maximum value is returned. The red dot in fig. 3.13 hence corresponds to the red dot in fig. 3.12. Fault detection is now possible using this latter test. For example if the threshold γ was fixed at 30, no false alarm would occur and the time to detect the fault would be 0.16 s . However, a different threshold is necessary to detect when the system is back to fault-free working operation.

In order to reduce the time to detect the leakage, to reduce the false alarm rate and to revert to non-faulty case when a fault disappears, a recursive cumulative GLRT with adaptive threshold and upper bounded is implemented. The algorithm for an upper bound $h = 90$ and an initial threshold $\gamma_0 = 30$ follows:

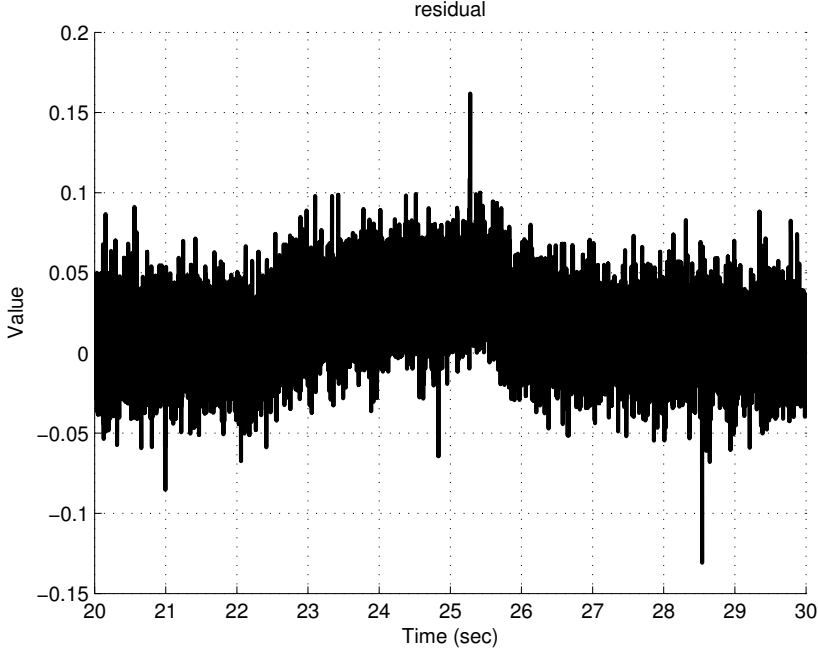


Figure 3.11: Residual signal from experiment. Fault in internal leakage occurs between time $t = 22.5$ s and $t = 25.6$ s, from 0.9 l/min to 1.9 l/min. Position of the mass is stabilised around a constant value with a PID controller.

Initialisation

$$h = 90$$

$$\gamma_0 = 30$$

Loop

$$\begin{aligned} g_k &= x_k - \gamma_{k-1} \\ \gamma_k &= x_k - \text{sign}(g_k) \min(|g_k|, \Delta) \\ g_k &= \max(0, g_{k-1} + g_k) \\ g_k &= \min(h, g_k) \end{aligned} \tag{3.67}$$

Result

$$g_k \quad \text{for increasing time } t_k$$

where x_k is the value at time t_k of the statistical test in eq. (3.66) and shown in

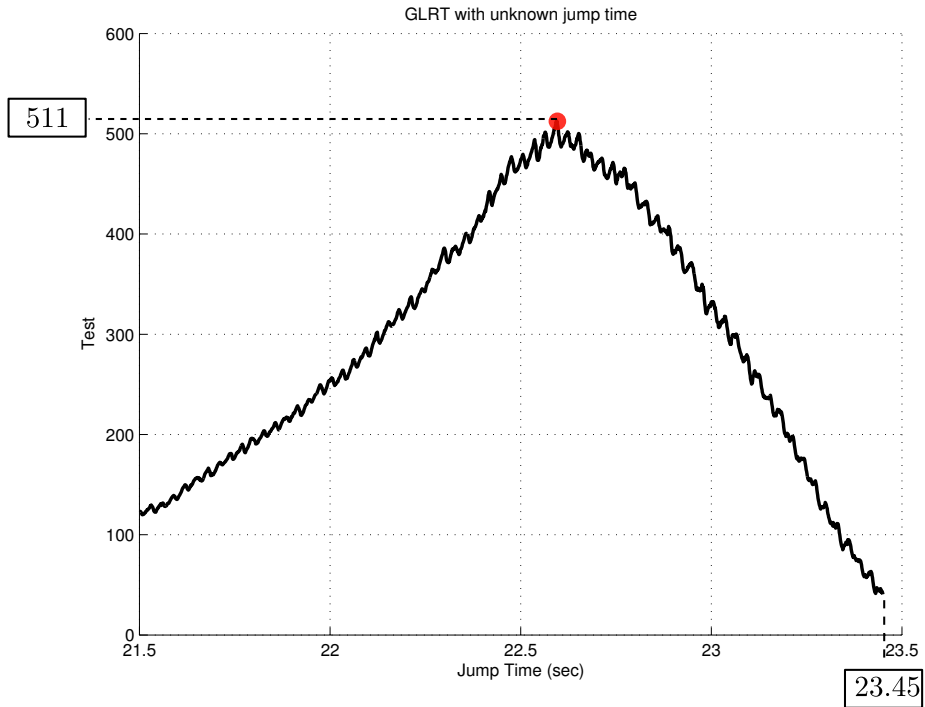


Figure 3.12: GLRT for different values of assumed jump time after 23.5 s of simulation. (Real jump time = 22.5 s.)

fig. 3.13, and where Δ is the maximum difference between the threshold and the statistical test. The motivation behind the threshold adaptivity is to decrease the time to detect fault reversion. The values g_k are given in fig. 3.14. The alarm or stopping time is the smallest time instant at which g_k crosses the given threshold h_1 . For h_1 equal to ten, detection time is equal to 0.16 s. The new detector does not trigger any false alarm. The final fault detection is plotted at the bottom of fig. 3.14.

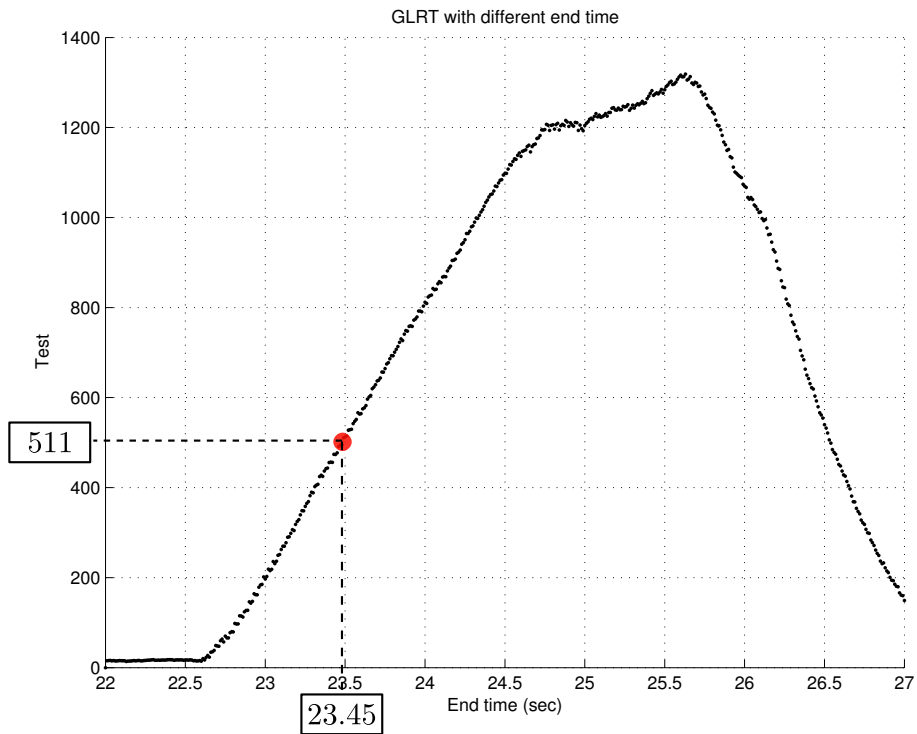


Figure 3.13: GLRT with unknown jump time.

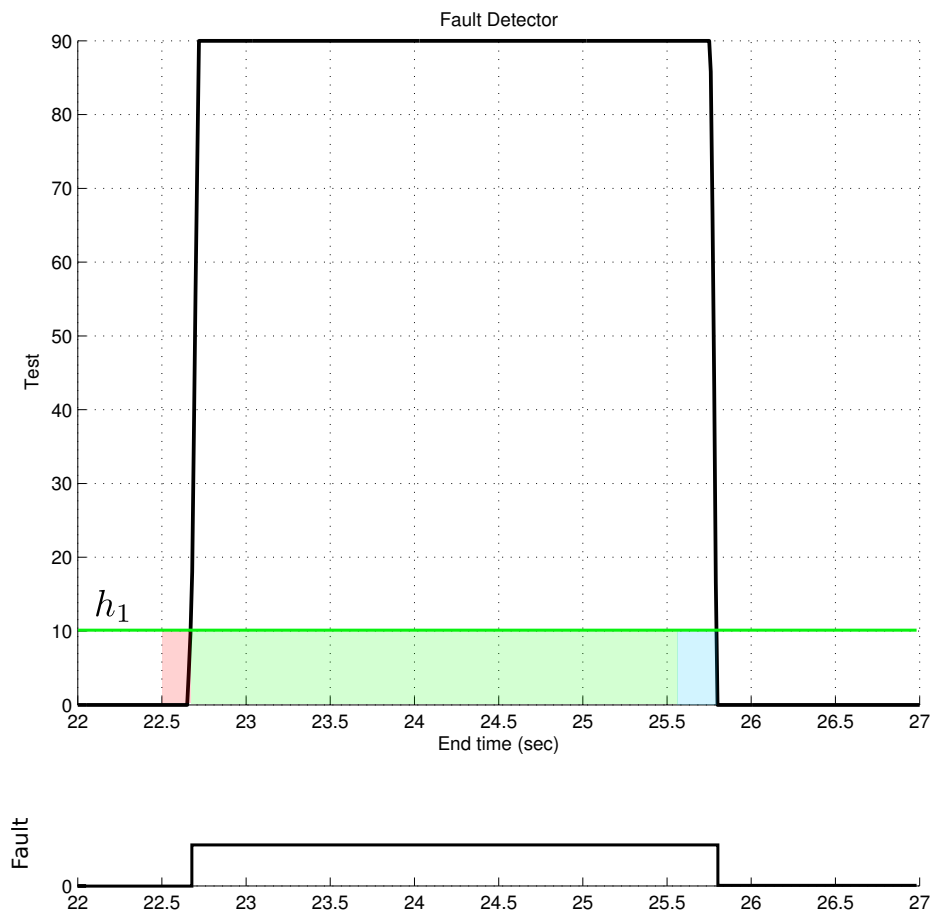


Figure 3.14: Fault detector with reversion. Thresholds $h_1 = 10$ (above, a fault is detected). Real fault occurs between 22.5 and 25.6 s. Red area is time to detect. Blue area is time to revert to non-faulty case.

3.4.2 Static Leakage Detection in a Force Controlled EHSS

A second experiment is conducted on the test bed shown in fig. 3.2, where the hydraulic cylinder is engaged and applies a constant force on an object. In contrast to the previous experiment where the load pressure and valve opening were low, in this configuration the load pressure is close to the supply pressure and the valve is open at 6% of the maximum opening. Since the load pressure is higher, an internal leakage fault has larger effect and smaller leakage can hence be detected. At time 16.5 s the initial internal leakage flow jumps from 0.9% to 1.3% of the nominal flow. This increase corresponds to an additional flow of 58 *ml/min* when the load pressure is equal to the supply pressure. The residual calculated from eq. (3.29) is given in fig. 3.15 between time $t = 15.5$ s and $t = 17.5$ s. In this case, a test as designed in section 3.2 is not needed since

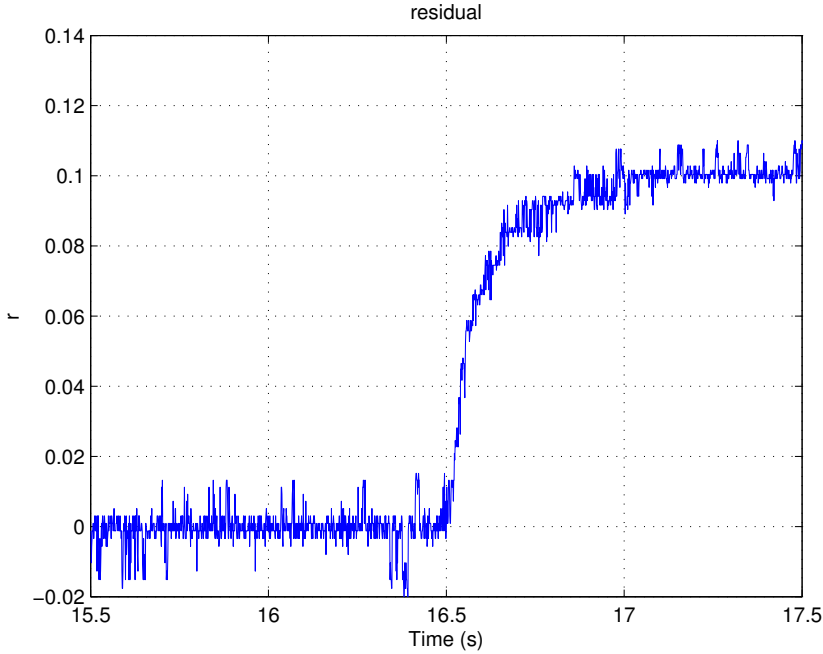


Figure 3.15: Residual signal from experiment. Fault in internal leakage occurs after time $t = 16.5$ s from 0.117 *l/min* to 0.175 *l/min*. The mass is in contact with a fixed object and a constant force is applied corresponding to a load pressure of 92% of the supply pressure.

a simple threshold at $h = 0.04$ for the residual can be used to detect such a fault. Smaller leakage fault still need to be investigated. However, adjusting

with sufficient precision a leakage flow with a correct magnitude to represent a realistic behaviour of a leakage across hydraulic cylinder chambers is a difficult task to realise in practice. In the following section, the simulation of a fault using the model described in section 3.2 is hence preferred. After estimation of the parameters in chapter 2 and noise characteristics in section 3.3, the model fits closely to the experimental test bench. A fault occurring between time $t = 14\text{ s}$ and $t = 15\text{ s}$ is introduced and is caused by an increase of 1 ml/min in the nominal leakage flow Q_{Leak} . The residual is given in fig. 4.13, for a 20 second simulation of the EHSS in steady-state with a constant valve opening.

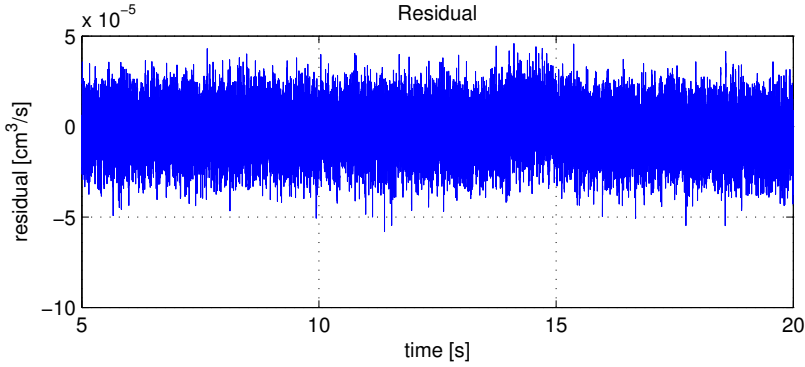


Figure 3.16: Residual signal from simulation. Fault in leakage occurs between time $t = 14\text{ s}$ and $t = 15\text{ s}$.

Fig. 3.17 shows the GLRT with unknown jump time for different simulation end times. Fault detection is now possible using this last test. For example if the threshold γ was fixed at 100, no false alarm would occurs and the time to detect the fault would be 0.4 s .

Using algorithm (3.67) with adaptive threshold and choosing $\Delta = 50$ in order to reduce the time to detect fault reversion, the values g_k are given in fig. 3.18. The alarm or stopping time is the smallest time instant at which g_k crosses the given threshold h_1 . For h_1 equal to 30, detection time is equal to 0.2 s . The new detector does not trigger any false alarm. The delay of reverting to non-faulty case from faulty is reduced if h is decreased. In the present case, $h = 90$ gives a reverting time equal to 0.25 s . In order to prevent the detector from switching excessively between the two cases, the falling edge threshold h_2 is taken as half the rising edge threshold, h_1 . The final fault detection is plotted at the bottom of fig. 3.18.

The fault case simulated here demonstrates the ability of the method to diagnose internal leakage flow fault as small as 1 ml/min when the EHSS is in steady-state.

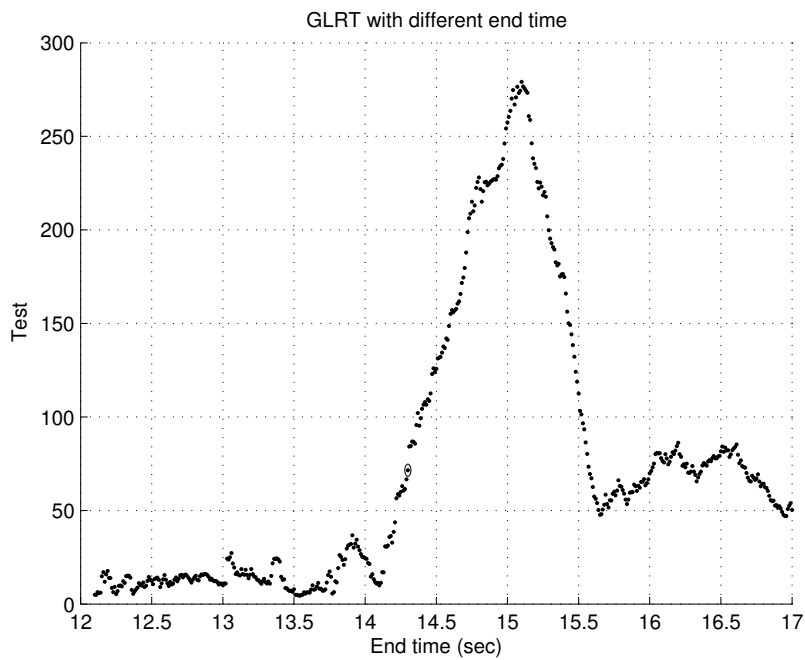


Figure 3.17: GLRT with unknown jump time.

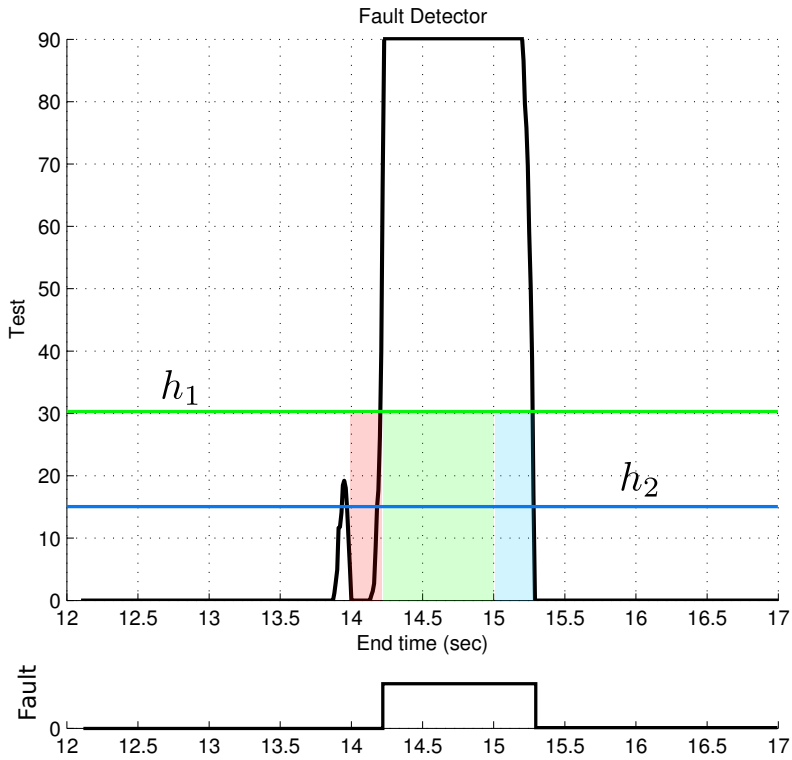


Figure 3.18: Fault detector with reversion. Thresholds $h_1 = 30$ (above, a fault is detected) and $h_2 = 15$ (below, a the detected fault is reset) . Real fault occurs between 14 and 15 s. Red area is time to detect. Blue area is time to revert to non-faulty case.

3.4.3 Dynamic Leakage Detection

The leakage fault detection is now investigated when the system is not in steady-state, i.e. when the inputs and outputs are not considered as constant. Two detectors were implemented, using respectively EKF and SAEKF to generate residuals as explained in section 3.1.2. In order to verify the performance of the detectors, a number of simulations and experiments were carried out where both internal and external leakages were created by opening/closing the control flow valves mounted on corresponding bypasses (see fig. 3.2 and 3.3). Simulations and experiments are implemented using Matlab/Simulink software. Four simulated and experimental cases are taken into account such as no leakage, internal leakage, external leakage and both internal and external leakage fault are present. The EHSS is run in open loop and the sampling time for the input and outputs is 1 ms. The input signal is a sine wave of frequency 3 Hz and amplitude 1 V centered on 0 V. A comparison between the simulated and experimental data is shown in figs. 3.3.2 and 3.3.2.

3.4.3.1 State Augmented Kalman Filter

Two scenarios were implemented using SAEKF. In the first scenario the measurements are simulated using eqs. 3.32-3.51, where the noise is added into the model. The system is in fault-free operating mode during the first two seconds, then an external leakage is added during the time intervals [2;4] and [6;8] seconds, whereas internal leakage is added during time interval [4;8] seconds. The normalised simulated measurements and their estimations using SAEKF are shown in figs. 3.19 and 3.20, while the estimated internal and external leakage flows are shown in fig. 3.21

In the second scenario the measured outputs are taken from the physical system, where the internal leakage occurs in time intervals [10-15] and [21-25] seconds and external leakage occurs in time intervals [0-5] and [21-25] seconds. Outside these intervals the system has no leakage related faults. The normalised measurements and estimations are shown in fig.3.22. The position measurements and estimations are very close and are not presented in the figure. The estimated leakages from output measurements are shown in fig. 3.23.

In simulations and experiments the leakage levels are the same as described in section 3.1.2 and given in percent of the nominal flow. The estimated leakages contain oscillations but faults related to them can be detected using averaging and thresholds. The initial state vector $x_i = 10^{-5}$, $i = 1, \dots, 7$ is the same for both simulated and experimental scenarios.

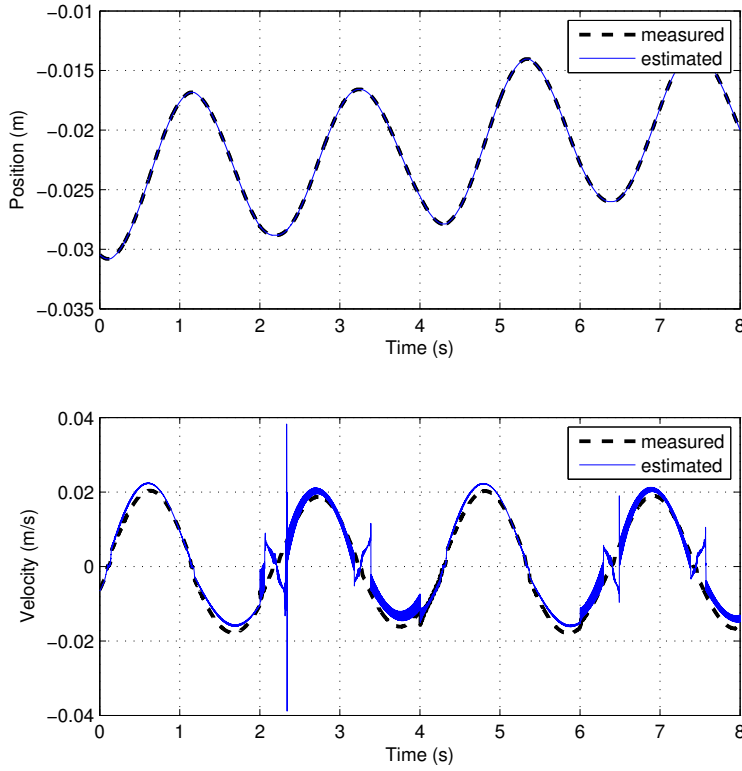


Figure 3.19: Simulated and estimated position and velocity.

3.4.3.2 Extended Kalman Filter

The same two scenarios are implemented using EKF. The integrals of the absolute values of the errors between measurements and estimations are summarised in table 3.2 when the measurements are simulated from the model with noise and in table 3.3 when the measurements are issued from the sensors of the test bed.

Each row represents a box of the partitioned leakage flow space and are labelled by NL for no leakage flow, IL for only internal leakage flow, EL for only external leakage flow and BL for both internal and external leakage flows. In both simulated and experimental scenarios the leakage levels used by EKF were 0.5 and 10 percent higher than actual external and internal leakage respectively in order to avoid perfect match between the measured and estimated states. The results show that the external leakage is more likely to be detected than inter-

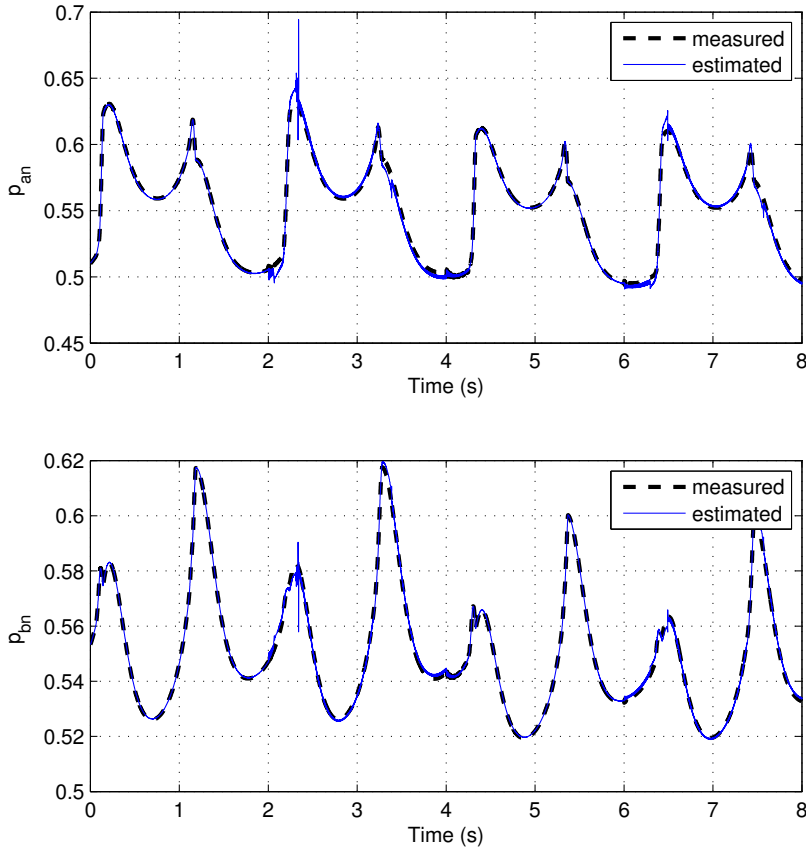


Figure 3.20: Simulated and estimated normalised load pressures.

nal leakage. The grey cells in table 3.3 represent the true case at the current time interval, i.e. when the model is best fit for the test bed configuration, and ideally the residuals in these cells should be smaller than all the other boxes in the same row. The time interval required for the fault detections depends on the tuning of matrices \mathbf{Q} and \mathbf{R} as well as the model accuracy.

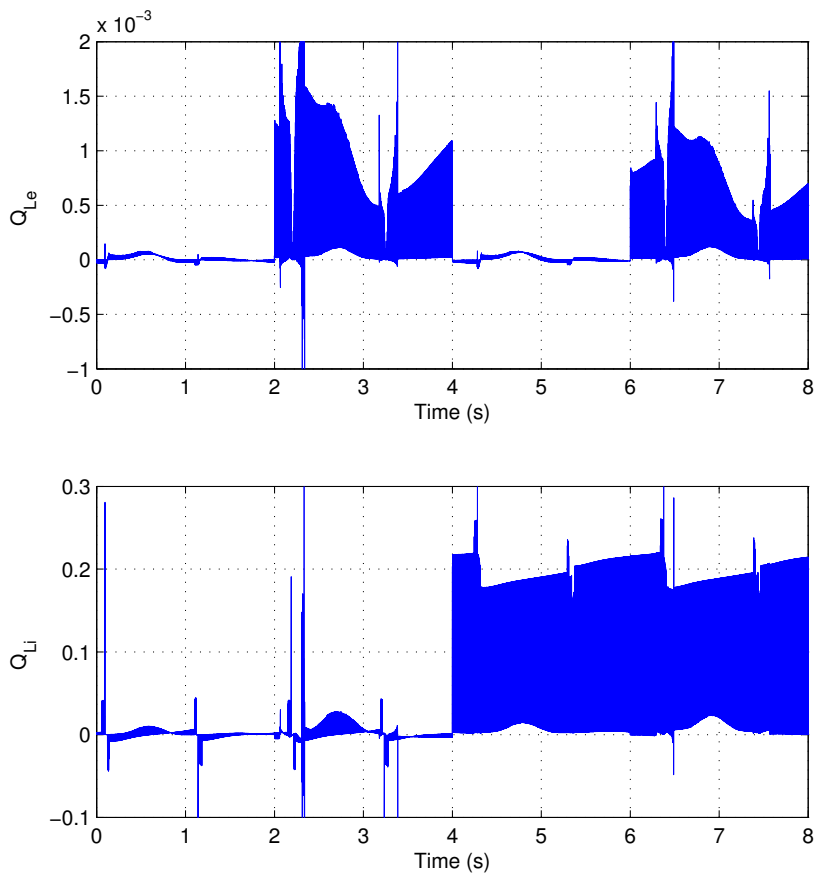


Figure 3.21: Estimated external and internal leakage flows.

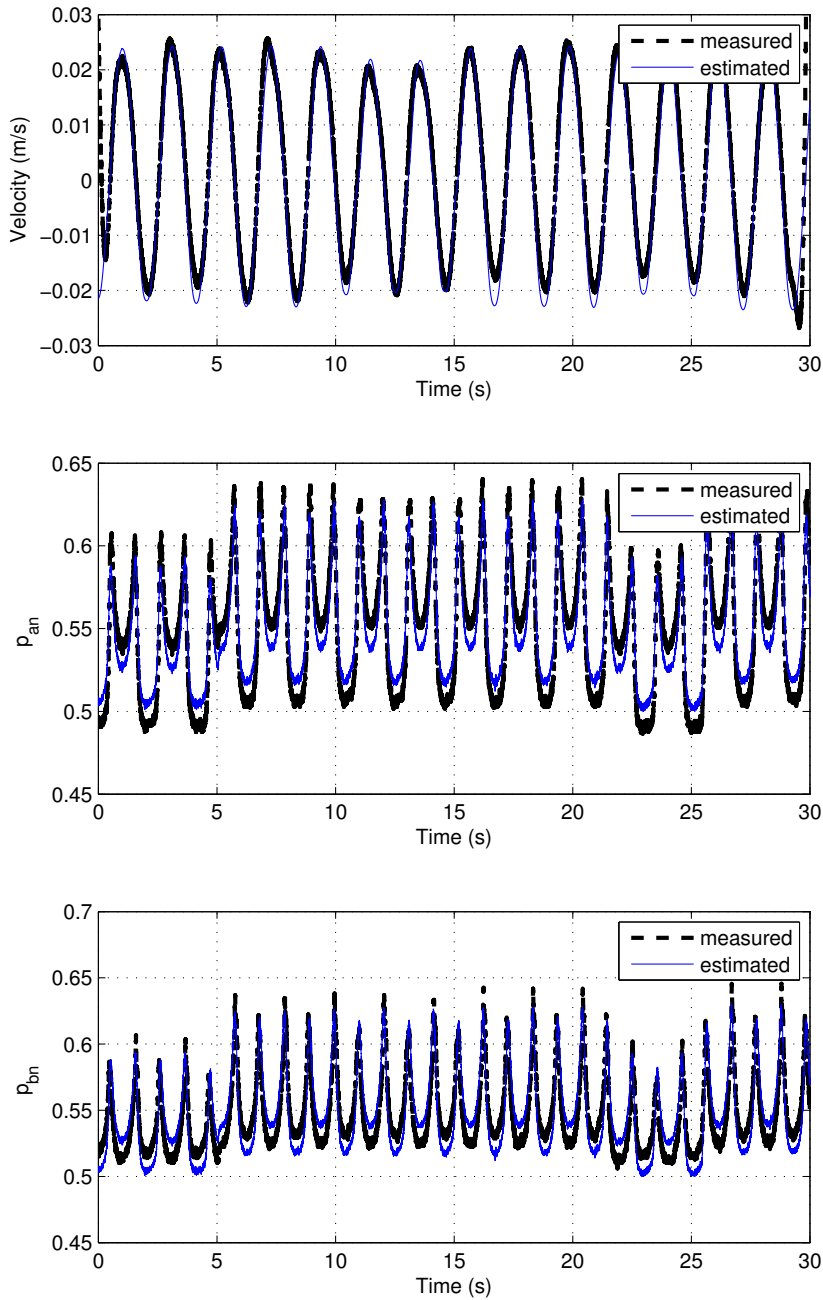


Figure 3.22: Measured and estimated velocity and normalised load pressures.

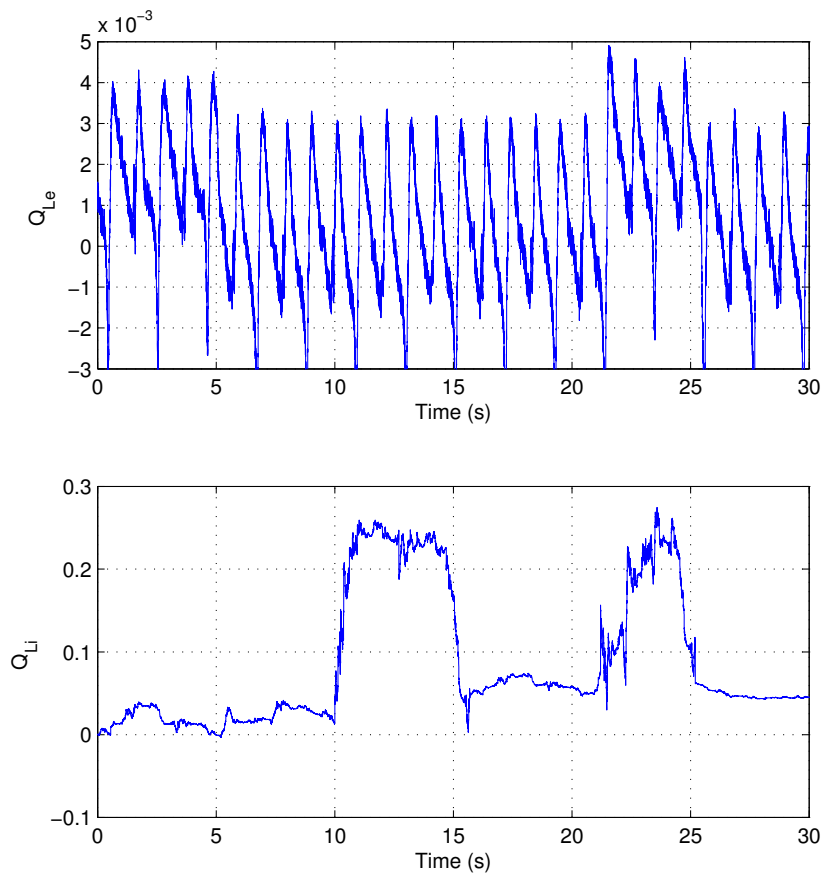


Figure 3.23: Estimated external and internal leakage flows.

Table 3.2: Residuals generated by different EKF's via simulations.

Con	Time	NL EKF	IL EKF	EL EKF	BL EKF
NL	0 s	0.0000	0.0000	0.0000	0.0000
	-	0.0022	0.0028	0.0080	0.0080
	0.5 s	0.0016	0.0017	0.0055	0.0057
IL	2 s	0.0001	0.0000	0.0001	0.0000
	-	0.0022	0.0018	0.0089	0.0085
	2.5 s	0.0013	0.0009	0.0062	0.0065
EL	4 s	0.0000	0.0001	0.0000	0.0001
	-	0.0056	0.0061	0.0020	0.0027
	4.5 s	0.0062	0.0059	0.0012	0.0013
BL	6 s	0.0000	0.0002	0.0001	0.0000
	-	0.0058	0.0063	0.0013	0.0012
	6.5 s	0.0071	0.0068	0.0012	0.0009

Table 3.3: Residuals generated by different EKF's via experiments.

Con	Time	NL EKF	IL EKF	EL EKF	BL EKF
NL	7 s	0.0000	0.0000	0.0000	0.0000
	-	0.0038	0.0057	0.0056	0.0066
	8 s	0.0039	0.0052	0.0039	0.0038
IL	12 s	0.0000	0.0000	0.0000	0.0000
	-	0.0050	0.0047	0.0048	0.0047
	13 s	0.0047	0.0047	0.0051	0.0053
EL	2 s	0.0000	0.0000	0.0000	0.0000
	-	0.0060	0.0060	0.0035	0.0048
	3 s	0.0075	0.0079	0.0059	0.0065
BL	22 s	0.0000	0.0000	0.0000	0.0000
	-	0.0045	0.0052	0.0049	0.0042
	23 s	0.0084	0.0083	0.0060	0.0057

3.5 Summary and Discussion

A fault detector for leakage in hydraulic cylinders was developed by initially considering a high fidelity model of a nonlinear hydraulic-mechanical system, then by implementing the fault detector on a test bed. Two different techniques were used depending on the system being in steady-state with constant velocity and load pressure or not. In the static case, using structural analysis, a robust residual was generated that accommodated unknown parameters and a composite hypothesis test was derived. Test rig measurements were used to validate the properties of residuals and experimental results demonstrated the performance and feasibility of the proposed method regarding prognosis of leakage. Two application examples were investigated: In the first one an internal leakage occurs as the position of the actuated mass is stabilised to a certain value by the mean of a controller. The second example represents the case when the system applies a constant force on a fixed object. In the more general case when the system is not in steady-state, since the internal friction state is not available from measurements, extended Kalman filter and state augmented Kalman filter were used to generate residuals. These residuals show that two types of fault, i.e. internal, external or both internal and external leakage, can be detected from the test bed measurements when the input is a sinusoidal signal.

Using the same methods as the one developed in this chapter, it is possible to detect and isolate faults related to the friction inside the hydraulic cylinder. If the system is in steady-state eq. 3.21 is used to generate a residual. Applying hypothesis testing to this residual, a fault related to friction can be detected. Whereas in the case of leakage detection, the same technique is also valid in the non steady-state behaviour by using constraint c_3 instead of s_4 , a residual cannot be generated in non steady-state for friction fault detection since the internal state z is not measured. However, the dynamic methods using SAEKF or EKF can be used instead. Both Kalman filters furnish an estimation of the state z and can be seen as a nonlinear observer for the system. The estimated value of z together with constraint c_2 lead to the generation of a residual for friction fault detection.

Future research directions are expected to include generalisation of this fault detector to the case of coloured noise in measurements or estimations and hence enable the present fault detector for prognosis of friction fault detection. Another key issue illustrated in this chapter when designing fault detector is the necessity for the model to be in close agreement with the physical system. Indeed, in order to detect external leakage flow, a model where the chamber pressures in the cylinder are two distinctive states, where the valve is not symmetric and the fluid is not considered as incompressible in the flow equations is necessary. Moreover it has been experienced that the performances of the two Kalman

filters are closely related to the model accuracy.

The implementation of the different fault detectors in this chapter was made offline, i.e. the measurements were taken in real-time but not analysed simultaneously. Especially for the SAEKF the computational time was excessive (12 times higher than when running EKF). However, by algorithm optimisation future research directions are expected to include real-time implementation of the fault detectors on the test bed and on the industrial counterparts in the offshore industry.

CHAPTER 4

Adaptive Nonlinear Control Design

The nonlinear nature of electro hydraulic servo systems (EHSS) and presence of model uncertainties make use of advanced control strategies necessary in highly demanding applications. Nonlinear adaptive and robust control techniques are essential in order to obtain high performance for a wide range of operating points. In this chapter, classical linear control techniques are first applied. Performances and robustness of the different linear controllers are analysed through simulations and experiments and used as references for comparison with nonlinear advanced controllers designed in the next section. Based on Lyapunov stability and the model developed in chapter 2, several adaptive nonlinear controllers are designed and one is implemented in a last section on an experimental test bed.

4.1 Linear Control Design

In order to understand the challenge of controlling EHSS, in this first section the problems are illustrated by using classical controllers with linearised model.

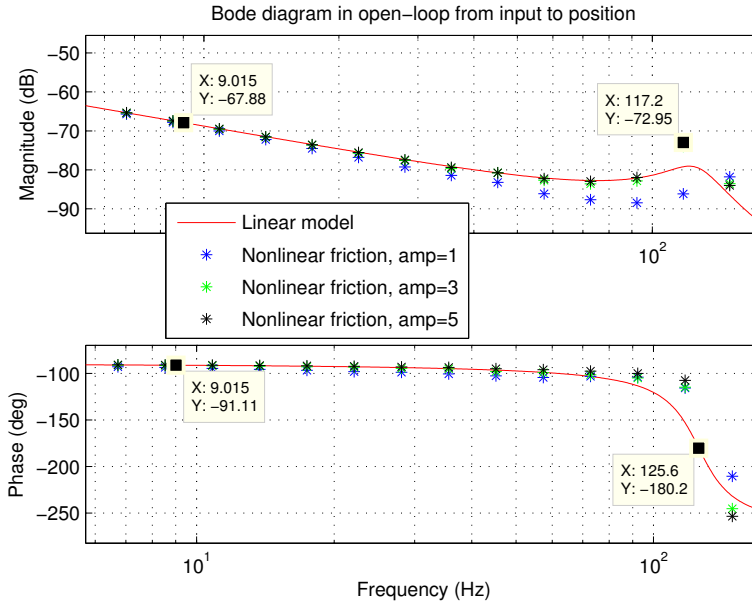


Figure 4.1: Input to position Bode diagram using a linearised model and the nonlinear model with different excitation amplitude: 5V, 3V and 1V and with the datatips used for proportional controller design.

4.1.1 Proportional Controller

Before designing high performance controllers for hydraulic servo systems, one has to know first what performance may be attained with a simple and ubiquitous proportional, integral and derivative (PID) compensator which is probably still the industry standard, possibly combined with a feedforward model. When the system contains an open-loop integrator, a proportional control can sometimes suffice. Fig. 4.1 shows the frequency response of the linearised model eqs. (2.41- 2.45) in red line (the load is disconnected) and the corresponding nonlinear model for different input amplitudes (stars) as in fig. 2.35. For a 11dB gain margin, it is read from the figure that a proportional gain of 2500 corresponding to a gain lift of 67.88 dB is necessary. Both from the model and from experiment, it is checked that a higher gain brings the system to instability.

Using a simple proportional controller $u = k_P(y_{ref} - y)$, where y_{ref} is the reference position, u is the input to the valve, y is the measured mass position and $k_P = 2500$ is the proportional gain, position tracking of a sine wave reference

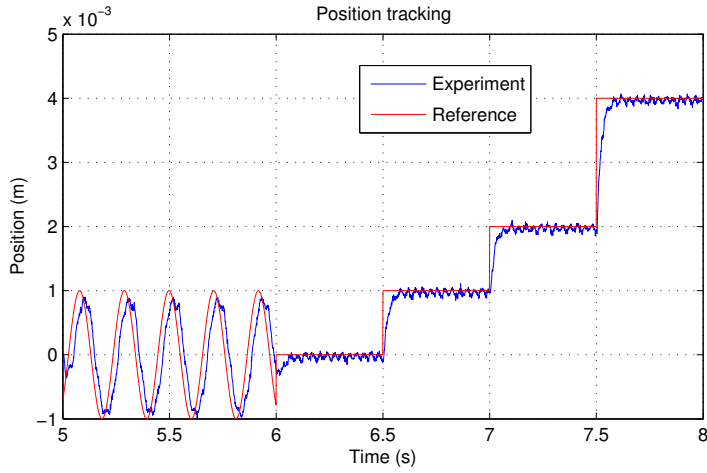


Figure 4.2: Position tracking from testbed.

followed by a sequence of steps is given in fig. 4.2, the corresponding position error in fig. 4.3 and input usage in fig. 4.4

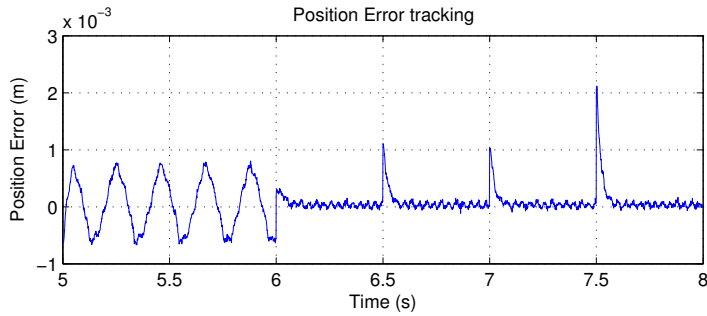


Figure 4.3: Error.

Finally the performances of the controlled system are summarised in table 4.1.

It results from this analysis that the proportional controller gives moderate performances and improvements can be achieved by increasing the bandwidth of the closed-loop system.

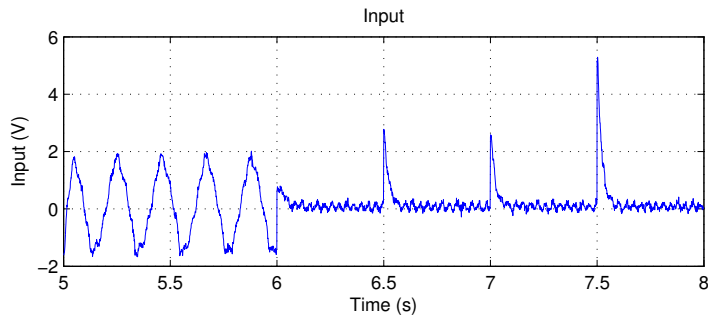


Figure 4.4: Input usage.

Table 4.1: Performances of the proportional controlled EHSS

Parameter	Value
Steady-state error constant(K_v)	57
Gain margin	11.4 dB
Phase margin	88.9°
Phase margin frequency	9.1 Hz
Closed-loop bandwidth	9.3 Hz
Percentage overshoot	0
Rise time	37 ms

4.1.2 Lag Compensator

One way of improving the performances is to increase the gain of the controller at low frequencies in order to decrease the static error to a ramp and to increase the bandwidth. Such a controller is called a lag compensator because of the lag introduced in the phase. Its frequency response as well as the frequency response of the compensated system in open-loop is shown in fig. 4.5. In the design, the gain margin was kept the same as before in order to ensure similar robustness with regards to the uncertainties due to unmodelled nonlinearities related to for example friction. The expression for the lag compensator is given below:

$$K_L(s) = 0.1 \frac{s + 100}{s + 10} \quad (4.1)$$

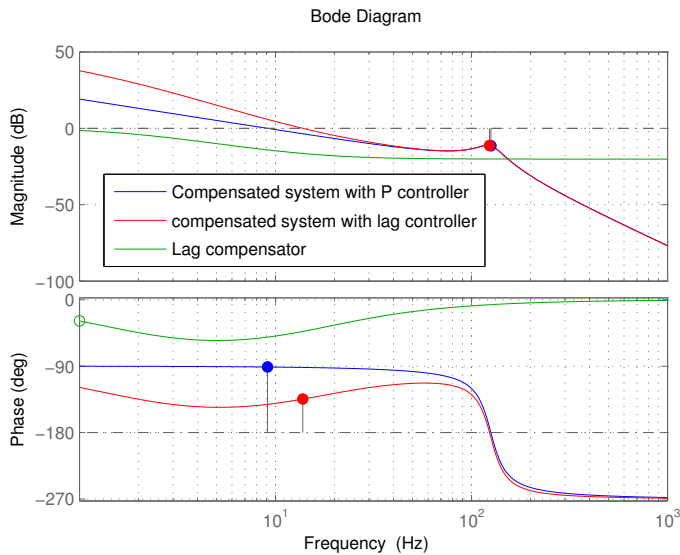


Figure 4.5: Frequency response for compensated system from input to position in open-loop.

Compared with a proportional controller, when using a lag compensator, the performances shown in table 4.2 are improved: the bandwidth is doubled and a tenfold improvement in the static error for a ramp is obtained. However, the overshoot is no longer zero because of the decrease in the phase margin. Experimental results are shown later in section 4.3 where several controllers are

compared.

Table 4.2: Performances of the lag compensated EHSS

Parameter	Value
Steady-state error constant (K_v)	570
Gain margin	11.3 dB
Phase margin	45.4°
Phase margin frequency	13.8 Hz
Closed-loop bandwidth	20.4 Hz
Percentage overshoot (%)	30
Rise time	13 ms

4.1.3 Robust H_∞ Controller

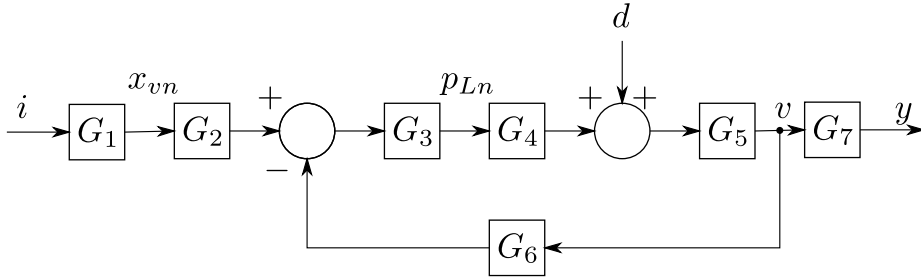
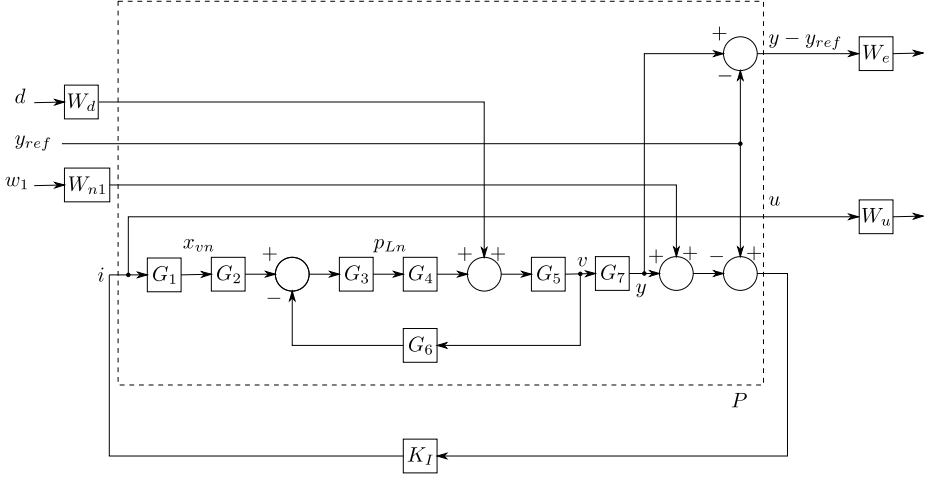


Figure 4.6: Block diagram for the linearised system.

The linearised system (2.41 - 2.45) is represented in the block diagram in Fig. 4.6 where d is a disturbance, $u = i$ is the input, y the output and where:

$$\begin{aligned}
 G_1(s) &= \frac{\omega_v^2 K_v}{s^2 + 2\zeta_v \omega_v s + \omega_v^2} & G_2(s) &= Q_n \\
 G_3(s) &= \frac{\beta_e}{p_s s + \beta_e (Q_{Leak} + Q_n \text{sign}(x_{vn}) \frac{\epsilon}{2})} & G_4(s) &= F_h \\
 G_5(s) &= \frac{1}{Ms + \sigma_2} & G_6(s) &= A_e \\
 G_7(s) &= \frac{1}{s}
 \end{aligned}$$

The H_∞ optimization problem can be formulated by the general configuration shown in Fig. 4.7, where y_{ref} is the reference and w_1 is the noise in the

Figure 4.7: H_∞ control problem.

position measurement. The objective is to design a feedback controller K_I which minimizes the norm $\|u\|_2$ with respect to the measurement noise. Let $z(t) = [W_u u(t), W_e(y(t) - y_{ref}(t))]^T$ and $w(t) = [W_d d(t), W_{n1} w_1(t)]^T$, then the objective is equivalent to finding K_I that minimizes

$$\|F_l(P, K_I)\|_\infty = \max_{w(t) \neq 0} \frac{\|z(t)\|_2}{\|w(t)\|_2} \quad (4.2)$$

which is a standard H_∞ optimal control problem. The weights W_d and W_{n1} describe the relative importance of the disturbances and noise signals. The noise signal has a mean value of zero and is hence best described by its standard deviation σ_1 . The disturbance can be considered as a sinusoidal signal of amplitude A_d , best described by its effective value $A_d/\sqrt{2}$. The weight W_e and W_u are chosen so that the error $(y - y_{ref})$ is penalised at low frequencies and input usage is penalised at high frequencies. Thus a low-pass filter and a high-pass filter are chosen for the weights W_e and W_u respectively. The different weights are given below:

$$\begin{aligned} W_d &= \frac{A_d}{\sqrt{2}}, & A_d &= 10, \\ W_{n1} &= 2.8 \times 10^{-5}, \\ W_e &= A_e \frac{s/M_f + \omega_b}{s + A_f \omega_b}, & A_e &= \frac{5}{M_f}, & M_f &= 1.5, & \omega_b &= 800, & A_f &= 0.001 \\ W_u &= \frac{s + B_f}{s + \omega_b}, & B_f &= 0.00001 \end{aligned}$$

Running the general H_∞ algorithm of [15] with a tolerance of $tol = 0.01$ gives a minimum value for $\|F_l(P, K_I)\|_\infty$ equal to $\gamma^* = 437$ with a controller gain of 30.6×10^9 for the input. Stopping the algorithm when $\|F_l(P, K_I)\|_\infty$ has reached $\gamma = 1.05\gamma^*$ the controller K_I gain is reduced to 593×10^3 . This significant decrease justifies the need to take $\gamma = 1.05\gamma^*$. Indeed the energy required by the controller will be reduced. The controller is given below:

$$K_I(s) = \frac{593600(s + 5000)(s + 0.125)(s^2 + 1106s + 4.77e05)}{(s + 1268)(s + 624)(s + 5)(s^2 + 829s + 3.79e05)} \times \dots \quad (4.3)$$

$$\frac{(s^2 + 649s + 2.64e06)}{(s^2 + 647s + 2.63e06)}$$

Implementing the new controller K_I , it is now possible to simulate the compensated system. Its frequency response in open-loop is plotted in fig. 4.8 together with the proportional and lag compensated system, and its simulated performances are shown in table 4.3. Experimental time response is shown later in section 4.3 where several controllers are compared.

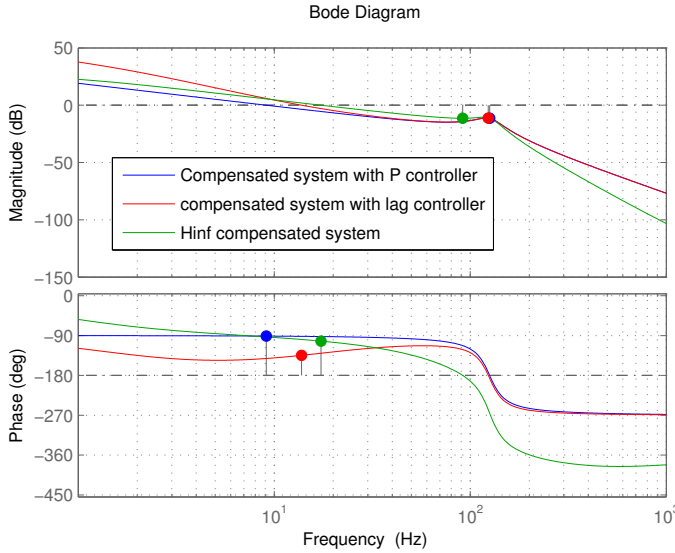


Figure 4.8: Frequency response for compensated system from input to position in open-loop.

Compared with the other linear controllers, the EHSS performs better regarding bandwidth, rise time and overshoot when using H_∞ optimal control but with a

Table 4.3: Performances of the H_∞ compensated EHSS

Parameter	Value
Steady-state error constant (K_v)	2.7
Gain margin	11.4 dB
Phase margin	77.5°
Phase margin frequency	17.3 Hz
Closed-loop bandwidth	24.2 Hz
Percentage overshoot (%)	0
Rise time	18 ms

higher static error as shown in fig. 4.9. If zero static error for a step is required, an integral action must be added to the H_∞ controller.

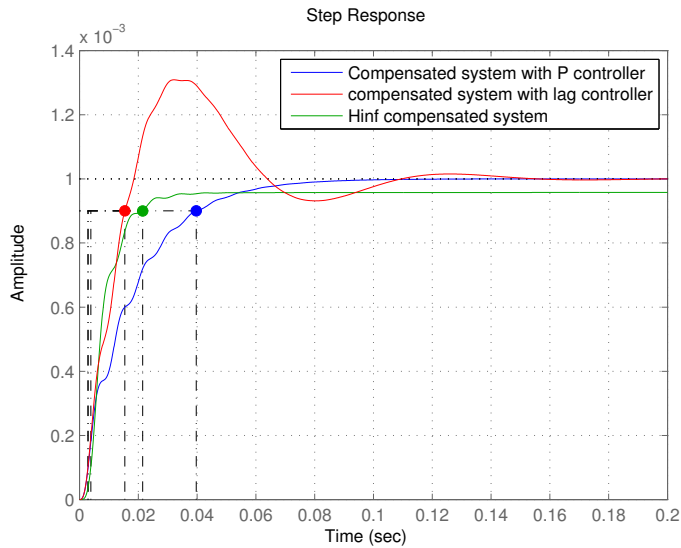
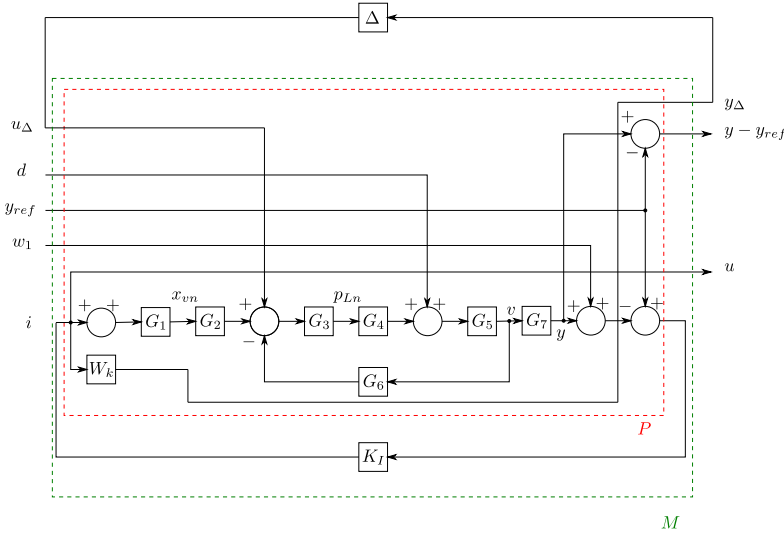


Figure 4.9: Step response for compensated system using proportional, lag and H_∞ optimal control.

Robustness analysis The amount of uncertainties in the actuator that the controller can tolerate before the system becomes unstable is now investigated in order to analyse and quantify the controller robustness. The nominal single input single output system from reference to mass position and its closed-loop

Figure 4.10: H_∞ M- Δ structure.

transfer function stability is under scrutiny.

First, the model uncertainty, i.e. the difference between the actual system on the testbed and the model system which was used to design the controller, is analysed. Uncertainty can be described as parametric and unmodelled dynamics combined into a single lumped complex perturbation Δ normalised such that $\|\Delta(j\omega)\|_\infty \leq 1$ as used in [39] and represented in fig. 4.10 and by the expression below:

$$G_p(s) = G(s)(1 + w_k(s)\Delta(s)); \quad |\Delta(j\omega)| < 1, \forall \omega \quad (4.4)$$

where G_p is any perturbed plant, G is the nominal plant, (without uncertainties) and w_k is a multiplicative weight introduced in order to normalise the perturbation. This weight is obtained by choosing a low order transfer function which satisfies:

$$|w_k(j\omega)| \geq l_k(\omega), \quad \forall \omega$$

Where $l_k(\omega)$ for each frequency is the smallest radius which includes all the possible plants and calculated as follows:

$$l_k(\omega) = \max_{G_p} \left| \frac{G_p(j\omega) - G(j\omega)}{G(j\omega)} \right| \quad (4.5)$$

When considering the friction nonlinearities as uncertainties, the three frequency responses shown in fig. 2.35 corresponding to three different input amplitudes can be seen as three perturbed plants or the two frequency responses in fig. 2.37

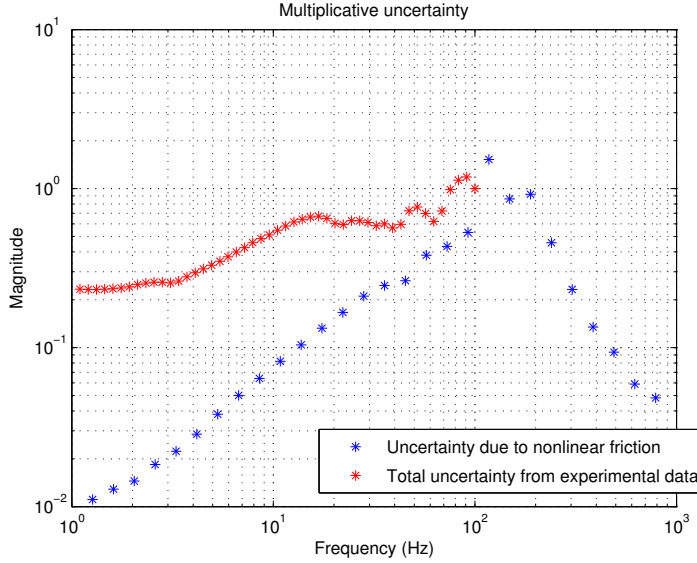


Figure 4.11: Multiplicative uncertainties caused by nonlinear friction model (blue) and total uncertainties when considering the actual system (red). Nominal model is the linearised model

of the actual system for two different input amplitudes can also be seen as two perturbed plants when the linearised model serves as reference. The maximum relative uncertainty, $\max_{G_p} \left| \frac{G_p(j\omega) - G(j\omega)}{G(j\omega)} \right|$, for each frequency is shown in fig. 4.11. The weight $w_k(s)$ can be derived such that it lies at frequency above the red and blue stars. At frequencies 80-120 Hz, $|w_k(jx\omega)| > 1$ which means that the Nyquist curve may pass through the origin. It follows that the input has no effect on the output and tight control is not possible [39].

Second, the robustness of the H_∞ optimal controller is investigated by calculating how much uncertainties it can tolerate before the system becomes unstable. Using Nyquist stability condition, the requirement for robust stability can be expressed as:

$$\|w_k\|_\infty < 1/\|T\|_\infty \quad (4.6)$$

where T is the complementary sensitivity function. The value of the upper bound, $1/\|T\|$, for w_k at different frequencies are represented in fig. 4.12. This upper bound does not constrain the weight since it is greater than one for all frequencies and greater than 2 between frequencies 80-120 Hz.

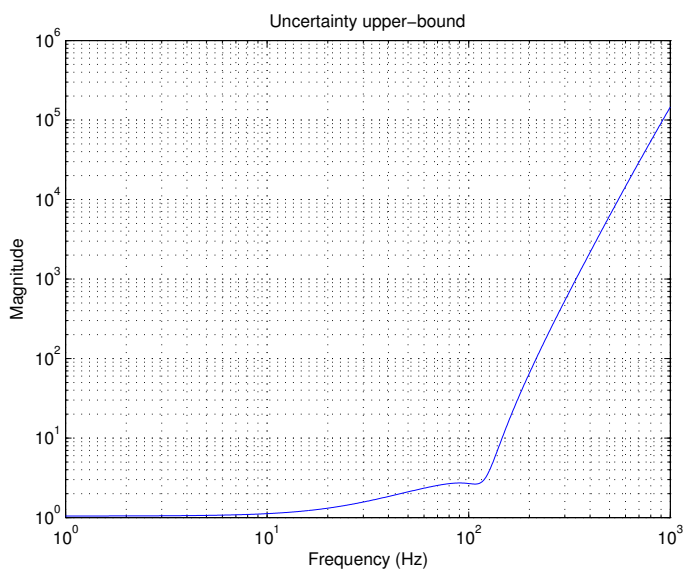


Figure 4.12: Upper-bound, $1/|T|$, for the weight $|w_k(s)|$ in order for the system to be robust stable.

4.2 Adaptive Backstepping

During the 90's, backstepping proved to be a powerful tool for stabilizing nonlinear systems [26], where nonlinearities are not constrained by linear bounds.

However it was first limited to the so-called class of “parametric pure-feedback” (or lower triangular) systems and global stability is achieved for the subclass of “parametric strict-feedback systems”. Moreover when some of the states are not measurable, solutions are restricted to a narrower class of minimum phase systems in which the nonlinearities depend only on the output variable. For example, in the case of a third order system, it belongs to the **pure-feedback** class if it can be written as:

$$\begin{aligned}\dot{x}_1 &= k_1 x_2 + \varphi_1^T(x_1, x_2)\theta \\ \dot{x}_2 &= k_2 x_3 + \varphi_2^T(x_1, x_2, x_3)\theta \\ \dot{x}_3 &= k_3 u + \varphi_3^T(x_1, x_2, x_3)\theta\end{aligned}\tag{4.7}$$

where the θ vector and the k_i are constant and unknown. Restrictively, it belongs to the **strict-feedback** subclass if it can be written as:

$$\begin{aligned}\dot{x}_1 &= k_1 x_2 + \varphi_1^T(x_1)\theta \\ \dot{x}_2 &= k_2 x_3 + \varphi_2^T(x_1, x_2)\theta \\ \dot{x}_3 &= k_3 u + \varphi_3^T(x_1, x_2, x_3)\theta\end{aligned}\tag{4.8}$$

When uncertain or unknown parameters are separated from the control input u by more than one integrator, as for example parameters k_1 and θ in the first equation of system (4.8), the *matching condition* or *extended matching condition* no longer prevails but adaptive backstepping can still be used in order to globally stabilise the system. In addition tuning functions developed by Krstić can be used to remove overparametrisation. See [26] and references therein.

In this section, adaptive backstepping is applied to EHSS considering valve dynamics, and dynamic friction model. Simulations show the benefits of this nonlinear control design compared with linear techniques and the importance of a high fidelity model for improving control performance.

However, adaptive backstepping requires analytical model differentiation [1] which leads to an “explosion of terms” and hence renders the real implementation when using detailed model too difficult. However, by using a modified structure of the controller a real implementation of adaptive backstepping is realised on a EHSS and exhibits good performances.

Uncertain parameters The moving mass M which can be measured in an experimental test rig is nonetheless considered as uncertain in order to allow for a large range of applications as for example pick and place manipulation. Friction parameters, which can be identified with experiment contain also uncertainties due to different oil characteristics and wear inside the cylinder. Finally, the mechanical system contains uncertainties in the load (spring coefficient and damping coefficient which are null for the non-faulty case). The adaptive controllers presented in this section handle all the uncertainties described above.

4.2.1 Backstepping without Valve Dynamics

In order to demonstrate the effects of introducing valve dynamics in the backstepping controller, a controller without considering valve dynamics is developed first. The complete controller including valve dynamics is presented in section 4.2.2.

The system without valve dynamics can be rewritten as:

$$\dot{v} = -\frac{k}{M}y - \frac{d + \sigma_2}{M}\dot{y} + \frac{\eta_{hmc}F_h}{M}p_{Ln} \quad (4.9)$$

$$\begin{aligned} \frac{\eta_{hmc}F_h}{M}\dot{p}_{Ln} = & -\frac{\beta_e A_e \eta_{hmc} F_h}{p_s M}v - \frac{\beta_e Q_{Leak} \eta_{hmc} F_h}{p_s M}p_{Ln} \\ & + \frac{\beta_e Q_n \eta_{hmc} F_h}{p_s M} \sqrt{1 - \text{sign}(x_{vn})p_{Ln}} \text{sat} \left(x_{vn}, \frac{L}{x_{vmax}} \right) \end{aligned} \quad (4.10)$$

where hydraulic friction is modelled by η_{hmc} , hydro-mechanical efficiency of the cylinder, and σ_2 , damping coefficient. Alternatively, defining the states $(x_1, x_2, x_3) = (y, v, \frac{\eta_{hmc}F_h}{M}p_{Ln})$, the system becomes:

$$\dot{x}_1 = x_2 \quad (4.11)$$

$$\dot{x}_2 = x_3 + \varphi_2(x_1, x_2)^T \theta \quad (4.12)$$

$$\dot{x}_3 = b f(x_3)u + \varphi_3(x_2, x_3)^T \theta \quad (4.13)$$

where $\theta = [\theta_1, \dots, \theta_4]^T = \left[\frac{-k}{M}, \frac{-(d+\sigma_2)}{M}, \frac{-\beta_e A_e \eta_{hmc} F_h}{p_s M}, \frac{-\beta_e Q_{Leak}}{p_s} \right]^T$ is the vector of uncertain parameters, $\varphi_2(x_1, x_2) = [x_1, x_2, 0, 0]^T$, $\varphi_3(x_2, x_3) = [0, 0, x_2, x_3]^T$, $f(x_3) = \sqrt{\eta_{hmc}F_h/M - \text{sign}(x_{vn})x_3}$ is a known function and $b = \frac{\beta_e}{p_s} Q_n \sqrt{\eta_{hmc} \frac{F_h}{M}}$ is an uncertain parameter.

Following the tuning function design as in [26], the state space system (4.11-4.13), which is in a strict feedback form can be decomposed in successive subsystems for which tuning functions $\tau_i, i = 1 \dots 3$ and stabilizing functions

$\alpha_i, i = 1 \dots 3$ are recursively found, leading to the final adaptive control law u and the final update laws for the uncertain parameters θ and $\lambda = \frac{1}{b}$ with estimated $\hat{\theta}$ and $\hat{\lambda}$. Note that the symbol \sim defines the estimation error, i.e. $\tilde{\theta} = \theta - \hat{\theta}$.

Coordinate Transformation

$$z_1 = x_1 - y_r \quad (4.14)$$

$$z_2 = x_2 - y_r^{(1)} - \alpha_1 \quad (4.15)$$

$$z_3 = x_3 - y_r^{(2)} - \alpha_2 \quad (4.16)$$

Regressor

$$\omega_1 = 0 \quad (4.17)$$

$$\omega_2 = \phi_2 \quad (4.18)$$

$$\omega_3 = \phi_3 - \frac{\partial \alpha_2}{\partial x_2} \phi_2 \quad (4.19)$$

Tuning functions for $\hat{\theta}$:

$$\tau_1 = 0 \quad (4.20)$$

$$\tau_2 = \omega_2 z_2 \quad (4.21)$$

$$\tau_3 = \tau_2 + \omega_3 z_3 \quad (4.22)$$

Stabilizing functions:

$$\alpha_1(x_1, y_r) = \bar{\alpha}_1 \quad (4.23)$$

$$\alpha_2(x_1, x_2, \hat{\theta}, y_r, \dot{y}_r) = \bar{\alpha}_2 \quad (4.24)$$

$$\alpha_3(\bar{x}_3, \hat{\theta}, \bar{y}_r^{(2)}, \hat{\lambda}) = \frac{\hat{\lambda}}{f(x_3)} \bar{\alpha}_3 \quad (4.25)$$

where $\bar{x}_3 = (x_1, x_2, x_3)$, $\bar{y}_r^{(2)} = (y_r, y_r^{(1)}, y_r^{(2)})$ and:

$$\bar{\alpha}_1 = -L_1 z_1 \quad (4.26)$$

$$\bar{\alpha}_2 = -z_1 - L_2 z_2 - \omega_2^T \hat{\theta} + \frac{\partial \alpha_1}{\partial x_1} x_2 + \frac{\partial \alpha_1}{\partial y_r} \dot{y}_r \quad (4.27)$$

$$\bar{\alpha}_3 = -z_2 - L_3 z_3 - \omega_3^T \hat{\theta} + \frac{\partial \alpha_2}{\partial \hat{\theta}} \Gamma \tau_3 + \sum_{k=1}^2 \left(\frac{\partial \alpha_2}{\partial x_k} x_{k+1} + \frac{\partial \alpha_2}{\partial y_r^{(k-1)}} y_r^{(k)} \right) \quad (4.28)$$

Adaptive control law:

$$u = \alpha_3 + \frac{\hat{\lambda}}{f(x_3)} y_r^{(3)} \quad (4.29)$$

Parameter update laws:

$$\dot{\hat{\theta}} = \Gamma \tau_3 \quad (4.30)$$

$$\dot{\hat{\lambda}} = -\gamma \operatorname{sign}(b) \left(y_r^{(3)} + \bar{\alpha}_3 \right) z_3 \quad (4.31)$$

Error system: The design procedure (4.14-4.31) results in the following error system:

$$\dot{z}_1 = -L_1 z_1 + z_2 \quad (4.32)$$

$$\dot{z}_2 = -L_2 z_2 - z_1 + z_3 + \omega_2^T \tilde{\theta} \quad (4.33)$$

$$\dot{z}_3 = -L_3 z_3 - z_2 + \omega_3^T \tilde{\theta} - b \left(\bar{\alpha}_3 + y_r^{(3)} \right) \tilde{\lambda} \quad (4.34)$$

A Lyapunov function for this system is:

$$V = \frac{1}{2} z^T z + \frac{1}{2} \tilde{\theta}^T \Gamma^{-1} \tilde{\theta} + \frac{|b|}{2\gamma} \tilde{\lambda}^2 \quad (4.35)$$

Its derivative along the solution of eqs. (4.30-4.34) is:

$$\dot{V} = - \sum_{k=1}^5 L_k z_k^2 \quad (4.36)$$

which proves from the Lasalle-Yoshizawa theorem that global tracking is achieved. The calculations for the error system and the Lyapunov derivation are not shown in this chapter, but are similar to the more complicated calculations for the controller including valve dynamics in section 4.2.2.

4.2.2 Backstepping with Valve Dynamics

In this section valve dynamics is included and it is assumed that all the states, i.e. position and velocity of the mass, load pressure, position and velocity of the valve spool, are measured. Defining the two additional states $(x_4, x_5) = (x_{vn}, \dot{x}_{vn})$

the system can be rewritten as :

$$\begin{aligned}
 \dot{x}_1 &= x_2 \\
 \dot{x}_2 &= x_3 + \varphi_2(x_1, x_2)^T \theta \\
 \dot{x}_3 &= b f(x_3) x_4 + \varphi_3(x_2, x_3)^T \theta \\
 \dot{x}_4 &= x_5 \\
 \dot{x}_5 &= u + \varphi_5(x_4, x_5)^T \theta
 \end{aligned} \tag{4.37}$$

which is in strict-feedback form but contains an unknown virtual control coefficient $b f(x_3)$ which is not constant. A new extension of the tuning function design from [26] is developed below in the special case where $f(x) = \sqrt{\eta_{hmc} F_h / M - x}$:

Coordinate Transformation

$$z_1 = x_1 - y_r \tag{4.38}$$

$$z_2 = x_2 - y_r^{(1)} - \alpha_1 \tag{4.39}$$

$$z_3 = x_3 - y_r^{(2)} - \alpha_2 \tag{4.40}$$

$$z_4 = x_4 - \frac{\hat{\lambda}}{f(x_3)} y_r^{(3)} - \alpha_3 \tag{4.41}$$

$$z_5 = x_5 - \frac{\hat{\lambda}}{f(x_3)} y_r^{(4)} - \alpha_4 \tag{4.42}$$

Regressor

$$\omega_1 = 0 \tag{4.43}$$

$$\omega_2 = \phi_2 \tag{4.44}$$

$$\omega_3 = \phi_3 - \frac{\partial \alpha_2}{\partial x_2} \phi_2 \tag{4.45}$$

$$\omega_4 = -\frac{\partial \alpha_3}{\partial x_2} \phi_2 - \frac{\partial \alpha_3}{\partial x_3} \phi_3 + \frac{\hat{\lambda} y_r^{(3)}}{2 f(x_3)^3} \phi_3 \tag{4.46}$$

$$\omega_5 = \phi_5 - \frac{\partial \alpha_4}{\partial x_2} \phi_2 - \frac{\partial \alpha_4}{\partial x_3} \phi_3 + \frac{\hat{\lambda} y_r^{(4)}}{2 f(x_3)^3} \phi_3 \tag{4.47}$$

Tuning functions for $\hat{\theta}$:

$$\tau_1 = 0 \tag{4.48}$$

$$\tau_2 = \omega_2 z_2 \tag{4.49}$$

$$\tau_3 = \tau_2 + \omega_3 z_3 \tag{4.50}$$

$$\tau_4 = \tau_3 + \omega_4 z_4 \quad (4.51)$$

$$\tau_5 = \tau_4 + \omega_5 z_5 \quad (4.52)$$

Tuning functions for \hat{b} :

$$\pi_3 = z_4 z_3 \quad (4.53)$$

$$\pi_4 = \pi_3 - \frac{\partial \alpha_3}{\partial x_3} f(x_3) x_4 z_4 + \frac{\hat{\lambda} y_r^{(3)}}{2 f(x_3)^2} x_4 z_4 \quad (4.54)$$

$$\pi_5 = \pi_4 - \frac{\partial \alpha_4}{\partial x_3} f(x_3) x_4 z_5 + \frac{\hat{\lambda} y_r^{(4)}}{2 f(x_3)^2} x_4 z_5 \quad (4.55)$$

Stabilizing functions:

$$\alpha_1(x_1, y_r) = \bar{\alpha}_1 \quad (4.56)$$

$$\alpha_2(x_1, x_2, \hat{\theta}, y_r, \dot{y}_r) = \bar{\alpha}_2 \quad (4.57)$$

$$\alpha_3(\bar{x}_3, \hat{\theta}, \bar{y}_r^{(2)}, \hat{\lambda}) = \frac{\hat{\lambda}}{f(x_3)} \bar{\alpha}_3 \quad (4.58)$$

$$\alpha_4(\bar{x}_4, \hat{\theta}, \bar{y}_r^{(3)}, \hat{b}, \hat{\lambda}) = \bar{\alpha}_4 \quad (4.59)$$

$$\alpha_5(\bar{x}_5, \hat{\theta}, \bar{y}_r^{(4)}, \hat{b}, \hat{\lambda}) = \bar{\alpha}_5 \quad (4.60)$$

where $\bar{x}_i = (x_1, \dots, x_i)$ and $\bar{y}_r^{(i)} = (y_r, \dots, y_r^{(i)})$ for all $i = 1, \dots, 5$, and where

$$\bar{\alpha}_1 = -L_1 z_1 \quad (4.61)$$

$$\bar{\alpha}_2 = -z_1 - L_2 z_2 - \omega_2^T \hat{\theta} + \frac{\partial \alpha_1}{\partial x_1} x_2 + \frac{\partial \alpha_1}{\partial y_r} \dot{y}_r \quad (4.62)$$

$$\bar{\alpha}_3 = -z_2 - L_3 z_3 - \omega_3^T \hat{\theta} + \frac{\partial \alpha_2}{\partial \hat{\theta}} \Gamma \tau_3 + \sum_{k=1}^2 \left(\frac{\partial \alpha_2}{\partial x_k} x_{k+1} + \frac{\partial \alpha_2}{\partial y_r^{(k-1)}} y_r^{(k)} \right) \quad (4.63)$$

$$\begin{aligned} \bar{\alpha}_4 = & -\hat{b} f(x_3) z_3 - L_4 z_4 - \omega_4^T \hat{\theta} + \frac{\partial \alpha_3}{\partial \hat{\theta}} \Gamma \tau_4 + \sum_{k=1}^2 \frac{\partial \alpha_3}{\partial x_k} x_{k+1} \\ & + f(x_3) \hat{b} \frac{\partial \alpha_3}{\partial x_3} x_4 + \sum_{k=1}^3 \frac{\partial \alpha_3}{\partial y_r^{(k-1)}} y_r^{(k)} + \left(\frac{y_r^{(3)}}{f(x_3)} + \frac{\partial \alpha_3}{\partial \hat{\lambda}} \right) \dot{\hat{\lambda}} \\ & + \sum_{k=2}^3 \frac{\partial \alpha_{k-1}}{\partial \hat{\theta}} \Gamma \omega_4 z_k - \frac{\hat{\lambda} y_r^{(3)} \hat{b}}{2 f(x_3)^2} x_4 \end{aligned} \quad (4.64)$$

$$\begin{aligned}
\bar{\alpha}_5 = & -z_4 - L_5 z_5 - \omega_5^T \hat{\theta} + \frac{\partial \alpha_4}{\partial \hat{\theta}} \Gamma \tau_5 + \sum_{\substack{k=1 \\ k \neq 3}}^4 \frac{\partial \alpha_4}{\partial x_k} x_{k+1} + f(x_3) \hat{b} \frac{\partial \alpha_4}{\partial x_3} x_4 \\
& + \sum_{k=1}^4 \frac{\partial \alpha_4}{\partial y_r^{(k-1)}} y_r^{(k)} + \left(\frac{y_r^{(4)}}{f(x_3)} + \frac{\partial \alpha_4}{\partial \hat{\lambda}} \right) \dot{\lambda} + \sum_{k=2}^4 \frac{\partial \alpha_{k-1}}{\partial \hat{\theta}} \Gamma \omega_5 z_k \\
& + \frac{\partial \alpha_4}{\partial \hat{b}} \gamma \Pi_5 - \frac{\hat{\lambda} y_r^{(4)} \hat{b}}{2 f(x_3)^2} x_4
\end{aligned} \tag{4.65}$$

Adaptive control law:

$$u = \alpha_5 + \frac{\hat{\lambda}}{f(x_3)} y_r^{(5)} \tag{4.66}$$

Parameter update laws:

$$\dot{\hat{\theta}} = \Gamma \tau_5 \tag{4.67}$$

$$\dot{\hat{b}} = \gamma \pi_5 \tag{4.68}$$

$$\dot{\hat{\lambda}} = -\gamma \text{sign}(b) \left(y_r^{(3)} + \bar{\alpha}_3 \right) z_3 \tag{4.69}$$

Error system: From the design procedure (4.38-4.69), the derivatives of the error variables z_1, \dots, z_5 can be expressed as follows:

$$\dot{z}_1 = \dot{x}_1 - y_r^{(1)} = x_2 - y_r^{(1)} = z_2 + \alpha_1 = -L_1 z_1 + z_2 \tag{4.70}$$

$$\begin{aligned}
\dot{z}_2 = & \dot{x}_2 - y_r^{(2)} - \dot{\alpha}_1 = x_3 + \varphi_2(x_1, x_2)^T \hat{\theta} + \varphi_2(x_1, x_2)^T \tilde{\theta} - y_r^{(2)} - \dot{\alpha}_1 \\
= & z_3 + \varphi_2(x_1, x_2)^T \hat{\theta} + \varphi_2(x_1, x_2)^T \tilde{\theta} - \dot{\alpha}_1 + \alpha_2 \\
= & z_3 + \varphi_2(x_1, x_2)^T \hat{\theta} + \varphi_2(x_1, x_2)^T \tilde{\theta} - \dot{\alpha}_1 - z_1 - L_2 z_2 - \omega_2^T \hat{\theta} \\
& + \frac{\partial \alpha_1}{\partial x_1} x_2 + \frac{\partial \alpha_1}{\partial y_r} \dot{y}_r = -L_2 z_2 - z_1 + z_3 + \omega_2^T \tilde{\theta}
\end{aligned} \tag{4.71}$$

$$\begin{aligned}
\dot{z}_3 &= \dot{x}_3 - y_r^{(3)} - \dot{\alpha}_2 = b f(x_3) x_4 + \varphi_3^T \hat{\theta} + \varphi_3^T \tilde{\theta} - y_r^{(3)} - \dot{\alpha}_2 \\
&= b f(x_3) \left(z_4 + \frac{\hat{\lambda}}{f(x_3)} y_r^{(3)} + \alpha_3 \right) + \varphi_3^T \hat{\theta} + \varphi_3^T \tilde{\theta} - y_r^{(3)} - \dot{\alpha}_2 \\
&= b f(x_3) \left(z_4 + \frac{\hat{\lambda}}{f(x_3)} \bar{\alpha}_3 \right) - b \tilde{\lambda} y_r^{(3)} + \varphi_3^T \hat{\theta} + \varphi_3^T \tilde{\theta} - \dot{\alpha}_2 \\
&= b f(x_3) z_4 - z_2 - L_3 z_3 - \omega_3^T \hat{\theta} + \frac{\partial \alpha_2}{\partial \theta} \Gamma \tau_3 + \sum_{k=1}^2 \left(\frac{\partial \alpha_2}{\partial x_k} x_{k+1} + \frac{\partial \alpha_2}{\partial y_r^{(k-1)}} y_r^{(k)} \right) \\
&\quad - b \tilde{\lambda} \bar{\alpha}_3 - b \tilde{\lambda} y_r^{(3)} + \varphi_3^T \hat{\theta} + \varphi_3^T \tilde{\theta} - \dot{\alpha}_2 \\
&= -L_3 z_3 - z_2 + \hat{b} f(x_3) z_4 + \frac{\partial \alpha_2}{\partial x_2} \phi_2^T \hat{\theta} - b \left(\bar{\alpha}_3 + y_r^{(3)} \right) \tilde{\lambda} + \omega_3^T \tilde{\theta} - \frac{\partial \alpha_2}{\partial x_2} \phi_2^T \hat{\theta} \\
&\quad + \tilde{b} f(x_3) z_4 + \frac{\partial \alpha_2}{\partial \hat{\theta}} \Gamma (\tau_3 - \tau_5) \\
&= -L_3 z_3 - z_2 + \hat{b} f(x_3) z_4 + \sigma_{34} z_4 + \sigma_{35} z_5 + \omega_3^T \tilde{\theta} - b \left(\bar{\alpha}_3 + y_r^{(3)} \right) \tilde{\lambda} \\
&\quad + \tilde{b} f(x_3) z_4
\end{aligned} \tag{4.72}$$

$$\begin{aligned}
\dot{z}_4 &= \dot{x}_4 - \frac{d}{dt} \left(\frac{\hat{\lambda}}{f(x_3)} y_r^{(3)} \right) - \dot{\alpha}_3 \\
&= x_5 - \frac{\dot{\lambda}}{f(x_3)} y_r^{(3)} - \hat{\lambda} \frac{d}{dt} \left(\frac{1}{f(x_3)} \right) y_r^{(3)} - \frac{\hat{\lambda}}{f(x_3)} y_r^{(4)} - \dot{\alpha}_3 \\
&= z_5 + \frac{\hat{\lambda}}{f(x_3)} y_r^{(4)} - \hat{b} f(x_3) z_3 - L_4 z_4 - \omega_4^T \hat{\theta} + \frac{\partial \alpha_3}{\partial \hat{\theta}} \Gamma \tau_4 + \sum_{k=1}^2 \frac{\partial \alpha_3}{\partial x_k} x_{k+1} \\
&\quad + f(x_3) \hat{b} \frac{\partial \alpha_3}{\partial x_3} x_4 + \sum_{k=1}^3 \frac{\partial \alpha_3}{\partial y_r^{(k-1)}} y_r^{(k)} + \left(\frac{y_r^{(3)}}{f(x_3)} + \frac{\partial \alpha_3}{\partial \hat{\lambda}} \right) \dot{\lambda} + \sum_{k=2}^3 \frac{\partial \alpha_{k-1}}{\partial \hat{\theta}} \Gamma \omega_4 z_k \\
&\quad - \frac{\hat{\lambda} y_r^{(3)} \hat{b}}{2 f(x_3)^2} x_4 - \frac{\dot{\lambda}}{f(x_3)} y_r^{(3)} - \hat{\lambda} \frac{d}{dt} \left(\frac{1}{f(x_3)} \right) y_r^{(3)} - \frac{\hat{\lambda}}{f(x_3)} y_r^{(4)} - \dot{\alpha}_3 \\
&= z_5 - \hat{b} z_3 - L_4 z_4 - \omega_4^T \hat{\theta} + \frac{\partial \alpha_3}{\partial \hat{\theta}} \Gamma \tau_4 + \sum_{k=1}^2 \frac{\partial \alpha_3}{\partial x_k} x_{k+1} + f(x_3) \hat{b} \frac{\partial \alpha_3}{\partial x_3} x_4 \\
&\quad + \sum_{k=1}^3 \frac{\partial \alpha_3}{\partial y_r^{(k-1)}} y_r^{(k)} + \frac{\partial \alpha_3}{\partial \hat{\lambda}} \dot{\lambda} + \sum_{k=2}^3 \frac{\partial \alpha_{k-1}}{\partial \hat{\theta}} \Gamma \omega_4 z_k - \frac{\hat{\lambda} y_r^{(3)} \hat{b}}{2 f(x_3)^2} x_4 \\
&\quad - \hat{\lambda} \left(-\frac{b}{2 f(x_3)^2} x_4 - \frac{\phi_3^T \hat{\theta}}{2 f(x_3)^3} - \frac{\phi_3^T \tilde{\theta}}{2 f(x_3)^3} \right) y_r^{(3)} - \dot{\alpha}_3 \\
&= z_5 - \hat{b} z_3 - L_4 z_4 - \omega_4^T \hat{\theta} + \frac{\partial \alpha_3}{\partial \hat{\theta}} \Gamma (\tau_4 - \tau_5) - f(x_3) \tilde{b} \frac{\partial \alpha_3}{\partial x_3} x_4 \\
&\quad + \sum_{k=2}^3 \frac{\partial \alpha_{k-1}}{\partial \hat{\theta}} \Gamma \omega_4 z_k - \hat{\lambda} \left(-\frac{\phi_3^T \hat{\theta}}{2 f(x_3)^3} - \frac{\phi_3^T \tilde{\theta}}{2 f(x_3)^3} \right) y_r^{(3)} - \frac{\partial \alpha_3}{\partial x_3} \phi_3^T \hat{\theta} \\
&\quad - \frac{\partial \alpha_3}{\partial x_3} \phi_3^T \tilde{\theta} - \frac{\partial \alpha_3}{\partial x_2} \phi_2 \hat{\theta} - \frac{\partial \alpha_3}{\partial x_2} \phi_2 \tilde{\theta} + \tilde{b} \frac{\hat{\lambda} y_r^{(3)}}{2 f(x_3)^2} x_4 \\
&= -L_4 z_4 - \sigma_{34} z_3 - \hat{b} z_3 + z_5 + \sigma_{45} z_5 + \omega_4^T \tilde{\theta} \\
&\quad + \tilde{b} \left(\frac{\hat{\lambda} y_r^{(3)}}{2 f(x_3)^2} x_4 - f(x_3) \frac{\partial \alpha_3}{\partial x_3} x_4 \right)
\end{aligned} \tag{4.73}$$

$$\begin{aligned}
\dot{z}_5 &= \dot{x}_5 - \frac{d}{dt} \left(\frac{\hat{\lambda}}{f(x_3)} y_r^{(4)} \right) - \dot{\alpha}_4 \\
&= u + \varphi_5^T \hat{\theta} + \varphi_5^T \tilde{\theta} - \frac{\dot{\lambda}}{f(x_3)} y_r^{(4)} - \hat{\lambda} \frac{d}{dt} \left(\frac{1}{f(x_3)} \right) y_r^{(4)} - \frac{\hat{\lambda}}{f(x_3)} y_r^{(5)} - \dot{\alpha}_4 \\
&= \alpha_5 + \frac{\hat{\lambda}}{f(x_3)} y_r^{(5)} + \varphi_5^T \hat{\theta} + \varphi_5^T \tilde{\theta} - \frac{\dot{\lambda}}{f(x_3)} y_r^{(4)} \\
&\quad - \hat{\lambda} \left(-\frac{b}{2f(x_3)^2} x_4 - \frac{\phi_3^T \hat{\theta}}{2f(x_3)^3} - \frac{\phi_3^T \tilde{\theta}}{2f(x_3)^3} \right) y_r^{(4)} - \frac{\hat{\lambda}}{f(x_3)} y_r^{(5)} - \dot{\alpha}_4 \\
&= -z_4 - L_5 z_5 - \omega_5^T \hat{\theta} + \frac{\partial \alpha_4}{\partial \hat{\theta}} \Gamma \tau_5 + \sum_{\substack{k=1 \\ k \neq 3}}^4 \frac{\partial \alpha_4}{\partial x_k} x_{k+1} + f(x_3) \hat{b} \frac{\partial \alpha_4}{\partial x_3} x_4 \\
&\quad + \sum_{k=1}^4 \frac{\partial \alpha_4}{\partial y_r^{(k-1)}} y_r^{(k)} + \left(\frac{y_r^{(4)}}{f(x_3)} + \frac{\partial \alpha_4}{\partial \hat{\lambda}} \right) \dot{\lambda} + \sum_{k=2}^4 \frac{\partial \alpha_{k-1}}{\partial \hat{\theta}} \Gamma \omega_5 z_k \\
&\quad + \frac{\partial \alpha_4}{\partial \hat{b}} \gamma \Pi_5 - \frac{\hat{\lambda} y_r^{(4)} \hat{b}}{2f(x_3)^2} x_4 + \varphi_5^T \hat{\theta} + \varphi_5^T \tilde{\theta} - \frac{\dot{\lambda}}{f(x_3)} y_r^{(4)} \\
&\quad - \hat{\lambda} \left(-\frac{b}{2f(x_3)^2} x_4 - \frac{\phi_3^T \hat{\theta}}{2f(x_3)^3} - \frac{\phi_3^T \tilde{\theta}}{2f(x_3)^3} \right) y_r^{(4)} - \dot{\alpha}_4 \\
&= -L_5 z_5 - \sigma_{35} z_3 - \sigma_{45} z_4 - z_4 + \omega_5^T \tilde{\theta} + \tilde{b} \left(\frac{\hat{\lambda} y_r^{(4)}}{2f(x_3)^2} x_4 - f(x_3) \frac{\partial \alpha_4}{\partial x_3} x_4 \right)
\end{aligned} \tag{4.74}$$

The resulting error system is:

$$\begin{aligned}
\dot{z}_1 &= -L_1 z_1 + z_2 \\
\dot{z}_2 &= -L_2 z_2 - z_1 + z_3 + \omega_2^T \tilde{\theta} \\
\dot{z}_3 &= -L_3 z_3 - z_2 + \hat{b} f(x_3) z_4 + \sigma_{34} z_4 + \sigma_{35} z_5 + \omega_3^T \tilde{\theta} - b \left(\bar{\alpha}_3 + y_r^{(3)} \right) \tilde{\lambda} \\
&\quad + \tilde{b} f(x_3) z_4 \\
\dot{z}_4 &= -L_4 z_4 - \sigma_{34} z_3 - \hat{b} f(x_3) z_3 + z_5 + \sigma_{55} z_5 + \omega_4^T \tilde{\theta} \\
&\quad + \tilde{b} \left(\frac{\hat{\lambda} y_r^{(3)}}{2f(x_3)^2} x_4 - f(x_3) \frac{\partial \alpha_3}{\partial x_3} x_4 \right) \\
\dot{z}_5 &= -L_5 z_5 - \sigma_{35} z_3 - \sigma_{45} z_4 - z_4 + \omega_5^T \tilde{\theta} + \tilde{b} \left(\frac{\hat{\lambda} y_r^{(4)}}{2f(x_3)^2} x_4 - f(x_3) \frac{\partial \alpha_4}{\partial x_3} x_4 \right)
\end{aligned} \tag{4.75}$$

where σ_{ik} is defined as:

$$\sigma_{34} = -\frac{\partial \alpha_2}{\partial \hat{\theta}} \Gamma \omega_4 \quad (4.76)$$

$$\sigma_{35} = -\frac{\partial \alpha_2}{\partial \hat{\theta}} \Gamma \omega_5 \quad (4.77)$$

$$\sigma_{45} = -\frac{\partial \alpha_3}{\partial \hat{\theta}} \Gamma \omega_5 \quad (4.78)$$

A Lyapunov function for this system is:

$$V = \frac{1}{2} z^T z + \frac{1}{2} \tilde{\theta}^T \Gamma^{-1} \tilde{\theta} + \frac{1}{2\gamma} \tilde{b}^2 + \frac{|b|}{2\gamma} \tilde{\lambda}^2 \quad (4.79)$$

Its derivative along the solutions of (4.75) is computed as:

$$\begin{aligned} \dot{V} &= z_1 (-L_1 z_1 + z_2) + z_2 \left(-L_2 z_2 - z_1 + z_3 + \omega_2^T \tilde{\theta} \right) \\ &\quad + z_3 \left(-L_3 z_3 - z_2 + \hat{b} f(x_3) z_4 + \sigma_{34} z_4 + \sigma_{35} z_5 \right. \\ &\quad \left. + \omega_3^T \tilde{\theta} - b \left(\bar{\alpha}_3 + y_r^{(3)} \right) \tilde{\lambda} + \tilde{b} f(x_3) z_4 \right) \\ &\quad + z_4 \left(-L_4 z_4 - \sigma_{34} z_3 - \hat{b} f(x_3) z_3 + z_5 + \sigma_{45} z_5 \right. \\ &\quad \left. + \omega_4^T \tilde{\theta} + \tilde{b} \left(\frac{\hat{\lambda} y_r^{(3)}}{2 f(x_3)^2} x_4 - f(x_3) \frac{\partial \alpha_3}{\partial x_3} x_4 \right) \right) \\ &\quad + z_5 \left(-L_5 z_5 - \sigma_{35} z_3 - \sigma_{45} z_4 - z_4 \right. \\ &\quad \left. + \omega_5^T \tilde{\theta} + \tilde{b} \left(\frac{\hat{\lambda} y_r^{(4)}}{2 f(x_3)^2} x_4 - f(x_3) \frac{\partial \alpha_4}{\partial x_3} x_4 \right) \right) + \tilde{\theta}^T \Gamma^{-1} \dot{\tilde{\theta}} + \frac{\tilde{b}}{\gamma} \dot{\tilde{b}} + \frac{|b|}{\gamma} \tilde{\lambda} \dot{\tilde{\lambda}} \\ &= - \sum_{k=1}^5 L_k z_k^2 + \left(\frac{\hat{\lambda} y_r^{(3)}}{2 f(x_3)^2} x_4 z_4 - f(x_3) \frac{\partial \alpha_3}{\partial x_3} x_4 z_4 \right. \\ &\quad \left. + \frac{\hat{\lambda} y_r^{(4)}}{2 f(x_3)^2} x_4 z_5 - f(x_3) \frac{\partial \alpha_4}{\partial x_3} x_4 z_5 + f(x_3) z_3 z_4 - \frac{\dot{\tilde{b}}}{\gamma} \right) \tilde{b} \\ &\quad + \left(z_2 \omega_2 + z_3 \omega_3 + z_4 \omega_4 + z_5 \omega_5 - \Gamma^{-1} \dot{\tilde{\theta}} \right)^T \tilde{\theta} - \left(b \left(\bar{\alpha}_3 + y_r^{(3)} \right) z_3 - \frac{|b|}{\gamma} \dot{\tilde{\lambda}} \right) \tilde{\lambda} \end{aligned} \quad (4.80)$$

which yields

$$\dot{V} = - \sum_{k=1}^5 L_k z_k^2 \quad (4.81)$$

Cost	Original	Optimized
α_1	$1 \otimes 2 \oplus$	$1 \otimes 2 \oplus$
α_2	$6 \otimes 9 \oplus$	$6 \otimes 9 \oplus$
α_3	$43 \otimes 67 \oplus$	$27 \otimes 30 \oplus 7 \triangleright$
α_4	$707 \otimes 1085 \oplus$	$128 \otimes 122 \oplus 53 \triangleright$
α_5	$29591 \otimes 44486 \oplus$	$699 \otimes 513 \oplus 222 \triangleright$

Table 4.4: *Cost of calculation in number of multiplication (\otimes), number of additions (\oplus) and number of assignments (\triangleright) for each stabilizing function α_i . Last column is the cost when the calculations are optimized.*

which proves from the Lasalle-Yoshizawa theorem that global tracking is achieved.

Table 4.4 shows the cost of calculations for each stabilizing function at each design step. The computation of the final control law is optimized in order to reduce the cost of calculation and make real-time application possible. Table 4.4 shows that significant reduction in calculation time is possible by optimizing the code.

4.2.2.1 Tracking Performance of Backstepping Controllers

In order to test the robustness of the controller, two models of the plant are implemented. The first one, described in section 4.2.1, is used to design the controller, whereas a second model, more realistic is used to represent the physical system. In this new model the dynamics of the valve is represented by a second order transfer function, the friction in the cylinder is nonlinear and Stribeck and Coulomb effects are modelled. Moreover the compressibility of the fluid is not neglected inside the load and thus the cylinder can accumulate fluid. Finally the uncertain parameters of the new model differ from the ones used in the controller design by up to $\pm 20\%$. The simulation results are given in Figs. 4.13-4.18. Figs. 4.13 and 4.16 show the tracking for sinusoidal and step references. Figs. 4.14 and 4.17 shows the tracking error, and Figs. 4.15 and 4.18 show the actuator (valve) input. For the Figs. 4.13-4.15 the controller gains equal $[L_1, L_2, L_3] = [180, 180, 180]$, while for Figs. 4.16-4.18 the controller gains equal $[L_1, L_2, L_3, L_4, L_5] = [180, 180, 180, 350, 350]$. The reference position and the tracking position are shown with dashed and plain lines, respectively. The model used to develop both the backstepping controllers contain the following uncertainties: $M^* = 0.9 M$, $A^* = 1.1 A$, $k^* = 0.8 k$, $d^* = 0.8 d$, $C_d^* = 0.9 C_d$, $w^* = 1.1 w$, $V_t^* = 0.8 V_t$, $\beta^* = 0.8 \beta$, $\rho^* = 0.9 \rho$, $p^* = 0.9 p$. The *-superscript refers to the model used by the controller.

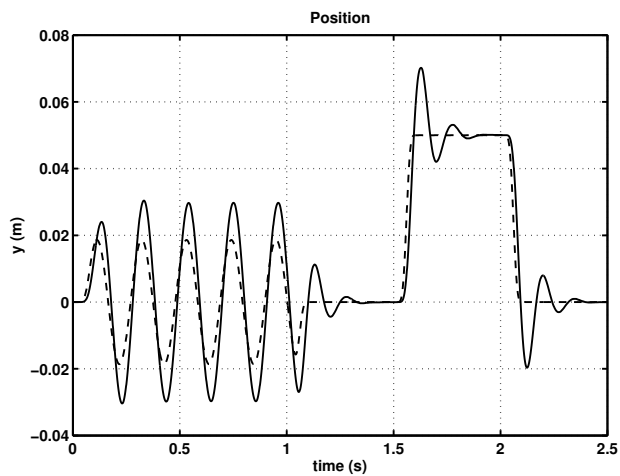


Figure 4.13: Simulated position tracking with the controller of section 4.2.1.

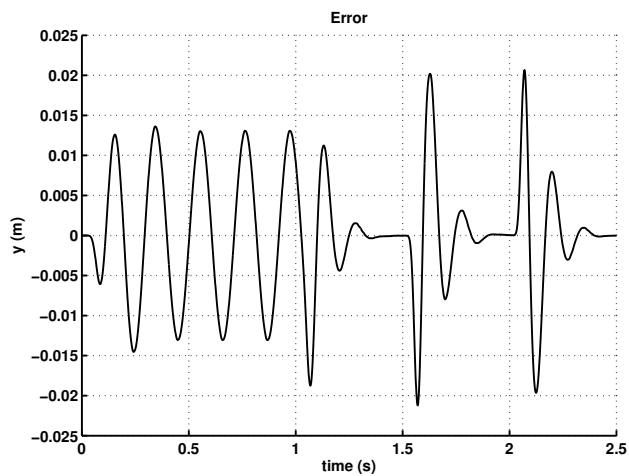


Figure 4.14: Tracking error for Fig. 4.13.

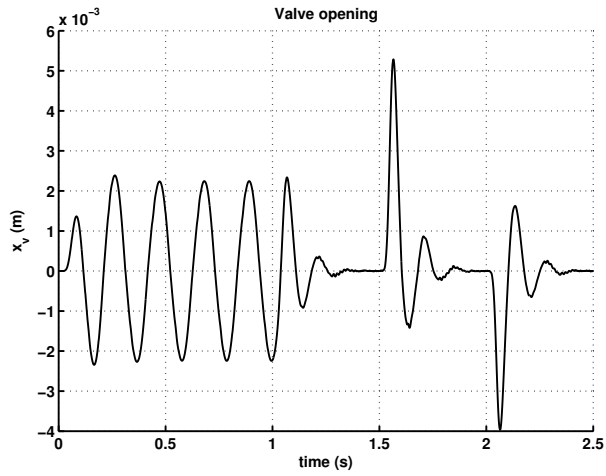


Figure 4.15: Simulated input (valve opening) with the controller of section 4.2.1.

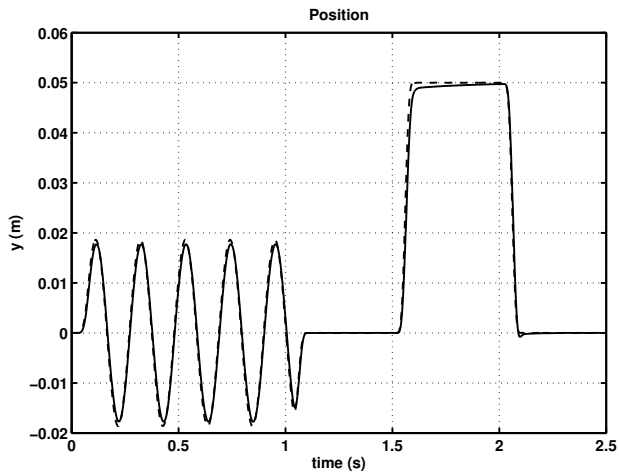


Figure 4.16: Simulated position tracking with the controller of section 4.2.2.

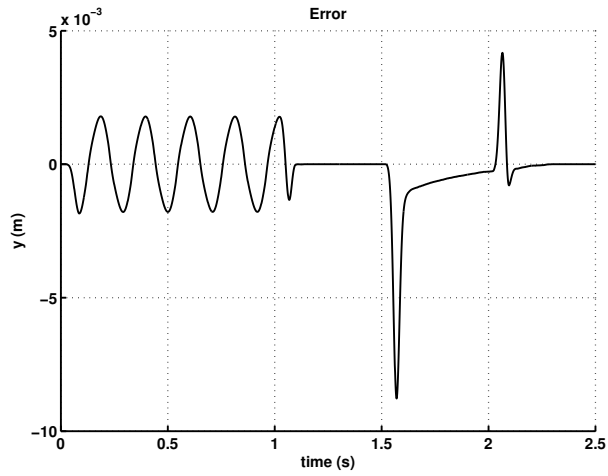


Figure 4.17: Tracking error for Fig. 4.16.

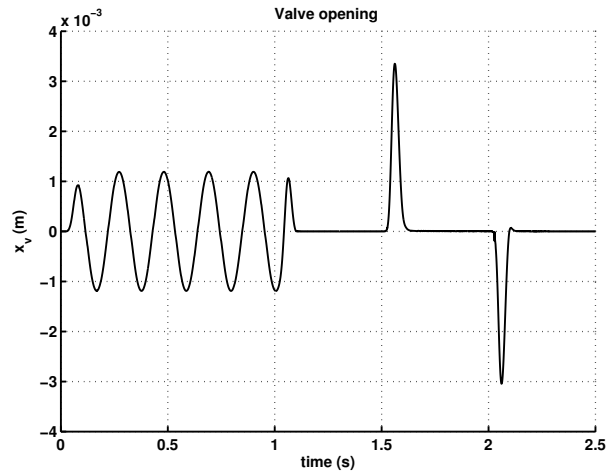


Figure 4.18: Simulated input (valve opening) with the controller of section 4.2.2.

4.2.2.2 Comparison with PI Controller

In [10] the following comparison metrics involving the position error $e(t)$ were defined: Mean Positioning Accuracy (MPA), Absolute Positioning Accuracy (APA), Weighted Position Accuracy (WPA), Saturation Index (SAT), Robustness Index (RI) and Composite Index (CI). The definitions are provided below for completeness.

The MPA is defined as the root mean squared position error obtained for a reference signal, averaged over a time interval $\mathcal{T} = [t_s, t_f]$:

$$MPA = \left(\frac{1}{t_f - t_s} \int_{t_s}^{t_f} e(t)^2 dt \right)^{1/2} \quad (4.82)$$

The APA is defined as the maximum absolute position error over a time interval \mathcal{T} :

$$APA = \max_{t \in \mathcal{T}}(|e|) \quad (4.83)$$

The WPA is defined over a time interval \mathcal{T} in the form:

$$WPA = \left(\frac{1}{t_f - t_s} \int_{t_s}^{t_f} (e(t)^2 + \rho u(t)^2) dt \right)^{1/2} \quad (4.84)$$

where $\rho > 0$ is a control weighting factor and u is the control output. The SAT is defined as the proportion of the respective time interval during which the controller output is saturated:

$$SAT = \frac{t_{sat}}{t_f - t_s} \quad (4.85)$$

The control output is considered saturated when the computed control is $|u(t)| > u_{max}$, where $|u_{max}|$ is the maximum input before saturation. The RI is defined represents the relative error of the MPA for nominal NOM and changed VAR plant parameters over a time interval: \mathcal{T} :

$$RI = \frac{|MPA(NOM, \mathcal{T}) - MPA(VAR, \mathcal{T})|}{MPA(NOM, \mathcal{T})} \quad (4.86)$$

Finally, the CI is defined as the weighted sum of the CI, APA and WPA over a time interval \mathcal{T} :

$$CI = k_1 RI + k_2 APA + WPA \quad (4.87)$$

where k_1 and k_2 are weighting factors.

A PD controller was compared with the other controllers on all these criteria for the transient response ($t_s = 0$) and the steady-state performance ($t_s = 10$),

as well as for a sinusoidal response and for a point-to-point response. For the RI [10] used a 50% reduction in supply pressure.

In this chapter, the criteria APA, MPA and WPA are used to compare a PI controller with two backstepping controllers BS1 and BS2 of sections 4.2.1 and 4.2.2, respectively. A PI controller is used instead of a PD, because the spring in Fig. 2.1 makes the open-loop integrator disappear. The hydraulic system considered in [10] contained an open-loop integrator. Moreover, the following three criteria are not considered in this chapter: SAT, RI and CI. Input saturation for the system in Fig. 2.1 occurs when the valve opening reaches 5mm. This saturation only occurs for the controller in section 4.2.1. The criterion RI is not suited to benchmarking when the nominal error is close to zero, which is the case in this chapter. The CI makes use of the RI, and hence is also not suited in this case. Nevertheless, the robustness of the adaptive backstepping controller can be seen for example in Fig. 4.16, where a 20% initial error in model parameters are introduced.

Similar to the presentation in [10], Figs. 4.19-4.21 contain 4 bars, for simulated results using: a) sinusoidal reference (entire response), b) sinusoidal reference (steady-state response), c) point-to-point reference (entire response), d) point-to-point (steady-state). Fig. 4.19 shows that both backstepping controllers BS1 and BS2 perform better than the PI controller for the APA criterion, where the BS2 controller performs significantly better. For both the MPA and the WPA, the BS1 and the PI controllers give similar performance, while the BS2 performs significantly better as seen in Figs. 4.20-4.21.

Because of the high complexity of these backstepping controllers, their implementation in real-time is not conducted but instead the structure of the controller is modified in order to reduce the complexity and to facilitate real-time experiments. The new design is described in the next section together with simulation and real-time implementation.

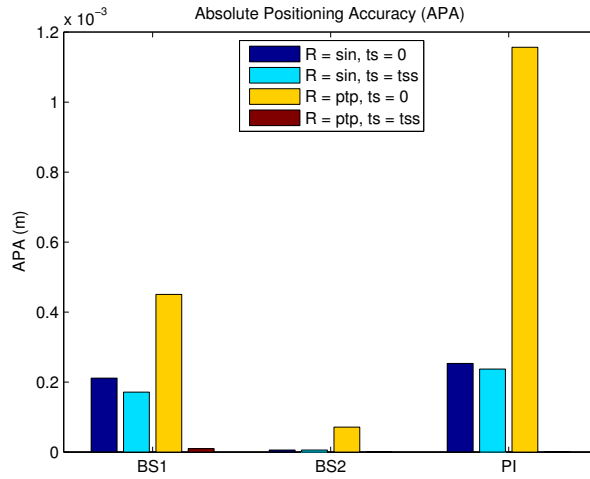


Figure 4.19: Comparison of Absolute Positioning Accuracy.

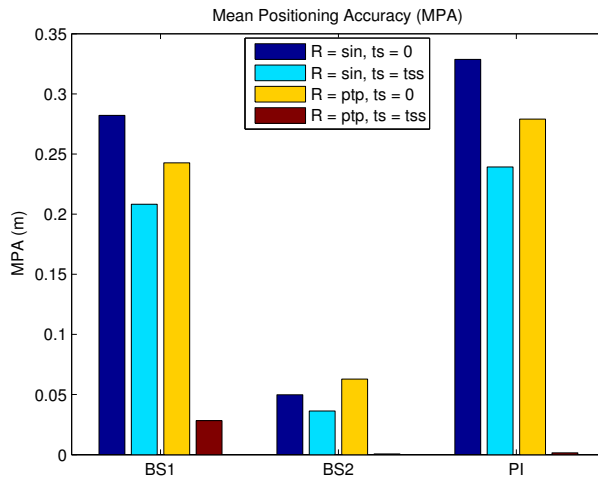


Figure 4.20: Comparison of Mean Positioning Accuracy.

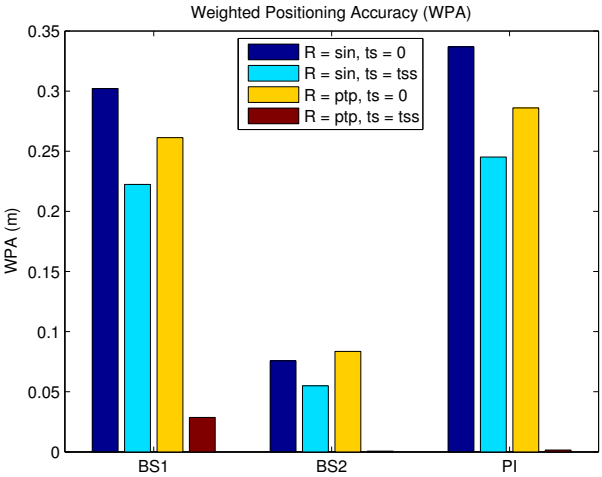


Figure 4.21: Comparison of Weighted Positioning Accuracy.

4.2.3 Backstepping with Valve Dynamics and Dynamic Friction

Another related work is the paper by [37] where the authors consider backstepping control for a pneumatic system using a cascade control structure with feedforward friction compensation. The main differences between [37] and the work presented here is the inner loop controller as well as the type of system (pneumatic vs. hydraulic-mechanical). Instead of using an inner loop containing valve characteristics and approximated inverse valve characteristics as in [37], a PID controller is used in the inner loop together with a backstepping procedure in the outer loop.

One drawback of the paper [13] was the relatively high complexity of the model-based backstepping controller and the difficulty in getting this controller to run fast enough on a real-time system. Hence, in this section, the control structure is re-considered by introducing an internal PID control loop for the pressure in the cylinder. This change reduces the backstepping with three steps compared to the paper [13]. These are shown to be related to: pressure, valve position and velocity, and input voltage. Moreover, it is analysed how the friction model could be extended by including Stribeck effects, Coulomb friction and dynamic phenomena (LuGre model, [11]) and better performance obtained as compared to linear viscous friction models.

Assumptions Besides the assumption that friction can be modeled by a dynamical friction model (LuGre), the three following are also considered: The flow through the leakage between the two cylinder chambers is laminar, i.e. proportional to the load pressure (pressure difference between the two cylinder chambers). The spring and damper in the mechanical part are linear. Other assumptions concerning the valve nonlinearities and valve dynamics are not necessary in the design of the controller thanks to the inner control structure developed in the next section.

4.2.3.1 Controller Design

Trajectory initialization In order to improve the adaptation by making the uncertainty errors smaller and to improve the adaptive system's transient performance, the reference trajectory is initialized, see [27], such that the state variables are zero at time zero and the reference and its derivatives are continuous up to a certain order. In the simulation, the trajectory initialization is done

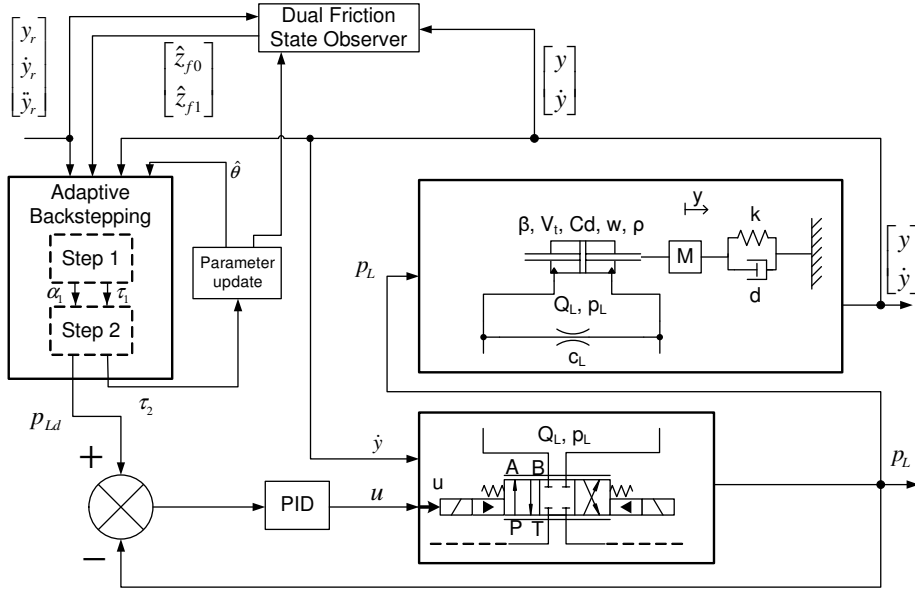


Figure 4.22: Nonlinear controller.

using a Bessel low-pass filter of order 12 with a passband edge frequency of 150 rad/s.

Cascade controller with LuGre friction model compensation The position y and velocity \dot{y} of the mass and the load pressure P_L are measured while the internal state z_f of the friction model, not accessible by measurement, is estimated by a dual observer. One drawback of the controller in [13] is the "explosion of terms" (see [1]), caused by the analytical differentiation of the stabilizing functions from one step to the next. If numerical differentiation is chosen instead, it can produce phase lag between synthetic inputs, requiring higher sampling rate and increases the number of algebraic loops in the simulation. In order to reduce the complexity of the controller and make it suitable for real-time applications the backstepping design is stopped after two steps by considering the load pressure as the input. Using a cascade structure, as shown in Fig.4.22, the load pressure is controlled inside the inner loop by using a PID controller. The external loop ensures a perfect output reference tracking provided the internal loop works perfectly.

The following equations describe the EHSS when p_L is considered as the input:

$$\ddot{y} = -\frac{k}{M}y - \frac{d + \sigma_2 + \sigma_1}{M}\dot{y} + \frac{A}{10M}p_L + \left(\frac{1}{M} \frac{\sigma_1 \sigma_0 |\dot{y}|}{F_c + (F_s - F_c) \exp\left(\frac{-\dot{y}}{v_s}\right)} - \frac{\sigma_0}{M} \right) z_f \quad (4.88)$$

$$\dot{z}_f = \dot{y} - \frac{\sigma_0 |\dot{y}|}{F_c + (F_s - F_c) \exp\left(\frac{-|\dot{y}|}{v_s}\right)} z_f \quad (4.89)$$

Eq.(4.88) is acceleration of the actuator tool and the load mass, where A is the cylinder effective area. If the state variables $[y, \dot{y}]$ are equal to $[x_1, x_2]$ and $p_{Ld} = p_L$, eq.(4.88) can be rewritten as:

$$\dot{x}_1 = x_2 \quad (4.90)$$

$$\dot{x}_2 = \varphi(x_1, x_2)^T \theta + b p_{Ld} + \left(\beta_1 \frac{|x_2|}{g(x_2)} - \beta_0 \right) z_f \quad (4.91)$$

where the control coefficient $b = \frac{A}{10M}$ is unknown, θ is a vector of uncertain parameters:

$$\theta = [\theta_1, \theta_2]^T = \left[-\frac{k}{M}, -\frac{d + \sigma_1 + \sigma_2}{M} \right]^T \quad (4.92)$$

and $\varphi(x_1, x_2)^T = [x_1 \quad x_2]$, $g(x_2) = \frac{F_c}{\sigma_0} + \frac{F_s - F_c}{\sigma_0} \exp\left(\frac{-|x_2|}{v_s}\right)$, $\beta_1 = \frac{\sigma_1}{M}$, and $\beta_0 = \frac{\sigma_0}{M}$. Two observers are used to estimate the internal friction state z_f :

$$\begin{aligned} \left(\beta_1 \frac{|x_2|}{g(x_2)} - \beta_0 \right) z_f &= \frac{|x_2|}{g(x_2)} \left(\beta_1 \tilde{z}_{f1} + \tilde{\beta}_1 \hat{z}_{f1} + \hat{\beta}_1 \hat{z}_{f1} \right) \\ &\quad - \beta_0 \tilde{z}_{f0} - \hat{\beta}_0 \hat{z}_{f0} - \tilde{\beta}_0 \hat{z}_{f0} \end{aligned} \quad (4.93)$$

and

$$\begin{aligned} \dot{\hat{z}}_{f0} &= x_2 - \frac{|x_2|}{g(x_2)} \hat{z}_{f0} + \iota_0 \\ \dot{\hat{z}}_{f1} &= x_2 - \frac{|x_2|}{g(x_2)} \hat{z}_{f1} + \iota_1 \end{aligned}$$

where \hat{z} , \tilde{z} represent the estimate of z and $z - \hat{z}$, respectively. $\iota_{0,1}$ are correction terms that will be found in the next step.

Using the coordinate transformation:

$$z_1 = x_1 - y_r \quad (4.94)$$

$$z_2 = x_2 - \dot{y}_r - \alpha_1 \quad (4.95)$$

and the stabilizing functions:

$$\alpha_1 = -L_1 z_1 \quad (4.96)$$

$$\begin{aligned} \alpha_2 = & -z_1 - L_2 z_2 - \varphi^T \hat{\theta} + \frac{\partial \alpha_1}{\partial x_1} x_2 + \frac{\partial \alpha_1}{\partial y_r} \dot{y}_r \\ & + \hat{\beta}_0 \hat{z}_{f0} - \frac{|x_2|}{g(x_2)} \hat{\beta}_1 \hat{z}_{f1} \end{aligned} \quad (4.97)$$

the adaptive control law is given by:

$$p_{Ld} = \hat{\varrho} (\alpha_2 + \ddot{y}_r) \quad (4.98)$$

where $\hat{\varrho}$ is the estimate of $\varrho = \frac{1}{b}$ computed as

$$\dot{\hat{\varrho}} = -\gamma (\alpha_2 + \ddot{y}_r) z_2 \quad (4.99)$$

and the parameter update laws are:

$$\dot{\hat{\theta}} = \Gamma \varphi z_2 \quad (4.100)$$

$$\dot{\hat{\beta}}_0 = -\gamma_0 \hat{z}_{f0} z_2 \quad (4.101)$$

$$\dot{\hat{\beta}}_1 = \gamma_1 \hat{z}_{f1} \frac{|x_2|}{g(x_2)} z_2 \quad (4.102)$$

$$\iota_0 = -z_2 \quad (4.103)$$

$$\iota_1 = \frac{|x_2|}{g(x_2)} z_2 \quad (4.104)$$

The design procedure in eqs. (4.94)-(4.104) results in the following error system:

$$\dot{z}_1 = \dot{x}_1 - y_r^{(1)} = x_2 - y_r^{(1)} = z_2 + \alpha_1 = -L_1 z_1 + z_2 \quad (4.105)$$

$$\begin{aligned} \dot{z}_2 = & \dot{x}_2 - y_r^{(2)} - \dot{\alpha}_1 = \varphi(x_1, x_2)^T \theta + bu + \left(\beta_1 \frac{|x_2|}{g(x_2)} - \beta_0 \right) z_f - y_r^{(2)} - \dot{\alpha}_1 \\ = & \varphi(x_1, x_2)^T \theta + b \hat{\varrho} \left(-z_1 - L_2 z_2 - \varphi^T \hat{\theta} + \frac{\partial \alpha_1}{\partial x_1} x_2 + \frac{\partial \alpha_1}{\partial y_r} \dot{y}_r + \hat{\beta}_0 \hat{z}_{f0} \right. \\ & \left. - \frac{|x_2|}{g(x_2)} \hat{\beta}_1 \hat{z}_{f1} + \ddot{y}_r \right) + \frac{|x_2|}{g(x_2)} \left(\beta_1 \tilde{z}_{f1} + \tilde{\beta}_1 \hat{z}_{f1} + \hat{\beta}_1 \hat{z}_{f1} \right) - \beta_0 \tilde{z}_{f0} - \hat{\beta}_0 \hat{z}_{f0} \\ & - \tilde{\beta}_0 \hat{z}_{f0} - y_r^{(2)} - \dot{\alpha}_1 \\ = & \varphi(x_1, x_2)^T \tilde{\theta} - z_1 - L_2 z_2 - b \tilde{\varrho} (\alpha_2 + \ddot{y}_r) + \frac{|x_2|}{g(x_2)} \left(\beta_1 \tilde{z}_{f1} + \tilde{\beta}_1 \hat{z}_{f1} \right) \\ & - \beta_0 \tilde{z}_{f0} - \tilde{\beta}_0 \hat{z}_{f0} \end{aligned} \quad (4.106)$$

A Lyapunov function for this system is:

$$V = \frac{1}{2} z^T z + \frac{1}{2} \tilde{\theta}^T \Gamma^{-1} \tilde{\theta} + \frac{b}{2\gamma} \tilde{\varrho}^2 + \frac{\beta_0}{2} \tilde{z}_{f0}^2 + \frac{\beta_1}{2} \tilde{z}_{f1}^2 + \frac{1}{2\gamma_0} \tilde{\beta}_0^2 + \frac{1}{2\gamma_1} \tilde{\beta}_1^2 \quad (4.107)$$

Its derivative along the solution of (4.105-4.106) is:

$$\begin{aligned} \dot{V} &= z_1 (-L_1 z_1 + z_2) + z_2 \left(\varphi(x_1, x_2)^T \tilde{\theta} - z_1 - L_2 z_2 - b \tilde{\varrho} (\alpha_2 + \ddot{y}_r) \right. \\ &\quad \left. + \frac{|x_2|}{g(x_2)} \left(\beta_1 \tilde{z}_{f1} + \tilde{\beta}_1 \hat{z}_{f1} \right) - \beta_0 \tilde{z}_{f0} - \tilde{\beta}_0 \hat{z}_{f0} \right) + \tilde{\theta}^T \Gamma^{-1} \dot{\tilde{\theta}} + \frac{b}{\gamma} \tilde{\varrho} \dot{\tilde{\varrho}} + \beta_0 \tilde{z}_{f0} \dot{\tilde{z}}_{f0} \\ &\quad + \beta_1 \tilde{z}_{f1} \dot{\tilde{z}}_{f1} + \frac{1}{\gamma_0} \tilde{\beta}_0 \dot{\tilde{\beta}}_0 + \frac{1}{\gamma_1} \tilde{\beta}_1 \dot{\tilde{\beta}}_1 \\ &= - \sum_{k=1}^2 L_k z_k^2 + \left(z_2 \varphi - \Gamma^{-1} \dot{\tilde{\theta}} \right)^T \tilde{\theta} - \left(b (\bar{\alpha}_2 + \ddot{y}_r) z_2 + \frac{b}{\gamma} \tilde{\varrho} \right) \tilde{\varrho} \\ &\quad + \left(z_2 \frac{|x_2|}{g(x_2)} \beta_1 + \beta_1 \left(x_2 - \frac{|x_2|}{g(x_2)} (\tilde{z}_{f1} + \hat{z}_{f1}) - \dot{\hat{z}}_{f1} \right) \right) \tilde{z}_{f1} \\ &\quad + \left(z_2 \frac{|x_2|}{g(x_2)} \hat{z}_{f1} - \frac{1}{\gamma_1} \dot{\tilde{\beta}}_1 \right) \tilde{\beta}_1 + \left(-z_2 \hat{z}_{f0} - \frac{1}{\gamma_0} \dot{\tilde{\beta}}_0 \right) \tilde{\beta}_0 \\ &\quad + \left(-z_2 \beta_0 + \beta_0 \left(x_2 - \frac{|x_2|}{g(x_2)} (\tilde{z}_{f0} + \hat{z}_{f0}) - \dot{\hat{z}}_{f0} \right) \right) \tilde{z}_{f0} \\ &= - \sum_{k=1}^5 L_k z_k^2 - \frac{|x_2|}{g(x_2)} (\beta_0 \tilde{z}_{f0}^2 + \beta_1 \tilde{z}_{f1}^2) \end{aligned} \quad (4.108)$$

which proves from the Lasalle-Yoshizawa theorem that global asymptotic tracking is achieved if the error $p_{Ld} - p_L$ inside the inner loop converges to zero.

4.2.3.2 Simulations

In order to demonstrate its robustness the controller is simulated with the EHSS described in [13] where dynamics of the valve spool and nonlinearities in the valve as well as dynamic friction in the cylinder are present. Moreover the uncertain parameters in the plant differ by up to $\pm 20\%$ compared to those used in the controller design. $M^* = 0.9 M$, $A^* = 1.1 A$, $k^* = 0.8 k$, $d^* = 0.8 d$, $\sigma_2^* = 0.9 \sigma_2$, $\sigma_1^* = 1.2 \sigma_1$, $\sigma_0^* = 0.8 \sigma_0$. The *-superscript refers to the model used by the controller.

In order to test the controller at different points of operation, the reference tracking position consists of a 5 Hz sine wave and followed by a sequence of steps between -1 and 10 mm. The controller gains chosen for the backstepping procedure are $L_1 = L_2 = 70$ and the adaptation gains are $\Gamma = \begin{bmatrix} \gamma_0 & 0 \\ 0 & \gamma_1 \end{bmatrix}$, $\gamma_0 = \gamma_1 = 50$. Position of the mass, y , tracking error, z_1 and the input voltage, u are shown in Figs. 4.23, 4.24 and 4.25 respectively, with and without friction compensation in the controller.

Simulations are run using Matlab/Simulink with a fixed step solver of order 4 (Runge-Kutta) and 5 ms step size which is suitable for real-time implementation (for instance using National Instrument CompactRio controller, Matlab XPC Target or Siemens 300-series PLC's).

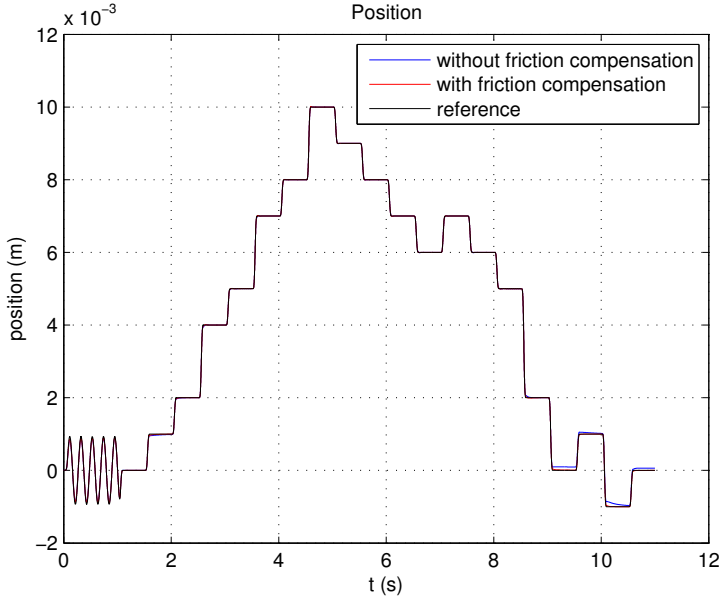


Figure 4.23: Position y . Black, blue and red line for the reference position, the position given by the controller without and with friction compensation respectively. $L_1 = L_2 = 70$.

Simulation results in Fig. 4.24 show that the tracking error is significantly decreased with friction compensation when the operating point is close to the zero position, i.e. when the load pressure is low. It happens in the simulation at time $t = 9$ to $t = 11$ s.

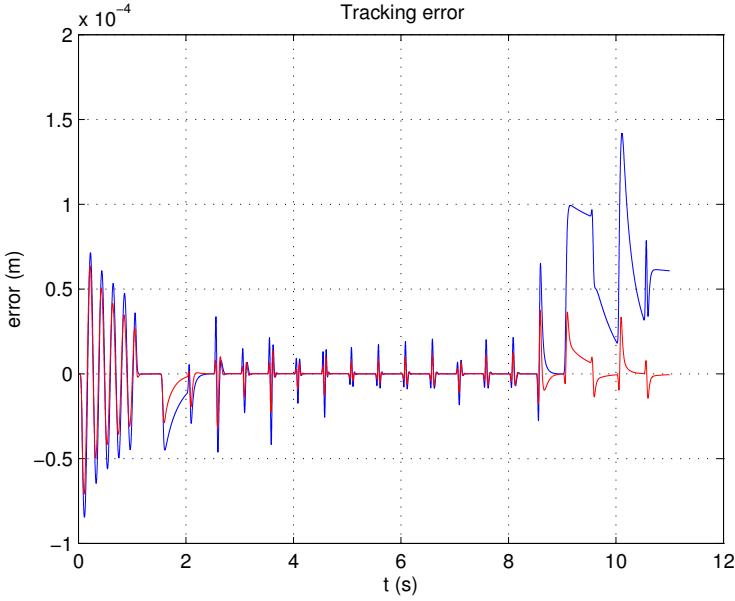


Figure 4.24: Tracking error. Blue=without friction compensation, Red=with friction compensation. $L_1 = L_2 = 70$.

4.2.3.3 Comparison with Full Backstepping

In this section the cascade controller with friction compensation developed in section 4.2.3.1 called CASC and the controller developed in [13] called BS2 are compared, using the same input position reference as the previous section and same gains for the controllers. The results are shown in Figs. 4.26 and 4.27 for a similar input level ($\pm 2V$).

The Mean Positioning Accuracy (MPA) and the Absolute Positioning Accuracy (APA) as defined in [10] are shown in Table 4.5.

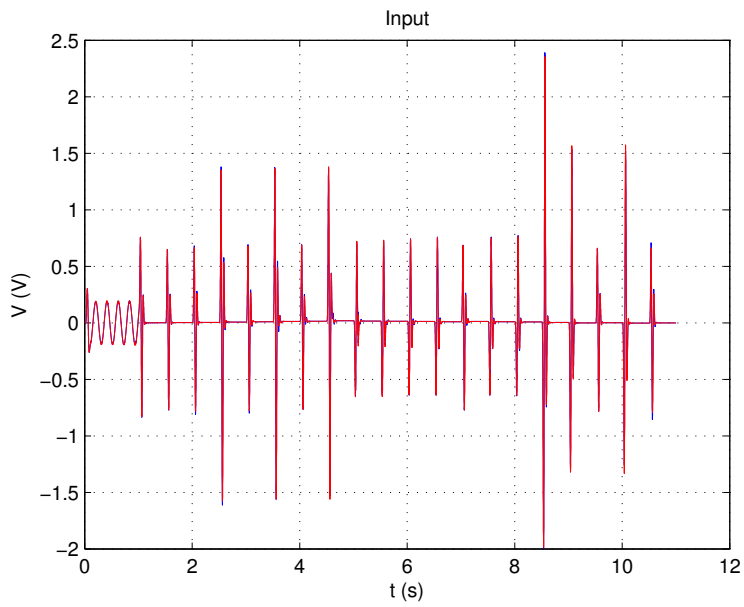


Figure 4.25: Input voltage. Blue=without friction compensation, Red=with friction compensation. $L_1 = L_2 = 70$.

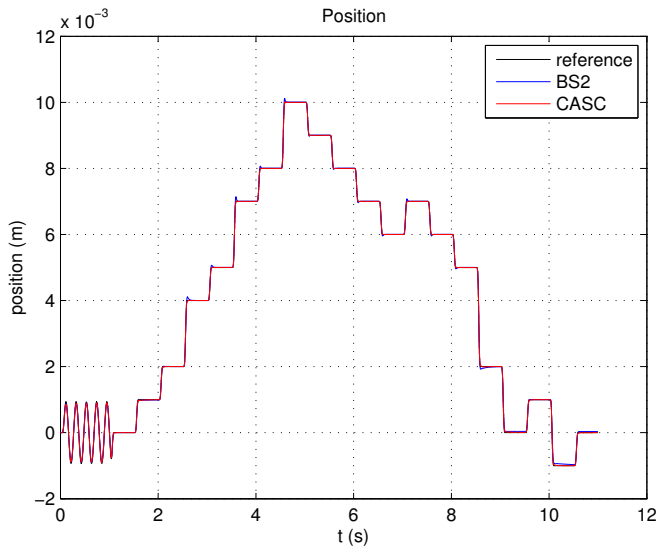


Figure 4.26: Position y . Black, blue and red line for the reference position, the position given by the controller BS2 and CASC respectively.

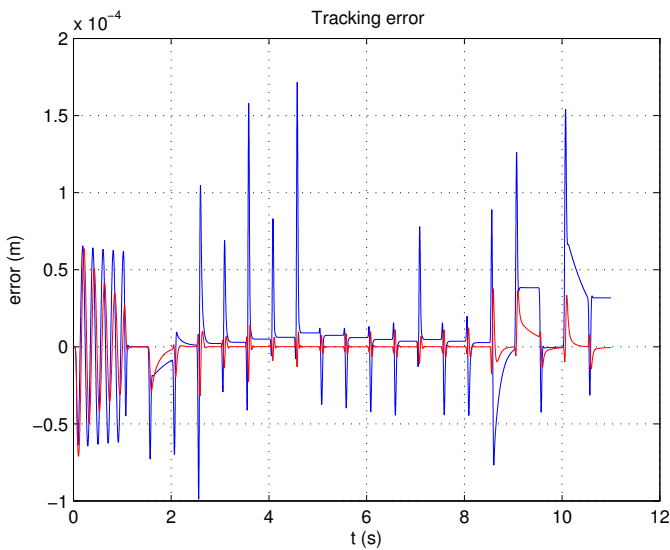


Figure 4.27: Tracking error y . Blue and red line for the controller BS2 and CASC respectively.

Controller Type	MPA	APA
BS2 (from $t = 0$ to $t = 9$)	$7.88 \cdot 10^{-4}$	$1.71 \cdot 10^{-4}$
BS2 (from $t = 9$ to $t = 11$)	$2.10 \cdot 10^{-3}$	$1.59 \cdot 10^{-4}$
CASC (from $t = 0$ to $t = 9$)	$3.90 \cdot 10^{-4}$	$7.10 \cdot 10^{-5}$
CASC (from $t = 9$ to $t = 11$)	$8.77 \cdot 10^{-4}$	$3.64 \cdot 10^{-5}$
Improvement from $t = 0$ to $t = 9$	2.02	2.41
Improvement from $t = 9$ to $t = 11$	2.39	4.37

Table 4.5: Comparison of tracking performance between CASC and BS2 controller.

The new controller CASC performs significantly better (more than a factor of 2 on both criteria), and especially for the APA improvement for positions close to zero where the load pressure is low, as seen in Fig.4.27 (between $t = 9$ and $t = 11$). Moreover, the number of floating point operations when using controller CASC is considerably reduced compared to the BS2 and more suitable for real-time implementation, see Table 4.6.

Controller Type	Costs
BS2	$699 \otimes 513 \oplus 222 \triangleright$
CASC	$16 \otimes 15 \oplus 4 \triangleright$

Table 4.6: Cost of BS2 and CASC optimised calculations in number of multiplication and division (\otimes), number of additions (\oplus) and number of assignments (\triangleright) for each control law.

4.3 Experiments

In this section the linear controllers as well as the adaptive nonlinear controller based on backstepping techniques and cascade structure are implemented in real-time on the test bed presented in chapter 2. The tracking performances for each controlled EHSS are thereafter analysed using the mean positioning accuracy and the absolute positioning accuracy metrics. The experiments are conducted with a hydraulic fluid temperature stabilised around 30°C and without load. Real-time implementation is realised using Matlab XPC Target with 1ms step size. Position tracking and the corresponding tracking error are shown in figs.4.28 and 4.29 for the same position reference used in simulation fig.4.26. The same experiment is repeated for the controlled EHSS with four different controllers, i.e. the proportional (K_P), lag (K_L), H_∞ (K_I) and backstepping (CASC) controllers designed previously.

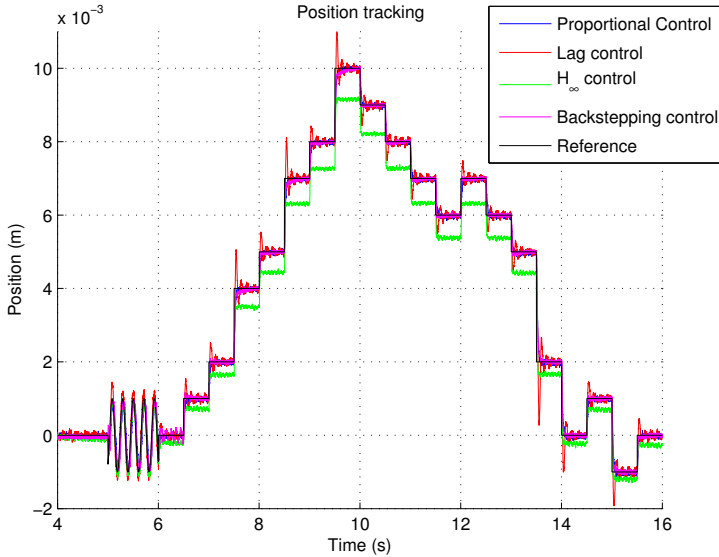


Figure 4.28: Position tracking using linear controller (proportional = blue, lag compensator = red, H_∞ = green) and nonlinear backstepping control (magenta). Reference position is the black line.

All controllers successfully stabilise the system and the mass position is able to follow in a certain extent the reference, with large steady-state error with H_∞ control and large overshoot with lag control, as shown previously from simulation. Next, the performances when the reference is a sine wave of frequency 30 rad/s and amplitude 1mm are investigated and position tracking together with error tracking are shown during one period for time interval $\mathcal{T} = [5.6, 5.85]$ in figs. 4.30 and 4.31 respectively.

At this frequency, the closed-loop system with lag control gives the smallest tracking error since the phase shift is reduced compared to the other controllers. However, at higher frequencies, the phase shift for the system with lag control would drop quickly to -90° and proportional control might give better performances. MPA and APA metrics for the sine wave reference signal over the time interval $\mathcal{T} = [5.1, 5.9]$ are given in table 4.7. These results show that for a sine wave reference signal of low frequency and low amplitude, the nonlinear backstepping controller does not perform better than linear controllers. Finally the tracking performances are analysed when the reference signal is a step of amplitude 1 mm. Position and error tracking are shown in figs. 4.32 and 4.33 respectively.

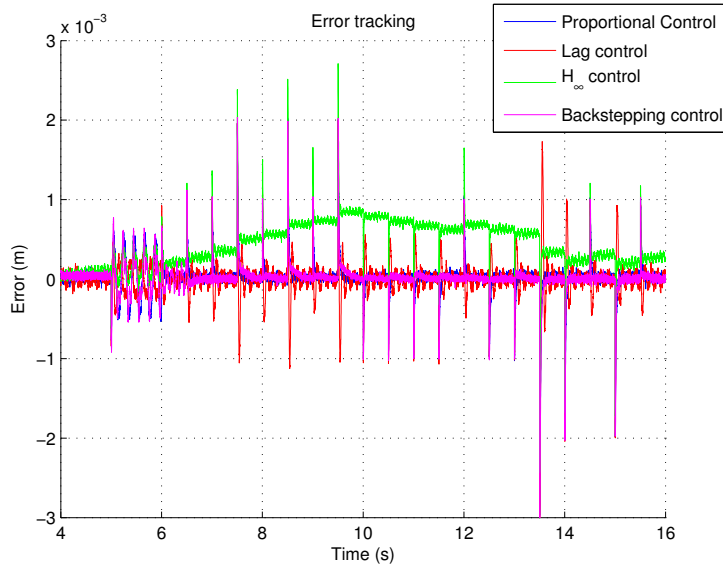


Figure 4.29: Position errors.

Whereas lag control leads the feedback system to a 40% overshoot and H_{∞} control leads to a 30% steady-state error, the backstepping controller with friction compensation gives the best performances in terms of mean positioning accuracy, as shown also in table 4.8.



Figure 4.30: Position tracking using linear controller (proportional = blue, lag compensator = red, H_{∞} = green) and nonlinear backstepping control (magenta). Reference position is the black line.

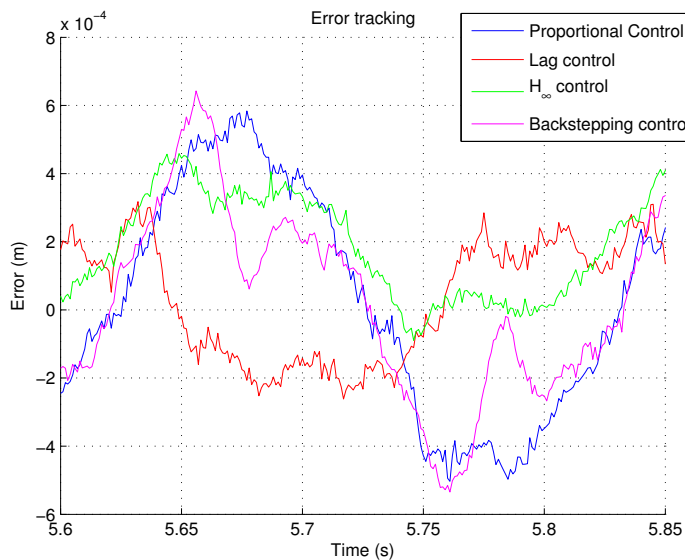


Figure 4.31: Position errors.

Controller Type	MPA	APA
K_P	$11.2 \cdot 10^{-3}$	$5.9 \cdot 10^{-4}$
K_L	$5.6 \cdot 10^{-3}$	$3.8 \cdot 10^{-4}$
K_I	$7.3 \cdot 10^{-3}$	$4.9 \cdot 10^{-4}$
$CASC$	$9.1 \cdot 10^{-3}$	$6.4 \cdot 10^{-4}$

Table 4.7: Comparison of tracking performance between proportional, lag and backstepping controllers, K_P , K_L , K_I and $CASC$ respectively, when the tracking reference is a sine wave signal of amplitude 1 mm and frequency 30 rad/s (from $t = 5.1s$ to $t = 5.9s$)

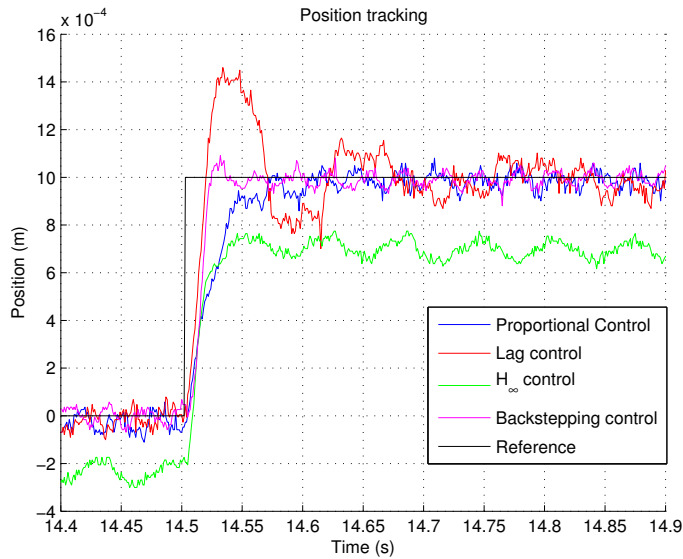


Figure 4.32: Position tracking using linear controller (proportional = blue, lag compensator = red, H_∞ = green) and nonlinear backstepping control (magenta). Reference position is the black line.

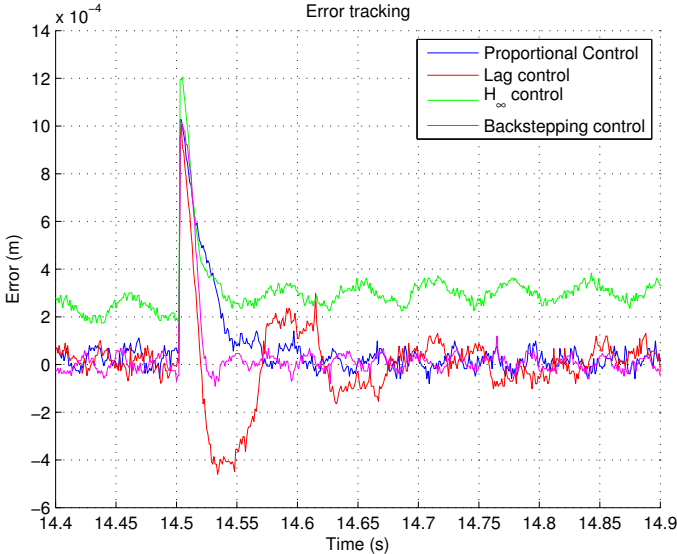


Figure 4.33: Position errors.

Controller Type	MPA	APA
K_P	$4.6 \cdot 10^{-3}$	$1.0 \cdot 10^{-3}$
K_L	$7.0 \cdot 10^{-3}$	$1.0 \cdot 10^{-3}$
K_I	$9.3 \cdot 10^{-3}$	$1.2 \cdot 10^{-3}$
$CASC$	$3.7 \cdot 10^{-3}$	$1.0 \cdot 10^{-3}$

Table 4.8: Comparison of tracking performance between proportional, lag and backstepping controllers, K_P , K_L , K_I and $CASC$ respectively, when the tracking reference is a negative step of amplitude 2mm followed by a positive step of amplitude 1mm (from $t = 14.1s$ to $t = 15s$)

4.4 Active Fault-Tolerant Control

Hydraulic manipulators have greatly improved safety and work conditions for operators. However, faults in hydraulic systems happen and a proper design of control system must be considered in order to avoid a break-down of the system or catastrophic failures.

Fault-tolerant control is a new area of automatic control and is particularly suited for applications where safety is of high priority or for applications where the cost of break-down, time to repair and intervention is high. Systematic methods for fault handling were developed in [6], and its application to EHSS has received increased attention in the last decade. Two cases can be distinguished:

The first case is passive fault-tolerant control (FTC) which can tolerate changes and can satisfy the requirements for a certain class of fault without the need to identify or diagnose the faults. For this purpose, robust or adaptive controllers are used. Passive FTC is best suited for slowly varying parameters and not for abrupt changes. Application to EHSS have been shown in [32], [21] or [22] where the controller used are based on quantitative feedback theory (QFT), or in [40] by using robust H_∞ control. QFT will not be dealt further in detail in this dissertation.

The second case is active FTC where information obtained from fault diagnosis is considered in controller redesign [33]. Application in EHSS are found in [17], [12] and [5]. Different actions can be taken after a fault is diagnosed: the nominal controller is augmented by a compensation controller in [17], the backstepping design is modified in [12] in order to include an additional adaptation term and adaptation law to compensate for the fault and a bumpless switch to a predetermined PID controller is realised in [5]. The faults which have been considered in the cited papers were internal leakage, fault in servo valve, in supply pressure, fault due to contamination and pressure sensor offset, detected by residual generation from parity equation and fuzzy-logic in [5], backstepping update laws in [12] and robust observer and adaptive robust state reconstruction in [17]. The nonlinearity in orifice flow and in nonsymmetric hydraulic cylinder were considered but not the nonlinearity in friction which in the present case is dominant.

Because of its adaptivity, it was shown in this chapter that nonlinear backstepping control can tolerate small faults in the uncertain parameters. However, in the case of the loss of one of the pressure sensor, backstepping control as designed previously is no longer operational. In this section active FTC with fault detection and identification (FDI) is designed, where the possible fault considered are due to leakage flow in the cylinder or valve, increase of friction in the

cylinder and fault in one of the pressure sensor. In this last case the controller is reconfigured and only the position measurement is used in order to track a position reference y_{ref} . The structure of the active FTC is shown in fig.4.34 where r_1 , r_2 are two residuals generated from the position and load pressure measurements, m_1 and m_2 respectively and the input signal u . The signals d_1 and d_2 are boolean and are one if the threshold for the test on r_1 , r_2 respectively is reached. The signals f_{g1} , f_{g2} and f_{g3} are three groups of distinct faults.

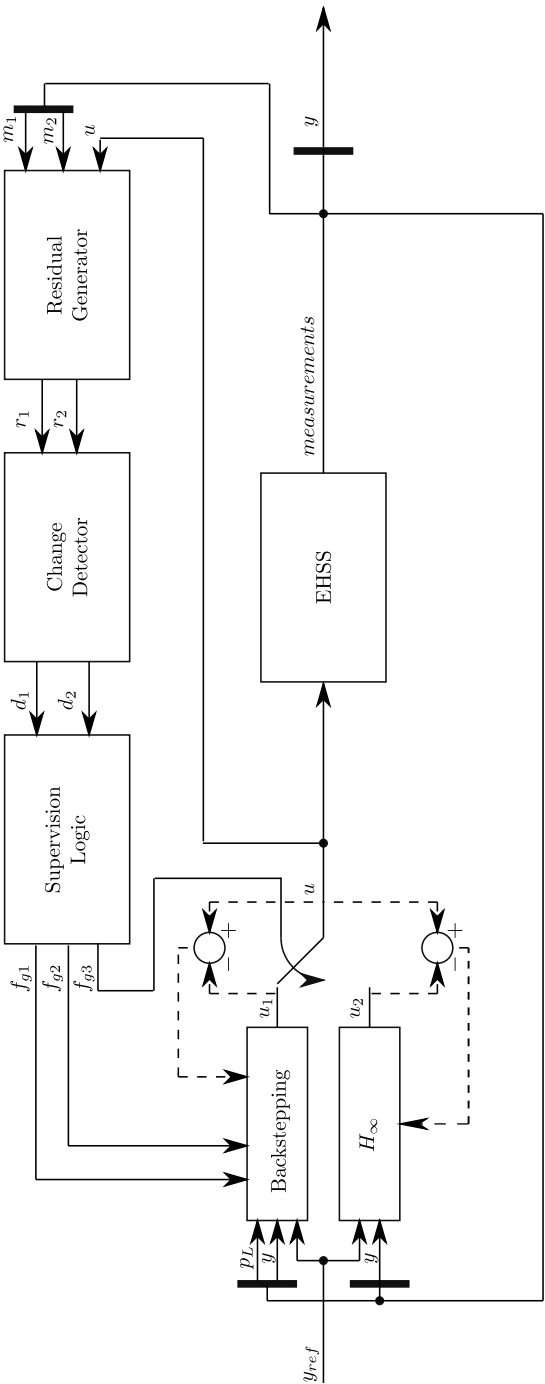


Figure 4.34: Active fault-tolerant control structure with control reconfiguration for an EHSS.

4.4.1 Fault Detection and Isolation

The two residuals r_1 and r_2 are generated using eqs. (3.17) and (3.18). The statistical hypothesis test developed in the previous chapter when the EHSS is in steady-state is no longer valid in the general case with varying input and new tests need hence to be designed. In this section, for the demonstration of FTC design with varying inputs, the varying input type is limited to periodic signals with frequencies higher than 1 Hz. In this special case, it can be shown from eqs. (3.17) and (3.18) that a fault in internal leakage or friction adds a periodic signal of zero mean to the residuals. Thus, the test used in this section consists of a running RMS value of the residuals with moving window length equal to the maximum period of the input signal followed by a threshold based test (a relay). The outputs of the test are the signals d_1 and d_2 as shown in fig. 4.34. Experimental results of the signals r_1 , r_2 , and of the signals d_1 , d_2 before the relay are shown later in section 4.4.4.

The way the constraints (eqs. (3.1)-(3.6)) and measurements (eqs. (3.7) and (3.8)) enter into the two parity relations (residuals r_1 and r_2) is as follows:

$$\begin{pmatrix} r_1 \\ r_2 \end{pmatrix} \leftarrow \begin{pmatrix} m_1 & m_2 & c_1 & c_2 & c_3 & c_4 & c_5 & c_6 \\ 1 & 1 & 1 & 0 & 1 & 0 & 0 & 0 \\ 1 & 1 & 0 & 1 & 0 & 1 & 1 & 1 \end{pmatrix} \quad (4.109)$$

Since two residuals are available, three groups of fault can be isolated. The first group, f_{g1} , with signature $r_1 \neq 0, r_2 = 0$ includes faults in the orifice flow equation c_1 or the mass balance equation c_3 . Possible fault in this group are leakage flow in the cylinder, change of the hydraulic fluid properties due to contamination or change in temperature. The second group, f_{g2} , with signature $r_1 = 0, r_2 \neq 0$ includes the force balance equation c_2 and the constraints relative to the friction model c_4 , c_5 and c_6 . Possible faults are due to the friction in the cylinder or a fault related to the load. The last group, f_{g3} , with signature $r_1 \neq 0, r_2 \neq 0$ includes the measurements m_1 and m_2 where possible faults are due to sensors. The supervision logic block in fig. 4.34 can be designed as shown in fig. 4.35 using AND and NOT gates.

4.4.2 Controller Design

For the first two groups of faults the structure of the controller does not need to be changed, thus passive fault-tolerant control can be realised by designing robust and adaptive controllers. The controller designed in section 4.2 can hence recover from a fault related to leakage in the cylinder, hydraulic fluid contamination, friction or load. However, since the adaptation law might be too

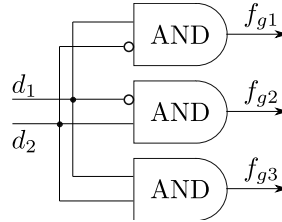


Figure 4.35: Supervision logic for three fault group diagnosis.

slow for the parameters to converge to the values when a fault is present, active fault-tolerant control is realised by changing the values of the backstepping controller parameters once a fault in leakage or friction is diagnosed. In the case of a faulty pressure measurement, since the backstepping controller needs the pressure feedback in order to be operational, any fault in one of the two pressure sensors would lead the system to a break-down.

4.4.3 Controller Reconfiguration

In order to avoid the system to stop, the structure of the controller needs to be changed, if one of the pressure sensor fails and only the position measurement is available. Since high performance is no longer a priority in this case, one of the linear controllers designed in section 4.1 can be used until the sensor is fixed or replaced. A seamless transition between the two controllers needs to be designed. If a H_∞ controller is chosen to replace the nonlinear controller, the transition can be realised using progressive fault accommodation or anti-windup mechanism as in [6] where the controller states are correctly initialised. The structure of such a reconfiguration is shown in fig. 4.34. Experimental results are presented in the next subsection with fault diagnosis of leakage, friction, and pressure sensor loss, together with controller reconfiguration from nonlinear backstepping control to proportional control.

4.4.4 Experiments

An experiment is run on the test bed presented before, without load. The goal of the experiment is to demonstrate the ability of the EHSS to perform position tracking when faults in leakage, friction and pressure sensor occur by using active FTC as shown in fig. 4.34. The reference position is a sine wave of frequency 5 rad/s and amplitude 1 cm. A fault in internal leakage is introduced

after 13.8 s until time is 20 s by opening a manual valve between the cylinder chambers. The calibrated leakage flow through this opening at 80 bar is 2 l/min. At time $t = 25.8$ s, a force of approximately 10N is applied against the mass in only positive direction, until time $t = 30.7$ s. Finally the pressure sensor in cylinder chamber A is disconnected during time interval $[40.3\text{s} - 44.0\text{s}]$. The measurements and input values are shown in fig. 4.36.

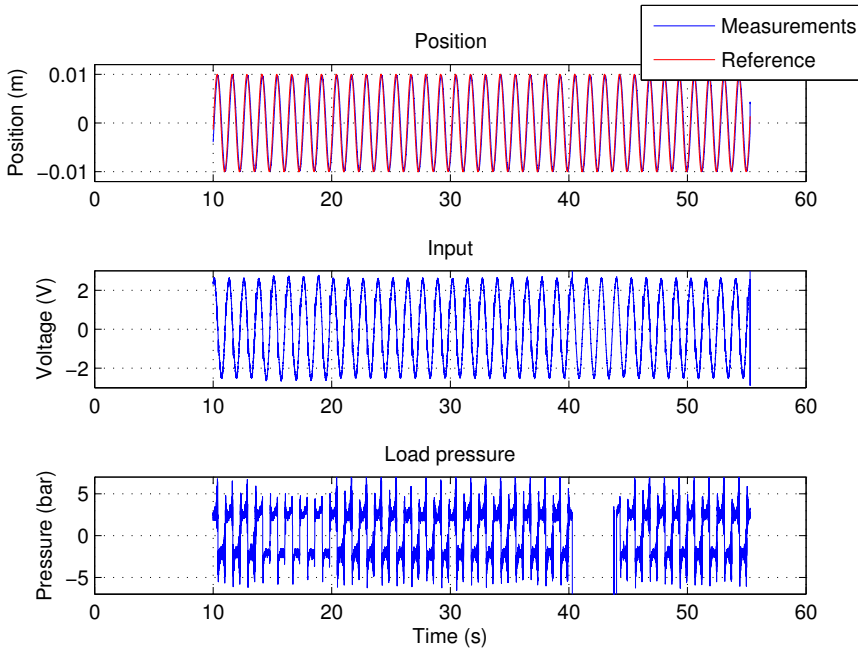
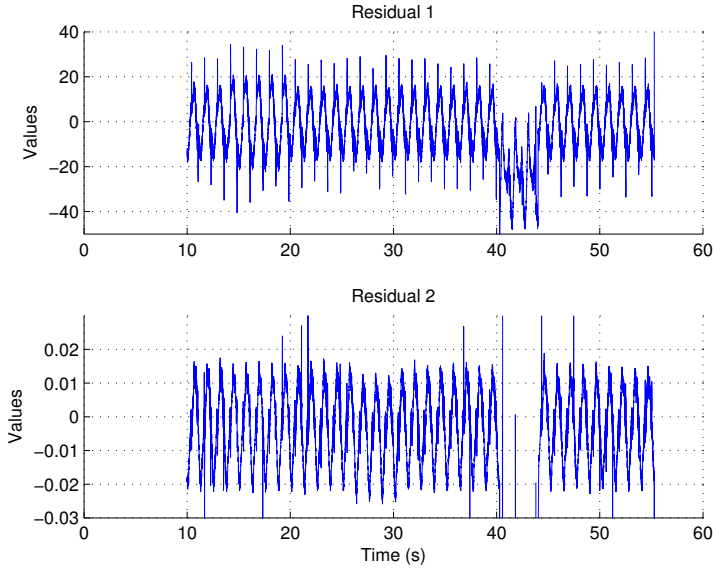


Figure 4.36: Position and load pressure measurements, input signals for position tracking of a 5 rad/s sine wave with successive faults in leakage, friction and pressure sensor during time interval $[13.8\text{s} - 20.0\text{s}]$, $[25.8\text{s} - 30.7\text{s}]$, and $[40.3\text{s} - 44.0\text{s}]$ respectively.

The measurements in fig. 4.36 show that the controlled system with active fault-tolerant control is able to follow the reference with high accuracy even with presence of one of the three faults considered. Moreover, the faults are not easily detectable from measurements only.

Fig. 4.37 shows the generated residuals r_1 and r_2 . It is observed that fault in leakage increases the magnitude of residual r_1 , one way additional force (which represent fault in friction) results in a small decrease in residual r_2 , whereas fault in pressure sensor is clearly visible in both residuals.

Figure 4.37: Residuals r_1 and r_2 .

Using a running RMS value of the residual with a moving and overlapping window for residual r_1 and a moving average value for residual r_2 , the processed residual data are shown in fig. 4.38. The changes are shown to be detectable using thresholds for fault detection and fault reversion. The value of these thresholds were tuned from the experiment directly in order to obtain satisfactory false alarm rate and detection time. The dependence of these thresholds with the false alarm rate is left for future studies.

Finally the faults are diagnosed and shown in fig. 4.39 using supervision logic. The time to detect is approximately 0.5 s for leakage related fault and 1s for friction related fault. The time to detect pressure sensor loss is within the range of 20 ms and the time to revert from sensor loss is approximately 60 ms. During these detection times the controller switches seamlessly from nonlinear backstepping control to proportional control, with a peak in input signal limited by saturation.

Remark Since the time to detect a change in residual r_2 is longer than the time to detect a change in residual r_1 , false alarms occur first in leakage fault diagnosis when the sensor fault is activated, and second in friction fault diagnosis when the sensor fault is deactivated as shown in fig. 4.39.

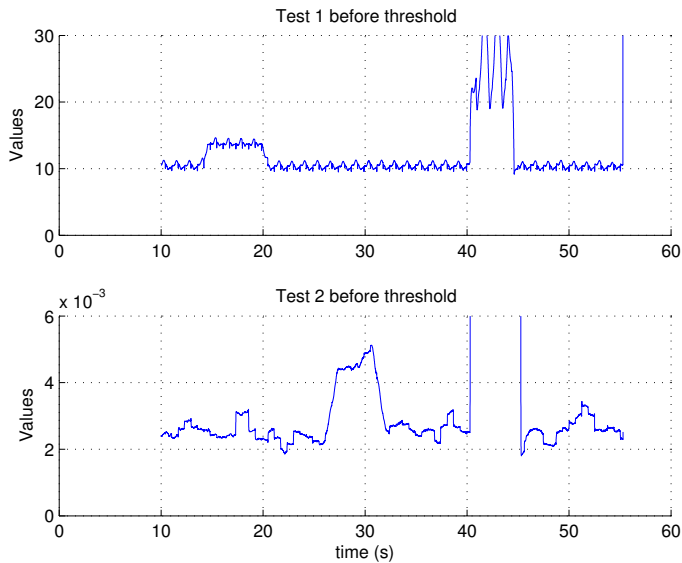


Figure 4.38: Values of the test run for residuals before decision making based on threshold.

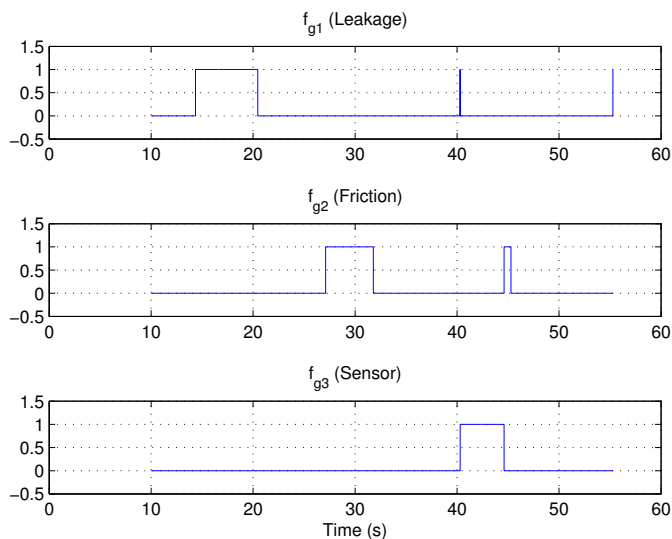


Figure 4.39: Diagnosed faults in group 1, 2 or 3 related to leakage, friction and sensor respectively, after supervision logic.

4.5 Summary and Discussion

In this chapter adaptive nonlinear control for electro hydraulic servo system was designed and implemented in a real-time environment on the test bed described in chapter 2 which exhibits nonlinearities and model uncertainties. First a review of classical linear control methods including proportional, lag and H_∞ control was used to characterise the performances which can be achieved using simple and ubiquitous compensators.

Second, an adaptive backstepping controller considering valve dynamics has been developed and the performance has been compared with three different criteria to a simple PI controller by simulation. All three criteria show that the adaptive backstepping controller taking valve dynamics into account performs significantly better than both the PI controller and a reduced version of the backstepping controller without taking valve dynamics into account.

Third, the complexity of the adaptive backstepping controller has been reduced by a factor of 50 by developing a cascade structure where the desired load pressure is considered as the output of the adaptive backstepping controller. By including a dynamic friction compensation in the new design the position tracking performances of the adaptive controller have further been increased compared with the similar controller without the cascade structure and the dynamic friction model. Besides, the new controller is suitable for real-time implementation and experimental results have demonstrated the increased performances over linear controllers in term of positioning accuracy for small amplitude step changes.

Finally, by combining the techniques of fault detection and isolation developed in the previous chapter with those of adaptive nonlinear control developed in this chapter, an active fault-tolerant controller has been successfully implemented on the test bed described in chapter 2. Online fault diagnosis for faults related either to internal leakage or to friction in the hydraulic cylinder, or to pressure sensors has been demonstrated with active controller parameter update for the first two cases and active controller reconfiguration in the last case where one of the two pressure sensor fails.

Conclusions and Further Research

5.1 Introduction

This chapter reviews the major results and contributions presented in the thesis and introduces several topics for further research. Motivated by the work realised and the results achieved in the previous chapters, the topics discussed in this chapter are: 1) the behaviour and modelling of friction and orifice flows in electro hydraulic servo system (EHSS), 2) the prognosis of fault in EHSS, 3) real-time implementation of adaptive nonlinear backstepping control in EHSS, 4) design of active fault-tolerant control for large EHSS. For each of these topics, the major conclusions are drawn and then discussed leading to recommendations for the modelling and control design of EHSS. Finally, in the last section of this chapter, several topics for further research are suggested which raise from the work presented in the thesis.

5.2 Major Conclusions, Discussions and Recommendations

The main contributions of the thesis are the developments of tools for designing an active fault-tolerant controller for EHSS. Results in three different areas have been achieved. The first main contribution is the identification of the uncertain and nonlinear system using a high fidelity model of the EHSS. 1) A new model for friction has been developed which explains the main static and dynamic behaviour of the force inside the hydraulic cylinder, including film thickness formation and the increase of Stribeck friction related to the sum of the chamber pressures in the cylinder. 2) A new model has been developed which takes into account the leakage flows inside the servo valve as well as openings deadbands and asymmetries. The motivation behind this new model for the servo valve is to obtain simulated values of the pressures close to the measured ones and to reproduce the important variation of the sum of the chamber pressures. Using a model with symmetric valve and actuator and making the assumption of equal flow coming in and out of the actuator results in a constant sum of the chamber pressures equal to the supply pressure. By contrast, experimental results show a variation up to +50% above the supply pressure which is well represented by the new model. All parameters have been estimated using the new models and the experimental data registered with one position and two pressure sensors.

The second main contribution of the thesis is the development of fault diagnosis techniques for EHSS. A fault detector was designed and implemented on a test bed for a simple EHSS. Experimental results showed the ability of the methods to detect and isolate the following faults using only position and pressure measurements: 1) internal leakage in hydraulic cylinders, 2) external leakages, 3) fault related to an increase of friction in either hydraulic actuators or load, 4) fault related to pressure sensors. From the measurements and the physical constraints on the system it is possible to generate two residuals by the mean of a structural analysis and the resulting incidence matrix of the system. The two generated residuals, equal to zero with an additional noise in the fault free case, take non-zero values in the presence of one of the faults enumerated previously. By the mean of averaging and simple operations (for example RMS value for sinusoidal signals) on the residuals together with a threshold test, the changes detected by this manner furnishes sufficient information to detect and isolate each of the faults in the case of high fault severity (i.e. when the changes caused by a fault in the residuals are more than two times as high as the residual noise characteristics). The presented methods are believed to easily generalise on more complex EHSS. However, for low severity faults, a simple threshold test is no longer sufficient and hypothesis testing must be realised on the residuals to detect changes. In the special case where the system is in steady-state,

the residual can be approximated as white Gaussian noise in the fault free case which enables for the design of a composite hypothesis test. Two application examples were investigated where fault related to leakage flow inside the cylinder has been successfully diagnosed in both simulations and experiments. In the general case where the input, outputs and states are varying, the residuals can not be approximated as white Gaussian noise in the fault free case making hypothesis testing difficult to design. Two alternative techniques have been developed in this case, using extended Kalman filter and state augmented Kalman filter respectively in order to detect and isolate faults related to leakage even when the internal friction state is not available. The first method considers the leakage parameter in the EHSS as an augmented state and its estimation gives a direct information on the presence of fault or not. The second quantises in a first step the EHSS in several hypothesis related to the leakages parameters and then selects in a second step the hypothesis for which the estimation of the measured outputs is the best. Experimental results demonstrated the feasibility of the proposed methods and low nominal leakage flow were diagnosed when designing the fault detector based on the new model of the EHSS developed in the second chapter of this dissertation. However, the time to process the estimation of the state using Kalman filters makes the methods not suitable for online fault diagnosis. The recommendations from this thesis when designing fault detector for EHSS are 1) to implement a dual fault detector, one running online at the same sampling rate as the measurements and using simple threshold testing of the residuals for detecting high severity fault as fast as possible with an acceptable false alarm rate and the second, running offline over recorded data using statistical hypothesis testing and Kalman filters to prognose fault of lower severity, and 2) to develop a high fidelity model of the EHSS first as the model influences to a great extent on the fault detector performances.

The third main contribution of the thesis is the development of a high performance adaptive nonlinear controller for EHSS and its implementation on the test bed. Several assets characterise the controller: 1) Based on the nonlinear model of the system, the controller, using backstepping design, is valid for any operating points as long as the servo valve does not saturate. 2) Compared to linear controllers (proportional, lag compensator, H_∞) which are widely used in the industry, the new controller performs significantly better for position tracking of small amplitude step changes. The main reason is the presence of an accurate friction model in the design of the controller. 3) Because of its adaptivity, uncertainties in the mass, the load, leakages and friction parameters can be handled. 4) By its cascade structure, the complexity of the proposed controller is significantly reduced compared to a pure backstepping controller including valve and friction dynamics, making its real-time implementation possible with one millisecond step time.

The last main contribution of the thesis is the development of an active fault-

tolerant controller for EHSS and its real-time implementation on the test bed. Combining the techniques of fault detection and isolation with the nonlinear controller developed in this thesis, active fault-tolerant control has been achieved. Online fault diagnosis for faults related either to internal leakage or to friction in the cylinder with active parameter update for the backstepping controller has been demonstrated as well as active controller reconfiguration in the case of detection and isolation of fault related to pressure sensors. In this last case the controller switches seamlessly from nonlinear to linear proportional control.

5.3 Future Research Directions

There are several remaining challenges not addressed in this dissertation when it comes to nonlinear adaptive fault-tolerant control for electro hydraulic servo systems. These topics for further research which are motivated by the work realised and the results achieved in the thesis are briefly introduced below.

Servo valve behaviour. The model of the servo valve presented assesses the importance of considering the valve dynamics as a second order system and using an additional dither signal in order to reduce stiction of the valve spool inside the sleeve. However, further work is needed to model the behaviour of the servo valve with higher accuracy. Additional measurement of the spool displacement and velocity, consideration of dynamic friction of the spool inside the sleeve and analysis of the fluid film formation could increase the model accuracy and hence the model based fault detection and controller performances. Furthermore it could lead to an optimisation of the dither frequency and amplitude.

Fault prognosis. Further work is needed in order to analyse the probability distribution function of the noise in the residuals in the general case where the states are not constant. This statistical analysis should be considered in order to predict the fault alarm rate for a given threshold with a desired confidence interval. Further work is also needed to generalise the fault detector in the case of coloured noise in measurements. Finally, in order to enable online fault diagnosis using Kalman filters, optimisation of the algorithm would be required.

Nonlinearities consideration. The level of nonlinearities present in the EHSS has been reduced in this dissertation by considering double rod hydraulic cylinders and by limiting the operations within the operating range of the servo

valve. However, additional nonlinearities occur when considering single rod hydraulic cylinder and saturation in the servo valve. The generalisation of the controller in the case of these additional nonlinearities would considerably increase the range of possible applications for the developed methods regarding nonlinear and adaptive fault-tolerant control of EHSS.

Nonlinear control benchmark. The techniques presented in this thesis for the control of a nonlinear EHSS are based on the Lyapunov stability and backstepping methods. A benchmark of several other nonlinear control techniques applied to EHSS will undoubtedly provide a more compelling basis for the design of nonlinear fault-tolerant controllers best fitted for the desired application. Another candidate using Lyapunov based methods is sliding mode control or passivity techniques could be implemented by describing the EHSS as a port control Hamiltonian system.

Larger EHSS The techniques developed in this thesis for a representative EHSS could be implemented on larger EHSS in terms of complexity and number of components, considering redundant actuators and sensors to better prognose a fault and accomodate for it. For example in the presented test bed, flow sensors, accelerometers and strain gauges could be added to the system as well as a redundant actuator or servo valve. Further work is also needed for autotuning of the model parameters and automatic design of active fault-tolerant controller. Finally, a future research direction is the implementation adpative nonlinear fault-tolerant control on industrial EHSS.

Bibliography

- [1] A.G. Alleyne. Systematic control of a class of nonlinear systems with application to electrohydraulic cylinder pressure control. *IEEE Transactions on Control Systems Technology*, 8(4):623–634, July 2000.
- [2] L. An and N. Sepehri. Hydraulic actuator leakage fault detection using extended Kalman filter. *International Journal of Fluid Power*, 2005.
- [3] W. Backé. The present and future of fluid power. *ARCHIVE: Proceedings of the Institution of Mechanical Engineers, Part I: Journal of Systems and Control Engineering 1991-1996 (vols 205-210)*, 207(49):193–212, 1993.
- [4] M. Basseville and I.V. Nikiforov. *Detection of abrupt changes: theory and application*, volume 15. Citeseer, 1993.
- [5] Mark Beck, A. Schwung, M. Muenchhof, and R. Isermann. Fault-tolerant control of an electro-hydraulic servo axes with a duplex-valve-system. *nt.ntnu.no*, pages 9425–9433, 2011.
- [6] M. Blanke, M. Kinnaert, J. Lunze, and M. Staroswiecki. *Diagnosis and Fault-Tolerant Control*. Springer-Verlag, 2006.
- [7] M. Blanke and M. Staroswiecki. Structural design of systems with safe behavior under single and multiple faults. *14th IFAC Safeprocess\ ' 2006*, 54(2):511–516, 2006.
- [8] C. Bohn. *Recursive Parameter Estimation for Nonlinear Continuous Time Systems through Sensitivity Model Based Adaptive Filters*. PhD thesis, University of Bochum, 2000.

- [9] A. Bonchis, P.I. Corke, and D.C. Rye. A pressure-based, velocity independent, friction model for asymmetric hydraulic cylinders. *Proceedings 1999 IEEE International Conference on Robotics and Automation (Cat. No. 99CH36288C)*, (May 1999):1746–1751, 1999.
- [10] A. Bonchis, P.I. Corke, and D.C. Rye. Experimental Evaluation of Position Control Methods for Hydraulic Systems. *IEEE Transactions on Control Systems Technology*, 10(6):876–882, 2002.
- [11] C. Canudas de Wit, H. Olsson, K.J. Åström, and P. Lischinsky. A new model for control of systems with friction. *IEEE Transactions on Automatic Control*, 40(3):419–425, March 1995.
- [12] Liang Chen and Steven Liu. Fault diagnosis integrated fault-tolerant control for a nonlinear electro-hydraulic system. pages 1039–1044, 2010.
- [13] M. Choux and G. Hovland. Adaptive backstepping control of nonlinear hydraulic-mechanical system including valve dynamics. *Modeling, Identification and Control*, 31(1):35–44, 2010.
- [14] M.a.B. Cunha. Adaptive Cascade Controller Applied to a Hydraulic Actuator. *2005 International Conference on Control and Automation*, pages 622–627, 2005.
- [15] JC Doyle, K. Glover, PP Khargonekar, and BA Francis. State-space solutions to standard H_2 and H_∞ control problems. *IEEE Transactions on Automatic control*, 34(8):831–847, 1989.
- [16] O. Egeland and J.T. Gravdahl. *Modeling and simulation for automatic control*, volume 76. Marine Cybernetics, 2002.
- [17] Shreekanth Gayaka and Bin Yao. Fault Detection , Identification and Accommodation for an Electro-hydraulic System : An Adaptive Robust Approach. (2005):13815–13820, 2008.
- [18] F. Gustafsson. *Adaptive filtering and change detection*, volume 5. Wiley Online Library, 2000.
- [19] H. Hammouri, P. Kabore, S. Othman, and J. Biston. Failure diagnosis and nonlinear observer. Application to a hydraulic process. *Journal of the Franklin Institute*, 339(4-5):455–478, 2002.
- [20] F.C. Johansen. Flow through Pipe Orifices at Low Reynolds Numbers. *Proceedings of the Royal Society A: Mathematical, Physical and Engineering Sciences*, 126(801):231–245, January 1930.
- [21] M. Karpenko and N. Sepehri. Fault-tolerant control of a servohydraulic positioning system with crossport leakage. *IEEE Transactions on Control Systems Technology*, 13(1):155–161, January 2005.

- [22] Mark Karpenko and Nariman Sepehri. Quantitative Fault Tolerant Control Design for a Leaking Hydraulic Actuator. *Journal of Dynamic Systems, Measurement, and Control*, 132(5):054505, 2010.
- [23] S.M. Kay. Fundamentals of statistical signal processing: estimation theory. *Technometrics*, 37(4):465, November 1993.
- [24] S.M. Kay. *Fundamentals of Statistical Signal Processing - Detection Theory*, volume 2. Prentice-Hall, London, 1998.
- [25] D.H. Kim and T.-C. Tsao. A linearized electrohydraulic servovalve model for valve dynamics sensitivity analysis and control system design. *Journal of Dynamic Systems, Measurement, and Control*, 122(1):179–187, 2000.
- [26] M. Krstić, I. Kanellakopoulos, and P. Kokotović. *Nonlinear and Adaptive Control Design*. Adaptive and Learning systems for signal processing, communications and control. Wiley, 1995.
- [27] M. Krstić, I. Kanellakopoulos, and P. Kokotović. *Nonlinear and Adaptive Control Design*. Wiley, New York, 1995.
- [28] M. Laursen, M. Blanke, and D. Düstegör. Fault diagnosis of a water for injection system using enhanced structural isolation. *International Journal of Applied Mathematics and Computer Science*, 18(4):593–604, 2008.
- [29] H.E. Merritt. *Hydraulic Control Systems*. John Wiley and Sons, 1967.
- [30] T.-T. Ming, Y.-X. Zhang, and X.-Y. Zhang. Fault Detection for Electro-Hydraulic Valve-Controlled Single Rod Cylinder Servo System Using Linear Robust Observer. In *2009 International Conference on Measuring Technology and Mechatronics Automation Vol 1*, pages 639–642, 2009.
- [31] M. Muenchhof. Semiphsical Models of a Hydraulic Servo Axis for Fault Detection. *2007 American Control Conference*, pages 1834–1839, July 2007.
- [32] N. Niksefat and N. Sepehri. A QFT fault-tolerant control for electrohydraulic positioning systems. *IEEE Transactions on Control Systems Technology*, 10(4):626–632, July 2002.
- [33] H Noura, D Theilliol, and JC Ponsart. *Fault-tolerant control systems: Design and practical applications*. Springer, Dordrecht/Heidelberg/London, 2009.
- [34] A. de Pennington, J.J.’t Mannetje, and R. Bell. The modelling of electrohydraulic control valves and its influence on the design of electrohydraulic drives. *ARCHIVE: Journal of Mechanical Engineering Science 1959-1982 (vols 1-23)*, 16(3):196–204, June 1974.

- [35] N.K. Poulsen and H. Niemann. Active fault diagnosis based on stochastic tests. *International Journal of Applied Mathematics and Computer Science*, 18(4):487–496, 2008.
- [36] S.E. Salcudean. On the Nonlinear Control of Hydraulic Servo-systems. (April):1276–1282, 2000.
- [37] D. Schindele and H. Aschemann. Adaptive friction compensation based on the LuGre model for a pneumatic rodless cylinder. *35th Annual Conf. of IEEE Industrial Electronics*, pages 1432–1437, November 2009.
- [38] M. Sepasi and F. Sassani. On-line fault diagnosis of hydraulic systems using Unscented Kalman Filter. *International Journal of Control, Automation and Systems*, 8(1):149–156, 2010.
- [39] S. Skogestad and I. Postlethwaite. *Multivariable feedback control: analysis and design*, volume 8. Wiley-Interscience, December 2005.
- [40] R.J. Veillette, J.B. Medanic, and W.R. Perkins. Design of reliable control systems. *IEEE Transactions on Automatic Control*, 37(3):290–304, March 1992.
- [41] J. Watton. *Condition Monitoring and Fault Diagnosis in Fluid Power Systems*. Wllis Horwood, 1992.
- [42] H Yanada and Y. Sekikawa. Modeling of dynamic behaviors of friction. *Mechatronics*, 18(7):330–339, September 2008.
- [43] H. Yanada, K. Takahashi, and A. Matsui. Identification of Dynamic Parameters of Modified LuGre Model and Application to Hydraulic actuator. *JFPS International Journal of Fluid Power System*, 3(1):1–8, 2010.
- [44] H. Yu, Z.-J. Feng, and X.-Y. Wang. Nonlinear control for a class of hydraulic servo system. *Journal of Zhejiang University Science*, 5(11):1413–1417, 2004.
- [45] H. Zeng and N. Sepehri. Tracking Control of Hydraulic Actuators Using a LuGre Friction Model Compensation. *Journal of Dynamic Systems, Measurement, and Control*, 130(1):014502, 2008.

www.elektro.dtu.dk

Department of Electrical Engineering

Automation and Control

Technical University of Denmark

Ørsted's Plads

Building 348

DK-2800 Kgs. Lyngby

Denmark

Tel: (+45) 45 25 38 00

Fax: (+45) 45 93 16 34

Email: info@elektro.dtu.dk

ISBN 978-87-92465-92-4